Implementation of 2D/3D-Unstructured Grid Capabilities into MIN3P-THCm

NWMO-TR-2022-10 March 2022

Danyang Su[1], K. Ulrich Mayer[1] and Kerry MacQuarrie[2]

[1]Department of Earth, Ocean and Atmospheric Sciences, University of British Columbia

[2]Department of Civil Engineering, University of New Brunswick

nwmo
NUCLEAR WASTE MANAGEMENT ORGANIZATION
SOCIÉTÉ DE GESTION DES DÉCHETS NUCLÉAIRES

Nuclear Waste Management Organization
22 St. Clair Avenue East, 4th Floor
Toronto, Ontario
M4T 2S3
Canada

Tel: 416-934-9814
Web: www.nwmo.ca

Implementation of 2D/3D-Unstructured Grid Capabilities into MIN3P-THCm

NWMO-TR-2022-10

March 2022

Danyang Su[1], K. Ulrich Mayer[1] and Kerry MacQuarrie[2]

[1]Department of Earth, Ocean and Atmospheric Sciences, University of British Columbia

[2]Department of Civil Engineering, University of New Brunswick

Document History

Title:	Implementation of 2D/3D-Unstructured Grid Capabilities into MIN3P-THCm		
Report Number:	NWMO-TR-2022-10		
Revision:	R000	Date:	March 2022
[1]Department of Earth, Ocean and Atmospheric Sciences, University of British Columbia [2]Department of Civil Engineering, University of New Brunswick			
Authored by:	Danyang Su[1]		
Verified by:	Kerry MacQuarrie[2]		
Approved by:	K. Ulrich Mayer[1]		
Nuclear Waste Management Organization			
Reviewed by:	Tammy Yang, Alec Blyth		
Accepted by:	Paul Gierszewski		

Revision Summary		
Revision Number	**Date**	**Description of Changes/Improvements**
R0	2022-03	Initial issue

ABSTRACT

Title: **Implementation of 2D/3D-Unstructured Grid Capabilities into MIN3P-THCm**
Report No.: **NWMO-TR-2022-10**
Author(s): Danyang Su[1], K. Ulrich Mayer[1] and Kerry MacQuarrie[2]
Company: [1]Department of Earth, Ocean and Atmospheric Sciences, University of British Columbia
[2]Department of Civil Engineering, University of New Brunswick
Date: March 2022

Abstract
Simulating flow and reactive transport in sedimentary basins and in crystalline rock often requires discretization of complex domains. In sedimentary rocks, for example, complex geometry is due to the presence of multiple geologic layers, which are commonly inclined and/or pinch out. Biogeochemical reactions tend to occur at interfaces between layers, implying that gradients controlling fluid and solute exchange are often large near the interfaces, requiring refined spatial discretization in these regions. The spatial discretization of such domains in 2D and 3D is difficult and can be cumbersome when using a structured grid that is limited to rectangular meshes. An unstructured grid that can more easily replicate irregular geometries is beneficial. Unstructured grid capabilities not only provide greater flexibility for discretizing complex domains, but also avoid averaging of material properties at interfaces. This report describes the approach used to implement 2D/3D-unstructured grid capabilities into MIN3P-THCm V1.1 (Su et al. 2017), a parallel version of a generic process-based reactive transport code designed for the investigation of multicomponent reactive transport in variably saturated media. The parallelized unstructured grid version, MIN3P-THCm V2.0.0, uses vertex-centered control volume methods with different control volume types and gradient reconstruction methods. MIN3P-THCm V2.0 is designed for any 2D simulation domain utilizing triangular and quadrilateral cells for mesh construction, and any 3D simulation domain utilizing tetrahedral, hexahedral and prism cells. MIN3P-THCM V2.0 also provides new modules to assist the user with setting up simulations. These modules include built-in 2D/3D-mesh generation with local mesh refinement; mesh conversion from external software such as GMS; as well as preprocessing and postprocessing using the vtk file format.

The report is structured as follows. In the first chapter, the background on unstructured grid methods in reactive transport simulation is introduced. In the second chapter, the key governing equations for flow and reactive transport are presented. In the third chapter, the governing equations are discretized. Different gradient reconstruction methods, multi-point flux approximation and upstream weighting methods are presented. The hybrid MPI-OpenMP parallelization method is briefly described. In the fourth chapter, the new multi-point flux approximation method is analyzed for challenging sharp wetting front problems in variably saturated media. In the fifth chapter, the applicability of the code for general flow and reactive transport problems is demonstrated. In the sixth chapter, the parallel performance of MIN3P-THCm V2.0 is analyzed. In the seventh chapter, MIN3P-THCm V2.0 is verified against existing MIN3P-THCm V1.0 benchmarks. In the eighth chapter, additional verification examples are provided, focusing on the use of unstructured grids in comparison to other existing MIN3P-THCm V1.0 benchmarks. Finally, in the ninth chapter, the code enhancements are discussed, and conclusions are provided.

TABLE OF CONTENTS

LIST OF TABLES

Page

LIST OF FIGURES

Page

1. INTRODUCTION

Simulation of flow and reactive transport is a nontrivial task, especially when applied to complex irregular solution domains. Discretization of complex domains in 2D and 3D is challenging, in particular when using a structured grid that only allows for the generation of rectangular meshes. There are notable restrictions with standard structured grids, of which the following two are most important: 1) the irregular shaped domain boundaries cannot be easily represented with a structured grid, and 2) it is difficult to refine the grid resolution in the areas of interest.

Complex geometries arise due to the presence of multiple geologic layers, which are commonly inclined and often pinch out. Biogeochemical reactions often tend to occur at interfaces between layers, implying that gradients controlling fluid and solute exchange can be large near the interfaces, requiring refined spatial discretization in these regions. The spatial discretization of such domains in 2D and 3D can be cumbersome and material properties need to be averaged when using structured grids; leading to an inaccurate description of the physical system. For such simulations, structured discretization methods can be applied by inactivating parts of the grid outside the domain of interest, but the domain remains bounded by rectangular grid cells that may not follow the irregular boundaries. As a result, information about the entire grid, including inactive cells, is read and processed. By using this strategy, MIN3P-THCm has been used to simulate reactive transport in sedimentary basins subjected to glaciation and deglaciation events (Bea et al. 2016, 2018). Other problems of interest may include the simulation of processes within and in the direct vicinity of a waste repository. One approach to tackle such a case is to define a fine mesh nested within a coarse mesh, where the coarse mesh first generates results at the boundary of the fine mesh and then the fine mesh uses these results as the transient boundary conditions for a sub-simulation. The above method is not perfect, but it is a suitable approach, if a code with unstructured grid capabilities and local mesh refinement is not available.

Compared to structured grid discretization, unstructured grid methods have intrinsic advantages for handling complex geometry and heterogeneous material properties. Unstructured grids not only provide greater flexibility for discretizing complex domains, but they also enable straightforward implementation of adaptive meshing techniques, thus enhancing solution accuracy and efficiency. However, due to the complexity of solution algorithms and code development, the number of subsurface simulators using unstructured grids is still limited. Among these codes, FEFLOW (Trefry and Muffels 2007) was one of the earliest codes for groundwater flow, contaminant and heat transport simulation, based on a layered unstructured mesh. FRAC3DVS (Therrien and Sudicky 1996) and its successor HydroGeoSphere (https://www.aquanty.com/hydrogeosphere/) are other codes based on layered meshes developed for simulation of 3D surface and subsurface flow, solute and energy transport. MODFLOW-USG is another flow and transport code with unstructured grid capabilities (Panday et al. 2013). To the authors' knowledge, very few reactive transport codes possess unstructured grid capabilities. PFLOTRAN (Hammond et al. 2012) is one of the reactive transport codes that can use unstructured meshes for both flow and reactive transport simulations in complex porous media. In addition, TOUGHREACT (Xu et al. 2012) has unstructured grid capabilities derived from introducing reactive chemistry into the multiphase flow and transport code TOUGH2 (https://tough.lbl.gov/tough-history/).

This report presents the approach used to implement fully unstructured grid discretization into MIN3P-THCm V1.1 (Su et al. 2017), a parallel version of a process-based reactive transport code designed for the investigation of multicomponent reactive transport in variably saturated

media under non-isothermal conditions. The key features of the code include 3D saturated/unsaturated fluid flow, biogeochemical reactions, heat transport, solute and gas transport, density coupling between flow and transport, and 1D hydro-mechanical coupling. MIN3P-THCm uses a global implicit method implemented using the direct substitution approach for solution of the multicomponent advection-dispersion equations and biogeochemical reactions. However, the requirement of a structured grid approach limits the application of MIN3P-THCm V1.1 in some cases. The enhanced code MIN3P-THCm V2.0 comes with the capabilities of high performance computing as well as high performance code for complex geometry. The objectives were: 1) to develop a flexible method to support different cell types in 2D and 3D, while maintaining high-order numerical accuracy; and (2) to implement a high-performance parallelization approach that takes advantages of cutting edge computer architecture, and allows the use of OpenMP, MPI or hybrid MPI-OpenMP for acceleration and scaling. The main features of the enhanced MIN3P-THCm include:

1.1 Input Features

A built-in pre-processor for generating 2D and 3D unstructured grid meshes is implemented based on the efficient and reliable geometric algorithm library CGAL (http://www.cgal.org/). The new code also supports mesh conversion from third-party programs such as “GMS” to build irregular, layered meshes composed of blocks or prisms. Another important feature in the enhanced MIN3P-THCm V2.0 is that it allows definitions of arbitrary regions within the simulation domain. Zones can be defined geometrically by polygons in 2D and polyhedra in 3D. All nodes within the specified geometry are assigned a unique number that can be used later to assign material properties, initial and boundary conditions. The material properties can be assigned layer by layer without averaging at the interface.

1.2 Discretization Features

MIN3P-THCm V2.0 is based on node-centered spatial discretization and uses several different control volume types and gradient reconstruction methods. Three control volume types are considered: median dual (MD) control volume, cell center (CC) control volume, and Voronoi diagram (VD) control volume. Three different gradient reconstruction methods are included: Green-Gauss (GG) gradient reconstruction, least-squares (LS) gradient reconstruction and high order least-squares (HLS) gradient reconstruction have been implemented. In calculating fluxes over control volume interfaces, both a two-point flux approximation (TPFA) and a multi-point flux approximation (MPFA) are supported, with multi-point upstream weighting available for the MPFA method. Different cell types are considered, including triangular and quadrilateral cells in 2D, as well as tetrahedral, hexahedral and prism cells in 3D.

1.3 Output Features

MIN3P-THCm V2.0 uses the VTK (visualization toolkit, http://www.vtk.org/) file format for the spatial output. The advanced HDF5 & XDMF data format is used for the high-performance input and output. The results are written in a general form that can be supported by open-source software such as Paraview (http://www.paraview.org/) and VisIt (https://wci.llnl.gov/simulation/computer-codes/visit).

2. Governing Equations

To provide context for the unstructured grid development, the governing equations of the MIN3P-THCm model are briefly reviewed below. The key model components consist of density dependent variably-saturated flow, energy transport and multicomponent reactive transport. Additional details on the underlying theory and governing equations for biogeochemical reactions, activity corrections and mechanical loading calculations can be found in the following references (Mayer et al. 2002, Henderson et al. 2009, Mayer and MacQuarrie 2010, Bea et al. 2012, 2016).

2.1 Density-Dependent Variably-Saturated Flow

The governing equation for non-isothermal and density-dependent variably-saturated flow is (Henderson et al. 2009, Bea et al. 2012):

$$\phi S_a \frac{\partial \rho_a}{\partial t} + \rho_a \frac{S_s}{\rho_w g} \frac{\partial P}{\partial t} - \nabla \cdot \rho_a \boldsymbol{q}_a - Q_a = 0 \qquad 2\text{-}1$$

where ϕ [L^3 void L^{-3} bulk] is porosity, S_a [L^3 water L^{-3} void] is the saturation of the aqueous phase, ρ_a [M L^{-3}] is the pore water density, which is a function of temperature and solution composition, ρ_w [M L^{-3}] is the freshwater density, t [T] is time, P [M L^{-1} T^{-2}] is the fluid pressure, S_s [L^{-1}] is the specific storage coefficient, g [L T^{-2}] is the gravity constant, Q_a [M L^{-3} T^{-1}] is a source-sink term for the aqueous and $\boldsymbol{q}_a$ [L T^{-1}] is the aqueous phase flux, which is defined as:

$$\boldsymbol{q}_a = \frac{k_r \boldsymbol{k}}{\mu} (\nabla P + \rho_a g \nabla z) \qquad 2\text{-}2$$

where k_r [-] is the relative permeability, $\boldsymbol{k}$ [L^2] is the intrinsic permeability tensor, z [L] is elevation and μ [M L^{-1} T^{-1}] is the viscosity of the aqueous phase. The saturation and relative permeability are a function of the aqueous phase pressure based on the relations given by Wöste & van Genuchten (1988) .

2.2 Energy Transport

The formulation for energy transport implemented in MIN3P-THCm is:

$$\frac{\partial \phi c_a S_a \rho_a}{\partial t} + \frac{\partial \phi c_g S_g \rho_g}{\partial t} + \frac{\partial (1-\phi) c_s \rho_s}{\partial t} + \frac{\partial L_w \phi S_g \rho_g}{\partial t} - \nabla \cdot J_e - Q_e = 0 \qquad 2\text{-}3$$

where c_a, c_g and c_s [E M^{-1} °C] are the heat capacities for aqueous, gas (vapour) and solid phases, respectively; ρ_g and ρ_s [M L^{-3}] are the density of gas (vapour) and solid phases, respectively; S_g [L^3 gas L^{-3} void] is the gas (vapour) phase saturation; $\nabla \cdot J_e$ [E L^{-3} T^{-1}] is the energy flux; L_w [E M^{-1}] is the latent heat of vaporization for water; and Q_e [E L^{-3} T^{-1}] is an energy source-sink term.

2.3 Reactive Transport

The global mass conservation equations for reactive transport, which contain the contributions of all mobile, adsorbed and mineral species, are (Mayer 1999):

$$\frac{\partial}{\partial t}[S_a \phi T_i^a] + \frac{\partial}{\partial t}\left[S_g \phi T_i^g\right] + \frac{\partial T_i^s}{\partial t} + \nabla \cdot [\boldsymbol{q}_a T_i^a] - \nabla \cdot [S_a \phi \mathbf{D}_a \nabla T_i^a] - \nabla \cdot \left[S_g \phi \mathbf{D}_g \nabla T_i^g\right] - Q_i^{a,a} - Q_i^{a,m} - Q_i^{a,ext} - Q_i^{g,ext} = 0 \qquad i = 1, N_c \tag{2-4}$$

where T_i^a [mol L^{-3} H_2O] is the total aqueous component concentration for the component A_i^c, T_i^g [mol L^{-3} gas] is the total gaseous concentration for the component A_i^c, and T_i^s [mol L^{-3} bulk] is the total concentration of the aqueous component A_i^c on the surface sites. $\mathbf{D}_a$ [L^2 T^{-1}] is the dispersion tensor for the aqueous phase and $\mathbf{D}_g$ [L^2 T^{-1}] is the dispersion tensor for the gaseous phase. $Q_i^{a,a}$ [mol L^{-3} T^{-1}] and $Q_i^{a,m}$ [mol L^{-3} T^{-1}] are internal source and sink terms from intra-aqueous kinetic reactions and kinetically controlled dissolution-precipitation reactions. $Q_i^{a,ext}$ [mol L^{-3} T^{-1}] and $Q_i^{g,ext}$ [mol L^{-3} T^{-1}] are external source and sink terms for the aqueous phase and gas phase, respectively.

3. Numerical Discretization and Parallelization

In this chapter, the numerical discretization of the governing equations for unstructured mesh is provided, followed by a description of the parallelization strategy.

3.1 Numerical Discretization with Vertex-Centered MPFA method

Due to its intrinsic mass conservation feature, the finite volume method (FVM) is one of the most popular methods for solving fluid flow and transport equations. Depending on the location of the solutions values, the FVM can be classified into cell-centered and node-centered (also known as vertex-centered) methods. Given the same mesh, the solutions of the cell-centered method are located at the centroid of the cells and the solutions of the node-centered method are located at the nodes of the mesh. In this work, we focus on the node-centered approach. For node-centered approaches, a dual mesh, which represents the control volumes at each node, must be created based on the provided mesh. Three different types of dual mesh methods are used in this work. The first dual mesh type is referred as the medial-dual (MD) type, which joints the midpoint of each edge of the mesh with the center of the cell. The second dual mesh type is referred as the Voronoi-diagram (VD) type, in which case the segment that joints the two adjacent cell centers is perpendicular to their common edge and crosses this edge at the midpoint. The third dual mesh type is referred to as the cell-center (CC) type, which joins the centers of adjacent cells. Illustration of dual mesh types for a triangular mesh is shown in Figure 3-1. In this work, a modified form of VD type is also provided suitable for meshes with obtuse cells. The midpoint of the largest edge is treated as the cell center to build the dual mesh, as shown in Figure 3-1 (b). The CC and MD types work for triangular mesh with obtuse cells without redefining the cell center. However, in a skewed mesh, the segment that joins two adjacent cell centers may not cross the shared edge. Therefore, the CC type cannot be used, because the control volume interface and the mesh edge do not cross. It should be noted that the center of the control volume face is selectable. It can be either the half-face center (HFC), the point P as shown in Figure 3-1 (d), or the intersection of the half-face and $edge\ ij$ (IHFE), the point Q in Figure 3-1 (d). For VD or CC control volume types, IHFE is close to the middle point of two HFCs shared by the same edge.

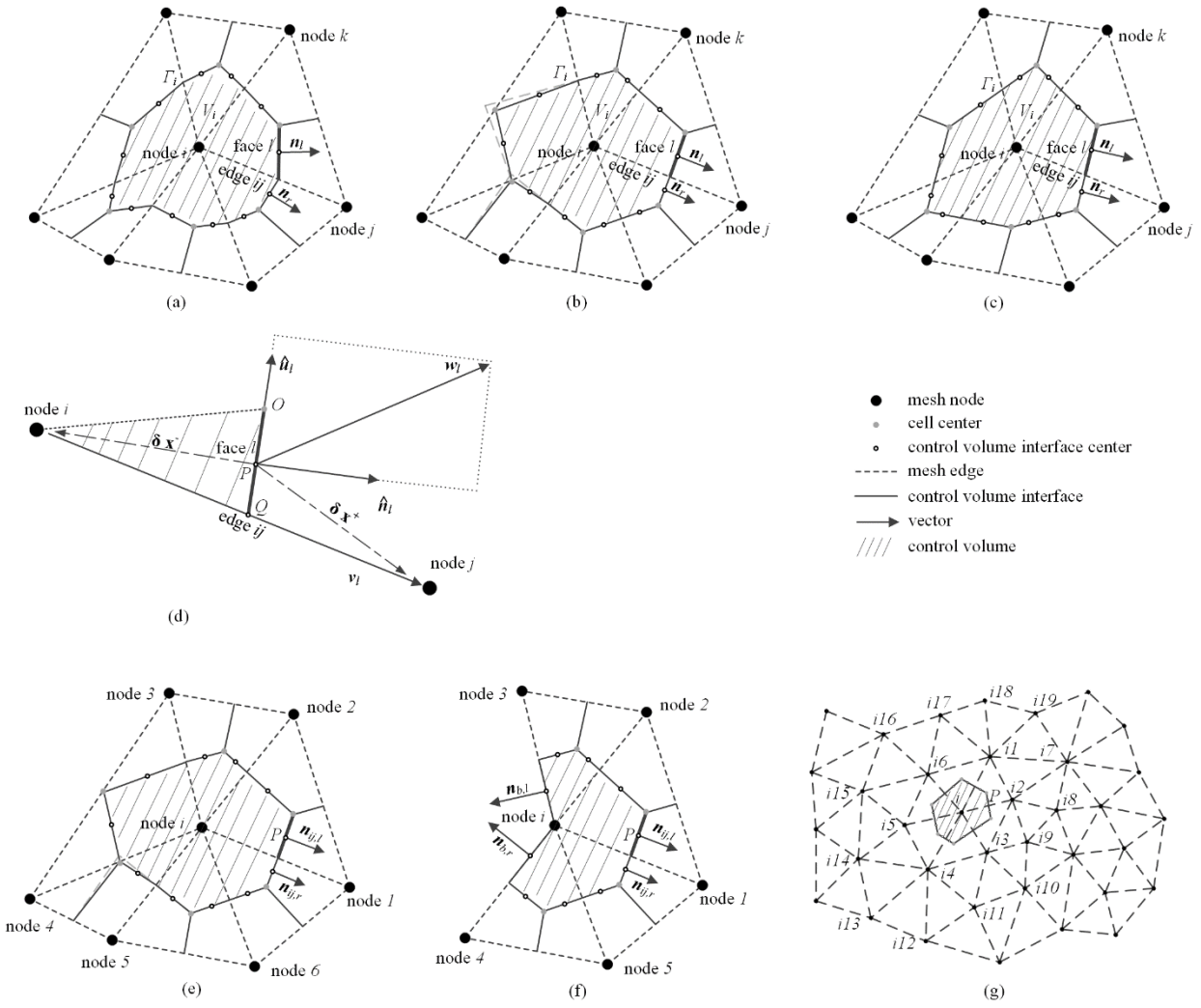

Figure 3-1: Illustration of Meshes and Corresponding Dual Control Volume and Gradient Reconstruction Methods, (a) MD Method for Triangular Mesh, (b) VD Method for Triangular Mesh, (c) CC Method for Triangular Mesh, (d) Local Control Volume Interface and Geometric Parameters, (e) Gradient Reconstruction for Internal Node, (f) Gradient Reconstruction for Boundary Node, and (g) Direct and Indirect Neighbouring Nodes for Node i

Taking the density dependent flow equation 2-1 as an example, for the defined control volume V_i enclosed by its boundary Γ_i, the governing equation can be rewritten in the integral conservative form by applying the Gauss divergence theorem.

$$\int_{\Delta t} \phi S_a \frac{\partial}{\partial t} \iiint_{V_i} \rho_a \, dV dt + \int_{\Delta t} \rho_a \frac{S_s}{\rho_w g} \frac{\partial}{\partial t} \iiint_{V_i} P \, dV dt = \int_{\Delta t} \oiint_{\Gamma_i} [\rho_a \boldsymbol{q}_a] \cdot \hat{\boldsymbol{n}} \, d\Gamma dt + \int_{\Delta t} \iiint_{V_i} Q_a \, dV dt \qquad 3\text{-}1$$

where $\hat{\boldsymbol{n}}$ is the unit outward normal of the control volume face. By applying the fully implicit time weighting, equation 3-1 can be rewritten as:

$$\begin{aligned}\phi S_a^{N+1}\left(\rho_{a,i}^{N+1}-\rho_{a,i}^{N}\right)V_i+\rho_{a,i}^{N+1}\frac{S_s}{\rho_w g}\left(\rho_{a,i}^{N+1}-\rho_{a,i}^{N}\right)V_i \\ =\sum_{l\in\Gamma_i}\rho_{a,l}^{N+1}\boldsymbol{q}_{a,l}^{N+1}\cdot\hat{\boldsymbol{n}}_l\,\Delta S_l\Delta t+Q_{a,i}^{N+1}V_i\Delta t\end{aligned} \tag{3-2}$$

where Δt [T] is the time increment; $N+1$ defines the new time level and N represents the old time level; l represents the l^{th} face of control volume V_i; ΔS_l [L in 2D and L^2 in 3D] is the area of the l^{th} face of control volume V_i; and $\boldsymbol{q}_{a,l}^{N+1}$ [$L\ T^{-1}$] is the mass flux through the l^{th} face of the control volume, which can be expressed as:

$$\boldsymbol{q}_{a,l}^{N+1}=\frac{k_{r,l}^{N+1}\boldsymbol{k}_l}{\mu}\nabla\left(P_l^{N+1}+\rho_{a,l}^{N+1}g\nabla z\right) \tag{3-3}$$

where $k_{r,l}^{N+1}$ [-] is the relative permeability coefficient of the l^{th} face of the control volume at the new time level, which can be calculated based on the relative permeability coefficients of adjacent nodes using centered weighting, harmonic weighting or upstream weighting methods. Equation 2-1 is nonlinear since the saturation and the relative permeability are a function of the fluid pressure, which can be described by Wöste & van Genuchten (1988):

$$S_a=S_r+\frac{1-S_r}{(1+\alpha P^n)^m} \tag{3-4}$$

$$S_e=\frac{S_a-S_r}{1-S_r} \tag{3-5}$$

$$k_r=S_e^l\left[1-\left(1-S_e^{1/m}\right)^m\right]^2 \tag{3-6}$$

where S_r [-] defines the residual saturation of the aqueous phase; S_e [-] is the effective saturation of the aqueous phase; α [L^{-1}], n [-], m [-] and l [-] are the soil hydraulic function parameters; and m is defined by:

$$m=1-\frac{1}{n} \tag{3-7}$$

The pressure gradient, $\nabla\left(P_l^{N+1}+\rho_{a,l}^{N+1}g\nabla z\right)$ [-], belongs to the l^{th} face of the control volume at the new time level considering the effect of the fluid density. Compared to the discretization using a structured mesh, equation 3-3 is the term that needs special treatment while the other terms in equation 3-2 remain the same or similar for both structured and unstructured discretization methods.

Substituting equation 3-3 into equation 3-2 yields the flux through the l^{th} face of the control volume during the time increment Δt:

$$\rho_{a,l}^{N+1}\boldsymbol{q}_{a,l}^{N+1}\cdot\hat{\boldsymbol{n}}_l\Delta S_l\Delta t=\rho_{a,l}^{N+1}\frac{\rho_{a,l}^{N+1}gk_{r,l}^{N+1}\boldsymbol{k}_l}{\mu}\nabla\left(\frac{P_l^{N+1}+\rho_{a,l}^{N+1}g\nabla z}{\rho_{a,l}^{N+1}g}\right)\cdot\hat{\boldsymbol{n}}_l\Delta S_l\Delta t \quad 3\text{-}8$$

$$=\rho_{a,l}^{N+1}k_{r,l}^{N+1}\boldsymbol{K}_l\nabla\psi\cdot\hat{\boldsymbol{n}}_l\Delta S_l\Delta t$$

where $\boldsymbol{K}_l=\boldsymbol{k}_l\frac{\rho_{a,l}^{N+1}g}{\mu}$ [L T^{-1}] is the hydraulic conductivity tensor, $\psi=\frac{P_l^{N+1}+\rho_{a,l}^{N+1}g\nabla z}{\rho_{a,l}^{N+1}g}$ [L] is the pressure head. Since $\rho_{a,l}^{N+1}$, $k_{r,l}^{N+1}$, ΔS_l and Δt are all scalar values that can be calculated based on the provided simulation parameters and geometric features of the mesh, we only need to focus on the calculation of $\boldsymbol{K}_l\nabla\psi\cdot\hat{\boldsymbol{n}}_l$ term for the different meshes. This term can be rewritten as:

$$\boldsymbol{K}_l\nabla\psi\cdot\hat{\boldsymbol{n}}_l=\nabla\psi\cdot\left(\boldsymbol{K}_l^T\hat{\boldsymbol{n}}_l\right)=\nabla\psi\cdot\boldsymbol{w}_l \quad 3\text{-}9$$

where $\boldsymbol{w_l}=\boldsymbol{K_l^T}\hat{\boldsymbol{n}}_{\boldsymbol{l}}$. As shown in Figure 3-1 (e), $\boldsymbol{w_l}$ can be further decomposed as:

$$\boldsymbol{w}_l=(\boldsymbol{w}_l\cdot\hat{\boldsymbol{u}}_l)\hat{\boldsymbol{u}}_l+(\boldsymbol{w}_l\cdot\hat{\boldsymbol{n}}_l)\hat{\boldsymbol{n}}_l \quad 3\text{-}10$$

where $\hat{\boldsymbol{u}}_l$ is the unit vector of the projection of $\boldsymbol{w}_l$ on the l^{th} face of the control volume and $\hat{\boldsymbol{n}}_l$ is the unit outward normal of the l^{th} face of the control volume. Since $\boldsymbol{K}_l$ is a symmetric diagonally dominant matrix, it is positive definite and $\boldsymbol{w}_l$ is of the same sign as unit outward normal vector $\hat{\boldsymbol{n}}_l$. Similarly, the *edge ij* can be written as:

$$\boldsymbol{v}_l=(\boldsymbol{v}_l\cdot\hat{\boldsymbol{u}}_l)\hat{\boldsymbol{u}}_l+(\boldsymbol{v}_l\cdot\hat{\boldsymbol{n}}_l)\hat{\boldsymbol{n}}_l \quad 3\text{-}11$$

By rearranging equation 3-10 and 3-11, we obtain:

$$\hat{\boldsymbol{u}}_l=\frac{\boldsymbol{w}_l-(\boldsymbol{w}_l\cdot\hat{\boldsymbol{n}}_l)\hat{\boldsymbol{n}}_l}{|\boldsymbol{w}_l-(\boldsymbol{w}_l\cdot\hat{\boldsymbol{n}}_l)\hat{\boldsymbol{n}}_l|} \quad 3\text{-}12$$

$$\hat{\boldsymbol{n}}_l=\frac{\boldsymbol{v}_l-(\boldsymbol{v}_l\cdot\hat{\boldsymbol{u}}_l)\hat{\boldsymbol{u}}_l}{\boldsymbol{v}_l\cdot\hat{\boldsymbol{n}}_l} \quad 3\text{-}13$$

Substituting equation 3-10, 3-12 and 3-13 into equation 3-9 yields:

$$\boldsymbol{K}_l\nabla\psi\cdot\hat{\boldsymbol{n}}_l=\underbrace{\frac{\boldsymbol{w}_l\cdot\hat{\boldsymbol{n}}_l}{\boldsymbol{v}_l\cdot\hat{\boldsymbol{n}}_l}\nabla\psi\cdot\boldsymbol{v}_l}_{primary\ term}+\underbrace{\left(\boldsymbol{w}_l\cdot\hat{\boldsymbol{u}}_l-\boldsymbol{w}_l\cdot\hat{\boldsymbol{n}}_l\frac{\boldsymbol{v}_l\cdot\hat{\boldsymbol{u}}_l}{\boldsymbol{v}_l\cdot\hat{\boldsymbol{n}}_l}\right)\nabla\psi\cdot\hat{\boldsymbol{u}}_l}_{secondary\ term} \quad 3\text{-}14$$

In equation 3-14, $\boldsymbol{w}_l$, $\boldsymbol{v}_l$, $\hat{\boldsymbol{n}}_l$, and $\hat{\boldsymbol{u}}_l$ are the physical and geometry parameters that can be calculated based on the provided mesh and material properties. The flux through the l^{th} face of the control volume consists of the primary term and a secondary term (also known as cross-diffusion term). For K-orthogonal meshes (e.g., structured mesh), both $\boldsymbol{w}_l\cdot\hat{\boldsymbol{u}}_l$ and $\boldsymbol{v}_l\cdot\hat{\boldsymbol{u}}_l$ equal

zero, such that the secondary term can be ignored. In the primary term, $\frac{\boldsymbol{w}_l \cdot \hat{\boldsymbol{n}}_l}{\boldsymbol{v}_l \cdot \hat{\boldsymbol{n}}_l}$ is the transmissibility coefficient (also known as influence coefficient in some literatures).

Here we provide the approximation of $\boldsymbol{\nabla\psi \cdot v_l}$. As shown in Figure 3-1 (d), let $\boldsymbol{x_P}$ denote the location of center point *P* on the $\boldsymbol{l^{th}}$ face of the control volume, $\boldsymbol{\delta x}^-$ be the vector from point *P* to *node i*, and $\boldsymbol{\delta x}^+$ be the vector from point *P* to *node j*, the *m*th order Taylor expansion of function $\boldsymbol{\psi}$ yields:

$$\psi(x_P + \boldsymbol{\delta x}^+) = \sum_{k=0}^{m} \frac{1}{k!} (\boldsymbol{\delta x}^+ \cdot \nabla)^k \, \psi(x_P) + R^+ \qquad m \geq 1 \tag{3-15}$$

$$\psi(x_P + \boldsymbol{\delta x}^-) = \sum_{k=0}^{m} \frac{1}{k!} (\boldsymbol{\delta x}^- \cdot \nabla)^k \, \psi(x_P) + R^- \qquad m \geq 1 \tag{3-16}$$

where the remainder R, written in Lagrangian form, can be expressed as:

$$R^+ = \frac{1}{(m+1)!} (\boldsymbol{\delta x}^+ \cdot \nabla)^{m+1} \psi(x_P + \theta \boldsymbol{\delta x}^+) \qquad 0 \leq \theta \leq 1 \tag{3-17}$$

Assuming that $R^+ \approx R^-$ and subtracting equation 3-16 from 3-15 yields:

$$\begin{aligned} \nabla\psi \cdot \boldsymbol{v}_l &= \nabla\psi \cdot [(x_P + \boldsymbol{\delta x}^+) - (x_P + \boldsymbol{\delta x}^-)] \\ &= \psi(x_P + \boldsymbol{\delta x}^+) - \psi(x_P + \boldsymbol{\delta x}^-) \\ &= \psi_j - \psi_i - \varepsilon_{ji} \end{aligned} \tag{3-18}$$

where ε_{ji} is the *m*th order remainder of the Taylor expansion, which can be expressed as:

$$\varepsilon_{ji} = \sum_{k=2}^{m} \frac{1}{k!} [(\boldsymbol{\delta x}^+ \cdot \nabla)^k - (\boldsymbol{\delta x}^- \cdot \nabla)^k] \psi(x_P) \tag{3-19}$$

It should be noted that higher order remainders of the Taylor expansion are only used for the HFC and IHFE methods with the CC control volume type. For the IHFE method with MD or VD control volume types, ε_{ji} is self-canceled. Also, for a good quality mesh, it is possible to assume $\varepsilon_{ji} \approx 0$; however, this simplification is not possible for a mesh with large expansion factors or aspect ratios. Substituting equation 3-18 into equation 3-14 yields:

$$\boldsymbol{K}_l \nabla\psi \cdot \hat{\boldsymbol{n}}_l \approx \frac{\boldsymbol{w}_l \cdot \hat{\boldsymbol{n}}_l}{\boldsymbol{v}_l \cdot \hat{\boldsymbol{n}}_l} (\psi_j - \psi_i - \varepsilon_{ji}) + \left(\boldsymbol{w}_l \cdot \hat{\boldsymbol{u}}_l - \boldsymbol{w}_l \cdot \hat{\boldsymbol{n}}_l \frac{\boldsymbol{v}_l \cdot \hat{\boldsymbol{u}}_l}{\boldsymbol{v}_l \cdot \hat{\boldsymbol{n}}_l} \right) \nabla\psi(x_P) \cdot \hat{\boldsymbol{u}}_l \tag{3-20}$$

Discretization of equation 2-3 and 2-4 can be carried out in a similar way as equation 2-1. To solve equation 3-20, the estimation of gradient at the control volume interface is required.

3.2 Gradient Reconstruction and MPUPS spatial weighting

In this section, an improved MPFA method with multi-point upstream (MPUPS) weighting based on gradient reconstruction method (MPFA-GRM) is introduced.

For K-orthogonal meshes, without considering second and higher order Taylor series remainders, equation 3-20 is reduced to $\boldsymbol{K}_l \nabla\psi \cdot \hat{\boldsymbol{n}}_l \approx \frac{\boldsymbol{w}_l \cdot \hat{\boldsymbol{n}}_l}{\boldsymbol{v}_l \cdot \hat{\boldsymbol{n}}_l}(\psi_j - \psi_i)$, a general form of the TPFA method. In other cases, the m^{th} order gradient of ψ is required for equation 3-19 and 3-20. Different MPFA methods to calculate the first order gradient of ψ have already been studied for cell-centered spatial discretization (Aavatsmark et al. 1998a, 1998b, Eigestad and Klausen 2005, Klausen and Winther 2006, Klausen et al. 2008, Aavatsmark 2008, Edwards and Zheng 2010). However, these methods cannot be directly applied to node-centered spatial discretization. In this section, we focus on the calculation of first and second order gradients of ψ at the center point *P* of the l^{th} face of the control volume in a 2D coordinate system. For the first order gradient reconstruction, we utilize Green-Gauss and least squares methods. For the second order gradient reconstruction, we use higher order least squares methods.

3.2.1 Green-Gauss Gradient Reconstruction Method

The Green-Gauss gradient reconstruction method (GG-GRM) is based on the assumption that the gradient is a global constant over in an individual cell cell (Nishikawa 2014). For a triangular mesh as shown in Figure 3-1 (e), the gradient of ψ over the the dual control volume V_i can be calculated by:

$$\nabla\psi = \frac{1}{\Delta V_i}\sum_{j=1}^{n}\frac{\psi_1 + \psi_j}{2}\left(\boldsymbol{n}_{ij,l} + \boldsymbol{n}_{ij,r}\right) \tag{3-21}$$

where ΔV_i [L^2 in 2D and L^3 in 3D] is the volume of the dual control volume; n (6 here) is the number of nodes connected to node i; $\boldsymbol{n}_{ij,l}$ and $\boldsymbol{n}_{ij,r}$ are the left and right scaled outward normals for the control volume face. For the boundary node as shown in Figure 3-1 (f), the gradient calculation is modified as:

$$\nabla\psi = \frac{1}{\Delta V_i}\left(\begin{array}{l}\displaystyle\sum_{j=1,2,5}\frac{\psi_1 + \psi_j}{2}\left(\boldsymbol{n}_{ij,l} + \boldsymbol{n}_{ij,r}\right) + \\ \displaystyle\frac{\psi_1 + \psi_3}{2}\boldsymbol{n}_{13,r} + \frac{\psi_1 + \psi_4}{2}\boldsymbol{n}_{14,l} + \\ \displaystyle\frac{5\psi_1 + \psi_4}{6}\boldsymbol{n}_{b,r} + \frac{5\psi_1 + \psi_3}{6}\boldsymbol{n}_{b,l}\end{array}\right) \tag{3-22}$$

where $\boldsymbol{n}_{b,l}$ and $\boldsymbol{n}_{b,r}$ are the left and right scaled outward normals of the boundary face.

More detailed information about gradient reconstruction methods for different cell types can be found in the literature (Nishikawa 2014). GG-GRM guarantees global mass conservation while retaining exactness for linear fluxes around each node.

3.2.2 Least-Squares Gradient Reconstruction Method

The least squares gradient reconstruction method (LS-GRM) is a method that is unrelated to the mesh topology. This method relies on a stencil, which identifies relevant neighboring nodes for use in the gradient estimation. The gradient of ψ over the dual control volume V_i is obtained by solving for the values of gradients that minimize the sum of the squares of the differences between neighboring values and calculated values based on the gradient (Mavriplis 2003). The objective to be minimized is given as:

$$\sum_{j=1}^{n} \omega_{ij}^2 E_{ij}^2 \tag{3-23}$$

where ω_{ij} is a weighting factor and E_{ij}^2 is the error calculated by:

$$E_{ij}^2 = \left(-d\psi_{ij} + u_{x,i} dx_{ij} + u_{y,i} dy_{ij}\right)^2 \tag{3-24}$$

where $d\psi_{ij} = \psi_j - \psi_i$, $dx_{ij} = x_j - x_i$, with similar expressions for dy_{ij}; $u_{x,i}$ and $u_{y,i}$ are the two gradient components to be solved. Dropping the subscript i for clarity, a system of two equations for the two gradient components are obtained by solving the minimization problem of:

$$\begin{cases} \dfrac{\partial \sum_{j=1}^{n} \omega_{ij}^2 E_{ij}^2}{\partial u_x} = 0 \\ \dfrac{\partial \sum_{j=1}^{n} \omega_{ij}^2 E_{ij}^2}{\partial u_y} = 0 \end{cases} \tag{3-25}$$

Equation 3-25 can be rewritten as:

$$\begin{cases} a_{11} u_x + a_{12} u_y = b_1 \\ a_{21} u_x + a_{22} u_y = b_2 \end{cases} \tag{3-26}$$

where

$$\begin{aligned} a_{11} &= \sum_{j=1}^{n} \omega_{ij}^2 dx_{ij}^2 \\ a_{22} &= \sum_{j=1}^{n} \omega_{ij}^2 dy_{ij}^2 \\ a_{12} = a_{21} &= \sum_{j=1}^{n} \omega_{ij}^2 dx_{ij}\, dy_{ij} \\ b_1 &= \sum_{j=1}^{n} \omega_{ij}^2 d\psi_{ij}\, dx_{ij} \end{aligned} \tag{3-27}$$

$$b_2 = \sum_{j=1}^{n} \omega_{ij}^2 d\psi_{ij}\, dy_{ij}$$

Equation 3-26 can be solved using Cramer's rule. The determination of the system is given by:

$$DET = a_{11}a_{22} - a_{12}a_{21} \qquad 3\text{-}28$$

If the determinant is non-zero, the gradient solution is given by:

$$\begin{cases} u_x = \dfrac{b_1 a_{22} - b_2 a_{12}}{DET} \\ u_y = \dfrac{b_2 a_{11} - b_1 a_{21}}{DET} \end{cases} \qquad 3\text{-}29$$

For the unweighted cases ($\omega_{ij} = 1$), the determinant corresponds to a difference in quantities of the order $O(dx^6)$, which may lead to an ill-conditioned system ($DET = 0$). In this case, an alternative method such as QR factorization can be used to obtain the solution. When the inverse distance weighting ($\omega_{ij} = 1/\sqrt{dx_{ij}^2 + dy_{ij}^2}$) is used, the determinant scales as $O(1)$, and the system is much better conditioned.

Though LS-GRM for node i is unrelated to the mesh topology, a commonly used method is to select the neighboring nodes in the first stencil layer that directly connect to the node i. As shown in Figure 3-1 (g), node *i1* to node *i6* are selected to calculate the gradient of node i. Alternatively, the user can select both the nodes in both first and second stencil layers to calculate the gradient of node i, as shown in Figure 3-1 (g) where node *i1* to node *i19* are selected.

3.2.3 High Order Least-Squares Gradient Reconstruction Method

Unlike GG-GRM and LS-GRM, which calculate the gradient at the nodes and support first order partial derivatives only, the high order least squares gradient reconstruction method (HLS-GRM) calculates gradients directly at the center of the control volume interface, with support of higher order partial derivatives.

HLS-GRM is based on the truncated Taylor series expansion of the function ψ for the control volume i, which can be written as (Pasdunkorale and Turner 2005, Sejekan 2016):

$$\psi_i = \psi_P + \left.\frac{\partial \psi}{\partial x}\right|_P dx_{Pi} + \left.\frac{\partial \psi}{\partial y}\right|_P dy_{Pi} + \left.\frac{\partial^2 \psi}{\partial x^2}\right|_P \frac{dx_{Pi}^2}{2} + \left.\frac{\partial^2 \psi}{\partial x \partial y}\right|_P dx dy_{Pi} + \left.\frac{\partial^2 \psi}{\partial y^2}\right|_P \frac{dy_{Pi}^2}{2} + \cdots \qquad 3\text{-}30$$

where $dx_{Pi} = x_i - x_P$, with similar expressions for dy_{Pi}. The final least-squares system is formed for every neighboring node within the stencil of the control volume i, by collating together all Taylor expansions of function ψ:

$$\begin{bmatrix} \omega_{P1} & \omega_{P1}dx_{P1} & \omega_{P1}dy_{P1} & \omega_{P1}dx_{P1}^2 & \omega_{P1}dxdy_{P1} & \omega_{P1}dy_{P1}^2 & \cdots \\ \omega_{P2} & \omega_{P2}dx_{P2} & \omega_{P2}dy_{P2} & \omega_{P2}dx_{P2}^2 & \omega_{P2}dxdy_{P2} & \omega_{P2}dy_{P2}^2 & \cdots \\ \omega_{P3} & \omega_{P3}dx_{P3} & \omega_{P3}dy_{P3} & \omega_{P3}dx_{P3}^2 & \omega_{P3}dxdy_{P3} & \omega_{P3}dy_{P3}^2 & \cdots \\ \vdots & \vdots & \vdots & \vdots & \vdots & \vdots & \ddots \\ \omega_{Pn} & \omega_{Pn}dx_{Pn} & \omega_{Pn}dy_{Pn} & \omega_{Pn}dx_{Pn}^2 & \omega_{Pn}dxdy_{Pn} & \omega_{Pn}dy_{Pn}^2 & \cdots \end{bmatrix} \begin{pmatrix} \psi \\ \frac{\partial\psi}{\partial x} \\ \frac{\partial\psi}{\partial y} \\ \frac{\partial^2\psi}{2\partial x^2} \\ \frac{\partial^2\psi}{\partial x\partial y} \\ \frac{\partial^2\psi}{2\partial y^2} \\ \vdots \end{pmatrix}_P = \begin{pmatrix} \omega_{P1}\psi_1 \\ \omega_{P2}\psi_2 \\ \omega_{P3}\psi_3 \\ \vdots \\ \omega_{Pn}\psi_n \end{pmatrix}$$

3-31

where ω_{Pi} is the spatial weighting, similar to Equation 3-23. Typically, inverse distance weighting is used. Equation 3-31 is over determined and can be written as $\mathrm{AX} = \mathrm{B}$. Since A is purely geometrical and mesh dependent, the solution can be sped up by precomputing and storing the pseudo-inverse of matrix A. The solution is obtained by $\mathrm{X} = \mathrm{A}^{-1}\mathrm{B}$, where A^{-1} is the pseudo-inverse of matrix A.

Similar as for LS-GRM, different stencil layers can be used in the gradient reconstruction for control volume interface center P. As shown in Figure 3-1 (g), nodes *i, i1* and *i2* are in the first stencil layer of center point P and node *i3* to *i19* are in the second and third stencil layer. It is worth mentioning that by ignoring the high order partial derivatives ($\frac{\partial^2\psi}{\partial x^2}, \frac{\partial^2\psi}{\partial x\partial y}, \frac{\partial^2\psi}{\partial y^2}, \cdots$), Equation 3-31 is reduced to a general linear system, if only the nodes in the first stencil layer are used.

3.2.4 MPFA Upstream Weighting

To calculate the flux through each control volume face, as shown in Equation 3-8, estimation of flow parameters (e.g., density, relative permeability) at the center of the control volume face are required. For nonlinear unsaturated flow, calculation of relative permeability at the center of the control volume face plays an important role in the monotonicity of a discrete scheme and its convergence behavior. Despite introducing numerical dispersion, upstream weighting is widely used to ensure the monotonicity of the scheme (Forsyth and Kropinski 1997, Younes et al. 2013). For the TPFA method, the upstream point can be easily determined by comparing the two nodal pressures. In the MPFA method, two or more nodes are used for gradient reconstruction and consequently the upstream pressure cannot be obtained directly.

For the primary term calculation, as shown in Equation 3-14, conventional two-point upstream weighting is applied when substituting this term into Equation 3-8. However, the secondary term may have a different flux direction compared to the primary term when the MPFA method is used, especially within region of the wetting front, where sharp gradients exist. In this case, standard two-point upstream weighting cannot guarantee monotonicity and can cause difficulty in convergence. To alleviate these issues, the multi-point upstream (MPUPS) weighting based on the sign of the secondary term is introduced. When the secondary term is positive, the cross-diffusion flux is from *node j* to *node i* and *node j* is selected as the upstream point when

substituting the secondary term into Equation 3-8. Similarly, *node i* is selected as the upstream point when the secondary term is negative. In the case of MPUPS, the primary and secondary terms in Equation 3-14 have the same upstream point if they have the same flux direction. If these two terms have opposite flux directions, different points are used as the upstream point. This rule guarantees the monotonicity for all flux components across control volume faces.

It is worth mentioning that the MPFA-GRM satisfies flux continuity and potential continuity. In GG-GRM, the potential gradient is linear over the control volume while in LS-GRM and HLS-GRM, the potential gradient is nonlinear over the control volume.

3.3 Hybrid MPI-OpenMP Parallelization

Parallelization of MIN3P-THCm V2.0 was based on MIN3P-THCm V1.1 (Su et al. 2017), a general-purpose parallel code based on the domain decomposition method using MPI. For MIN3P-THCm V2.0, the parallel scheme was further refined by adding threading acceleration using OpenMP, as shown in Figure 3-2. The optimized parallel code allows the use of OpenMP, MPI and hybrid MPI-OpenMP. With these features, different parallel schemes can be used for simulation tasks with different scale and complexity.

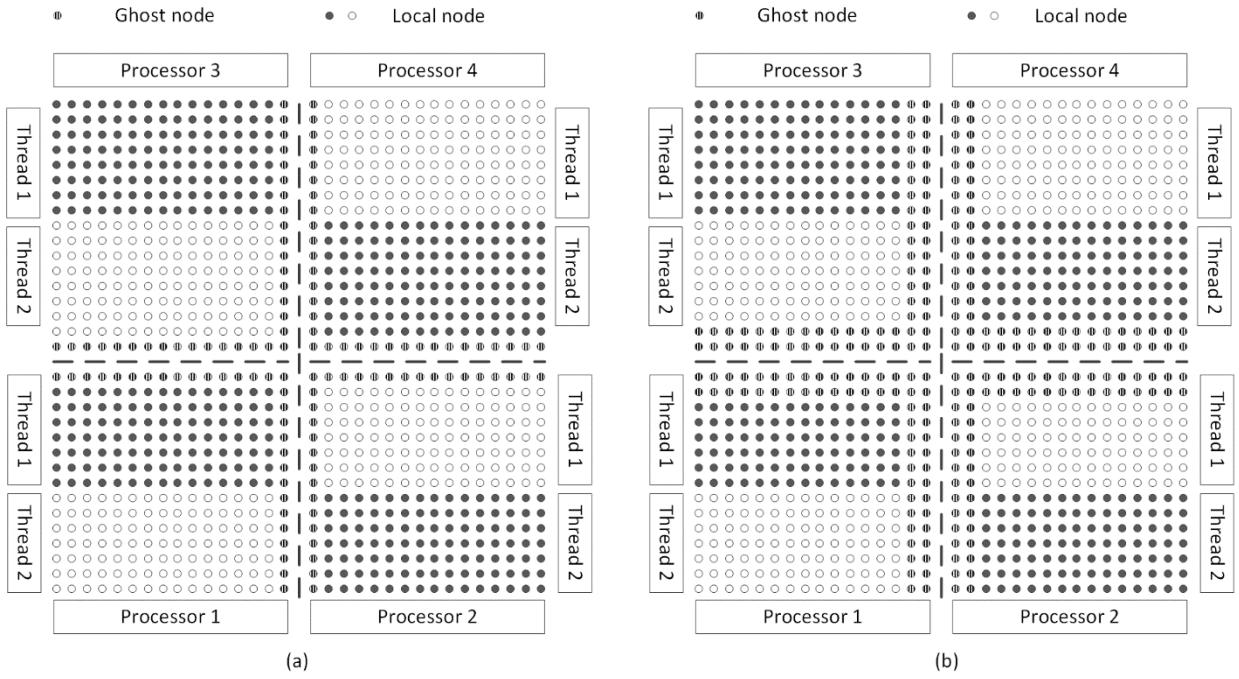

Figure 3-2: Conceptual Illustration of Hybrid MPI-OpenMP Parallelization Scheme (a) Stencil Width 1, and (b) Stencil Width 2

An overlapping domain decomposition of the unstructured grid is implemented based on PETSc's (Balay et al. 2018) DMPlex module. Overlapping domain decomposition methods are used for efficiency and flexibility. Domain decomposition for unstructured grid requires overlap of one or more nodes if using the Green-Gauss gradient reconstruction or second order least squares gradient reconstruction methods. For higher order least squares gradient reconstruction, two or more nodes must overlap between adjacent sub-domains. There is no

additional message communication required to obtain data from a neighbouring subdomain since each subdomain has local copies of all data associated with the ghost nodes/cells. For each subdomain, OpenMP threading acceleration is used. An example of hybrid MPI-OpenMP domain decomposition for unstructured meshes is shown in Figure 3-3.

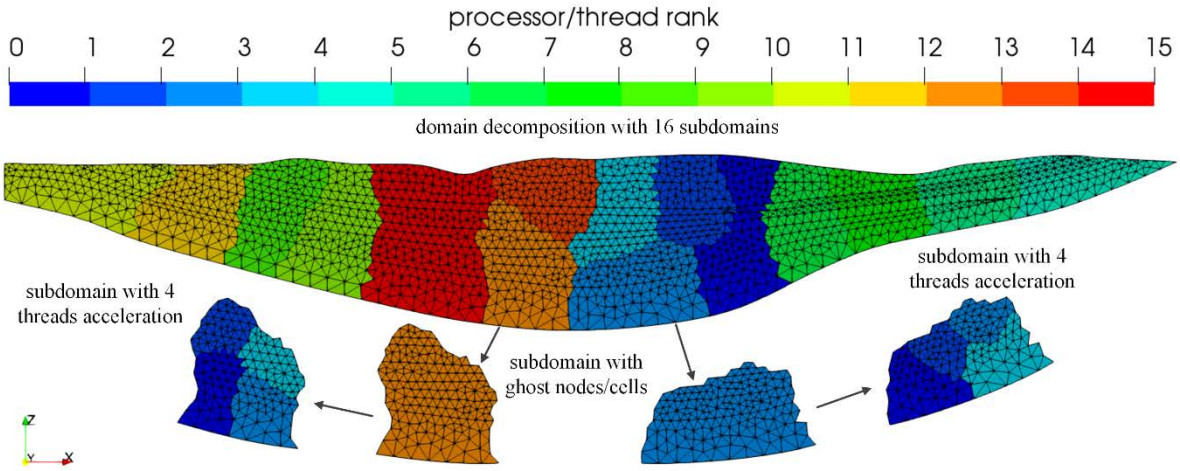

Figure 3-3: Illustration of Hybrid MPI-OpenMP Domain Decomposition for An Unstructured Mesh

The parallelized version of the code can be run in three modes: with thread acceleration only, the code runs in OpenMP parallelization; with domain decomposition only, the code runs in MPI parallelization; and by using a combination of thread acceleration and domain decomposition, the code runs in hybrid MPI-OpenMP parallelization. The hybrid MPI-OpenMP parallelization can take advantage of MPI scalability but simultaneously reducing communication overhead by using OpenMP. In addition to the default PETSc parallel solver packages included in ParMIN3P-THCm, an alternative linear iterative solver (LIS) (Fujii et al. 2005, Kotakemori et al. 2005, Nishida 2010) has been implemented in the code that can support OpenMP, MPI and hybrid MPI-OpenMP. System input and output (IO) is usually a bottleneck in the parallel code. In MIN3P-THCm V2.0, HDF5 and XDMF data file formats are used to support efficient parallel IO. The workflow of MIN3P-THCm V2.0 parallelization remains the same as MIN3P-THCm V1.1 with the aforementioned new features added, as shown in Figure 3-4.

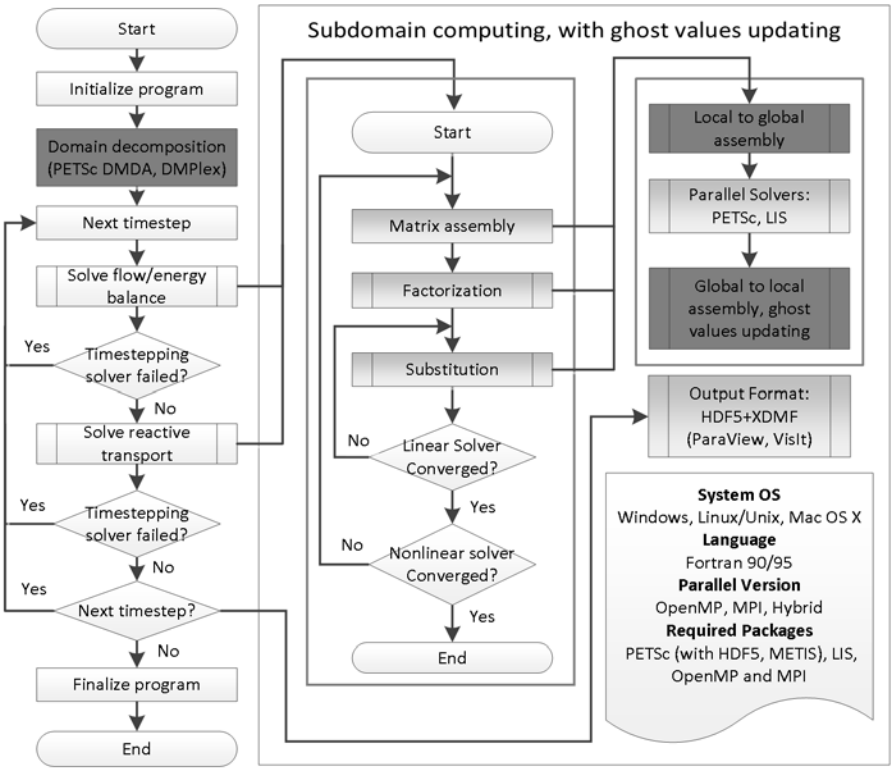

Figure 3-4: Workflow of MIN3P-THCm V2.0 Parallelization

4. Analysis of MPFA Method for Variably Saturated Flow

A series of numerical tests were carried out to investigate the versatility of the proposed MPFA-GRM scheme. The results of these tests are presented in this section. The monotonicity and convergence behavior were analyzed considering a wide range of parameters and methods including heterogeneity, anisotropy, control volume types, gradient reconstruction methods, flux approximation methods and spatial weighting methods, as shown in Table 4-1. Given the same mesh and material properties, 134 simulations were carried out, representing various combinations of the selected parameters and methods, as shown in Table 4-2.

Table 4-1: Numerical Options Used for Versatility Testing and Validation of MPFA-GRM Scheme

Candidate	Options
Control volume type	SG[1], MD, VD, CC
Center of control volume face[2]	HFC, IHFE
Flux approximation method	TPFA, MPFA
Gradient reconstruction method[3]	GG, LS, HLS2, HLS3, HLS4, HLS3e[4], HLS4e[4]
Spatial weighting	Center, Upstream (UPS), MPFA Upstream (MPUPS)[5]

[1] for structured mesh only

[2] HFC and IHFE have the same effect for TPFA method

[4] including high order Taylor expansion remainder

[3,5] for MPFA method only

Table 4-2: Simulation Scenarios for Analysis and Validation of MPFA-GRM Scheme

No.	Scenario	No.	Case Scenario	No.	Case Scenario
1	cc-gg-hfc-mpfa-center	19	cc-ls-hfc-mpfa-center	37	cc-hls2-hfc-mpfa-center
2	cc-gg-hfc-mpfa-mpups	20	cc-ls-hfc-mpfa-mpups	38	cc-hls2-hfc-mpfa-mpups
3	cc-gg-hfc-mpfa-ups	21	cc-ls-hfc-mpfa-ups	39	cc-hls2-hfc-mpfa-ups
4	cc-gg-ihfe-mpfa-center	22	cc-ls-ihfe-mpfa-center	40	cc-hls2-ihfe-mpfa-center
5	cc-gg-ihfe-mpfa-mpups	23	cc-ls-ihfe-mpfa-mpups	41	cc-hls2-ihfe-mpfa-mpups
6	cc-gg-ihfe-mpfa-ups	24	cc-ls-ihfe-mpfa-ups	42	cc-hls2-ihfe-mpfa-ups
7	md-gg-hfc-mpfa-center	25	md-ls-hfc-mpfa-center	43	md-hls2-hfc-mpfa-center
8	md-gg-hfc-mpfa-mpups	26	md-ls-hfc-mpfa-mpups	44	md-hls2-hfc-mpfa-mpups
9	md-gg-hfc-mpfa-ups	27	md-ls-hfc-mpfa-ups	45	md-hls2-hfc-mpfa-ups
10	md-gg-ihfe-mpfa-center	28	md-ls-ihfe-mpfa-center	46	md-hls2-ihfe-mpfa-center
11	md-gg-ihfe-mpfa-mpups	29	md-ls-ihfe-mpfa-mpups	47	md-hls2-ihfe-mpfa-mpups
12	md-gg-ihfe-mpfa-ups	30	md-ls-ihfe-mpfa-ups	48	md-hls2-ihfe-mpfa-ups
13	vd-gg-hfc-mpfa-center	31	vd-ls-hfc-mpfa-center	49	vd-hls2-hfc-mpfa-center
14	vd-gg-hfc-mpfa-mpups	32	vd-ls-hfc-mpfa-mpups	50	vd-hls2-hfc-mpfa-mpups
15	vd-gg-hfc-mpfa-ups	33	vd-ls-hfc-mpfa-ups	51	vd-hls2-hfc-mpfa-ups
16	vd-gg-ihfe-mpfa-center	34	vd-ls-ihfe-mpfa-center	52	vd-hls2-ihfe-mpfa-center
17	vd-gg-ihfe-mpfa-mpups	35	vd-ls-ihfe-mpfa-mpups	53	vd-hls2-ihfe-mpfa-mpups
18	vd-gg-ihfe-mpfa-ups	36	vd-ls-ihfe-mpfa-ups	54	vd-hls2-ihfe-mpfa-ups
55	cc-hls3-hfc-mpfa-center	73	cc-hls3e-hfc-mpfa-center	91	cc-hls4-hfc-mpfa-center
56	cc-hls3-hfc-mpfa-mpups	74	cc-hls3e-hfc-mpfa-mpups	92	cc-hls4-hfc-mpfa-mpups
57	cc-hls3-hfc-mpfa-ups	75	cc-hls3e-hfc-mpfa-ups	93	cc-hls4-hfc-mpfa-ups
58	cc-hls3-ihfe-mpfa-center	76	cc-hls3e-ihfe-mpfa-center	94	cc-hls4-ihfe-mpfa-center
59	cc-hls3-ihfe-mpfa-mpups	77	cc-hls3e-ihfe-mpfa-mpups	95	cc-hls4-ihfe-mpfa-mpups
60	cc-hls3-ihfe-mpfa-ups	78	cc-hls3e-ihfe-mpfa-ups	96	cc-hls4-ihfe-mpfa-ups
61	md-hls3-hfc-mpfa-center	79	md-hls3e-hfc-mpfa-center	97	md-hls4-hfc-mpfa-center
62	md-hls3-hfc-mpfa-mpups	80	md-hls3e-hfc-mpfa-mpups	98	md-hls4-hfc-mpfa-mpups
63	md-hls3-hfc-mpfa-ups	81	md-hls3e-hfc-mpfa-ups	99	md-hls4-hfc-mpfa-ups
64	md-hls3-ihfe-mpfa-center	82	md-hls3e-ihfe-mpfa-center	100	md-hls4-ihfe-mpfa-center
65	md-hls3-ihfe-mpfa-mpups	83	md-hls3e-ihfe-mpfa-mpups	101	md-hls4-ihfe-mpfa-mpups
66	md-hls3-ihfe-mpfa-ups	84	md-hls3e-ihfe-mpfa-ups	102	md-hls4-ihfe-mpfa-ups
67	vd-hls3-hfc-mpfa-center	85	vd-hls3e-hfc-mpfa-center	103	vd-hls4-hfc-mpfa-center
68	vd-hls3-hfc-mpfa-mpups	86	vd-hls3e-hfc-mpfa-mpups	104	vd-hls4-hfc-mpfa-mpups
69	vd-hls3-hfc-mpfa-ups	87	vd-hls3e-hfc-mpfa-ups	105	vd-hls4-hfc-mpfa-ups
70	vd-hls3-ihfe-mpfa-center	88	vd-hls3e-ihfe-mpfa-center	106	vd-hls4-ihfe-mpfa-center
71	vd-hls3-ihfe-mpfa-mpups	89	vd-hls3e-ihfe-mpfa-mpups	107	vd-hls4-ihfe-mpfa-mpups
72	vd-hls3-ihfe-mpfa-ups	90	vd-hls3e-ihfe-mpfa-ups	108	vd-hls4-ihfe-mpfa-ups
109	cc-hls4e-hfc-mpfa-center	127	cc-gg-hfc-tpfa-center	133	sg-center

110	cc-hls4e-hfc-mpfa-mpups	128	cc-gg-hfc-tpfa-ups	134	sg-ups
111	cc-hls4e-hfc-mpfa-ups	129	md-gg-hfc-tpfa-center		
112	cc-hls4e-ihfe-mpfa-center	130	md-gg-hfc-tpfa-ups		
113	cc-hls4e-ihfe-mpfa-mpups	131	vd-gg-hfc-tpfa-center		
114	cc-hls4e-ihfe-mpfa-ups	132	vd-gg-hfc-tpfa-ups		
115	md-hls4e-hfc-mpfa-center				
116	md-hls4e-hfc-mpfa-mpups				
117	md-hls4e-hfc-mpfa-ups				
118	md-hls4e-ihfe-mpfa-center				
119	md-hls4e-ihfe-mpfa-mpups				
120	md-hls4e-ihfe-mpfa-ups				
121	vd-hls4e-hfc-mpfa-center				
122	vd-hls4e-hfc-mpfa-mpups				
123	vd-hls4e-hfc-mpfa-ups				
124	vd-hls4e-ihfe-mpfa-center				
125	vd-hls4e-ihfe-mpfa-mpups				
126	vd-hls4e-ihfe-mpfa-ups				

4.1 Case I: Water Table Mounding in Isotropic Soil

In this part, the MPFA-GRM method is used to simulate variably saturated flow based on a laboratory experiment simulating infiltration and water table mounding (Vauclin et al. 1979, Clement et al. 1994). The spatial domain is 6.00 m x 2.00 m, with an initial horizontal water table located at the height of 0.65 m. At the surface of the domain, a constant flux (3.55 m/day) is applied over a width of 1 m in the center. Due to symmetry, the modeled portion of the domain is 3.00 m x 2.00 m, with no-flow boundaries on the bottom and on the left side. The remaining section of the top boundary above the water table and on the right side of the domain are no-flow boundaries. Observation point *P1* is located 0.3 m from the left boundary and 0.2 m below the top surface, and observation point *P2* is located close to the water table 0.8 m from the left boundary and 0.8 m below the top surface. A conceptual illustration of the simulation domain is shown in Figure 4-1. For the structured mesh, the nodal spacing is 0.05 m in the x and z directions, while for the unstructured mesh, the average nodal spacing is 0.05 m. This results in a total number of control volumes of 2501 for the structured mesh and 3269 for the unstructured mesh.

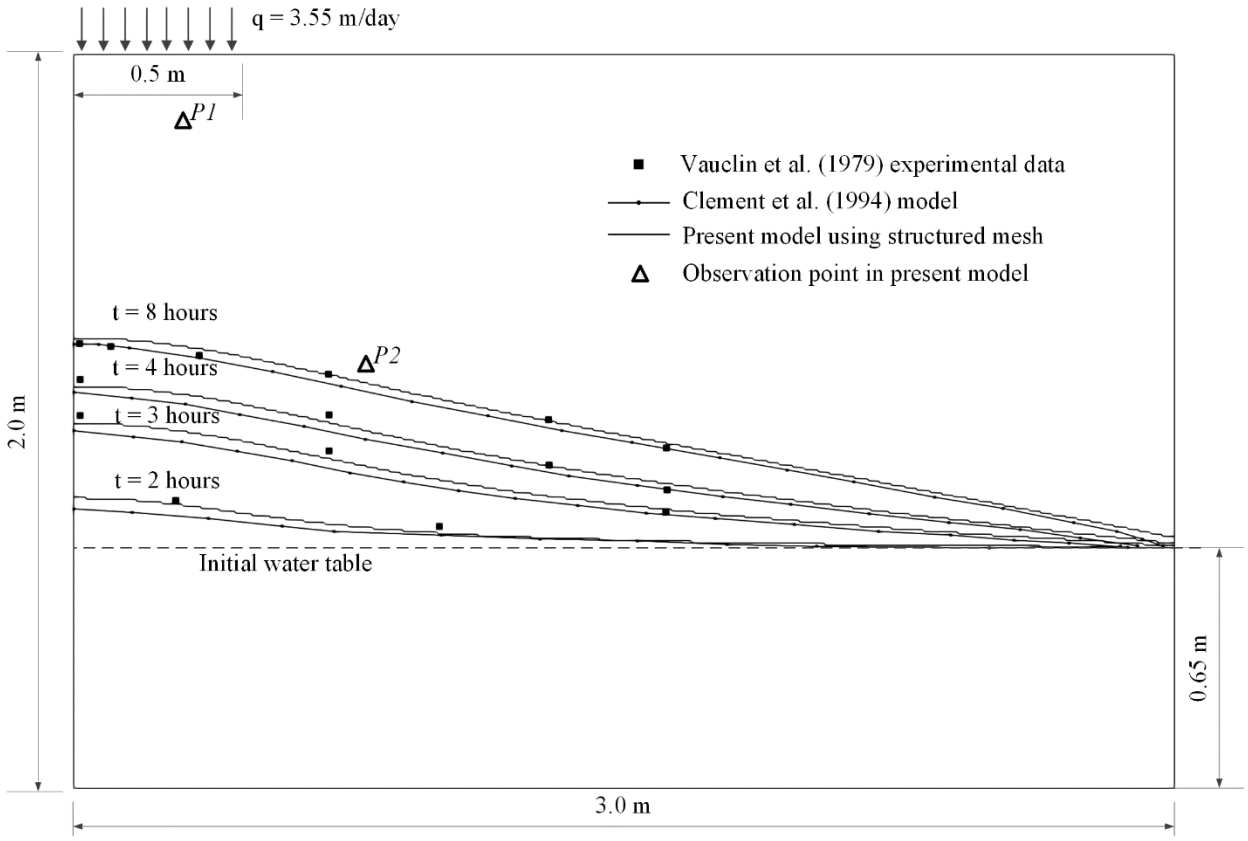

Figure 4-1: Illustration of Modeling Domain and Results for Simulation of Transient, Water Table Mounding Constrained by Data from Vauclin et al. (1979)

The soil properties used in the model are homogeneous and isotropic, with a saturated hydraulic conductivity of 8.40 m/day, a porosity of 0.30, and a residual saturation of 0.01. The estimated values of Van Genuchten soil parameters are $\alpha = 3.3$ m^{-1}, $n = 4.1$ and specific storage is ignored (Vauclin et al. 1979, Clement et al. 1994).

A comparison of transient water table positions obtained by the present model, Clement et al. (1994), and the experimental data collected by Vauclin et al. (1979) is shown in Figure 4-1, which illustrates that there is good agreement between the numerical models and the experimental data. In the present research, we use results obtained from structured mesh as the reference results based on previous code verification (Mayer et al. 2002, Henderson et al. 2009, Mayer and MacQuarrie 2010, Bea et al. 2012, 2018, Su et al. 2017). Another reason for utilizing these results as a reference is that the structured mesh is K-orthogonal yielding relatively small errors due to numerical discretization.

As aforementioned, the lack of monotonicity in unsaturated flow often yields non-physical oscillations near sharp wetting fronts. These oscillations can have a dramatic effect on the convergence behavior of the numerical model. We are most interested in comparing results near the wetting front, where sharp gradients exist and oscillations may occur. To evaluate the various options, the results obtained using different numerical methods, as listed in Table 4-2: , are compared to those obtained using a structured mesh.

4.1.1 Temporal Evolution of Water Saturations at Observation Points

The results obtained by GG-GRM are depicted for the two observation points (Figure 4-2). The changes of water saturation obtained using different numerical methods for the two observation points are in excellent agreement with each other. Smooth changes of water saturation over time indicate that oscillations are not occurring at the selected observation points. Similar results are obtained for scenarios using other gradient reconstruction methods.

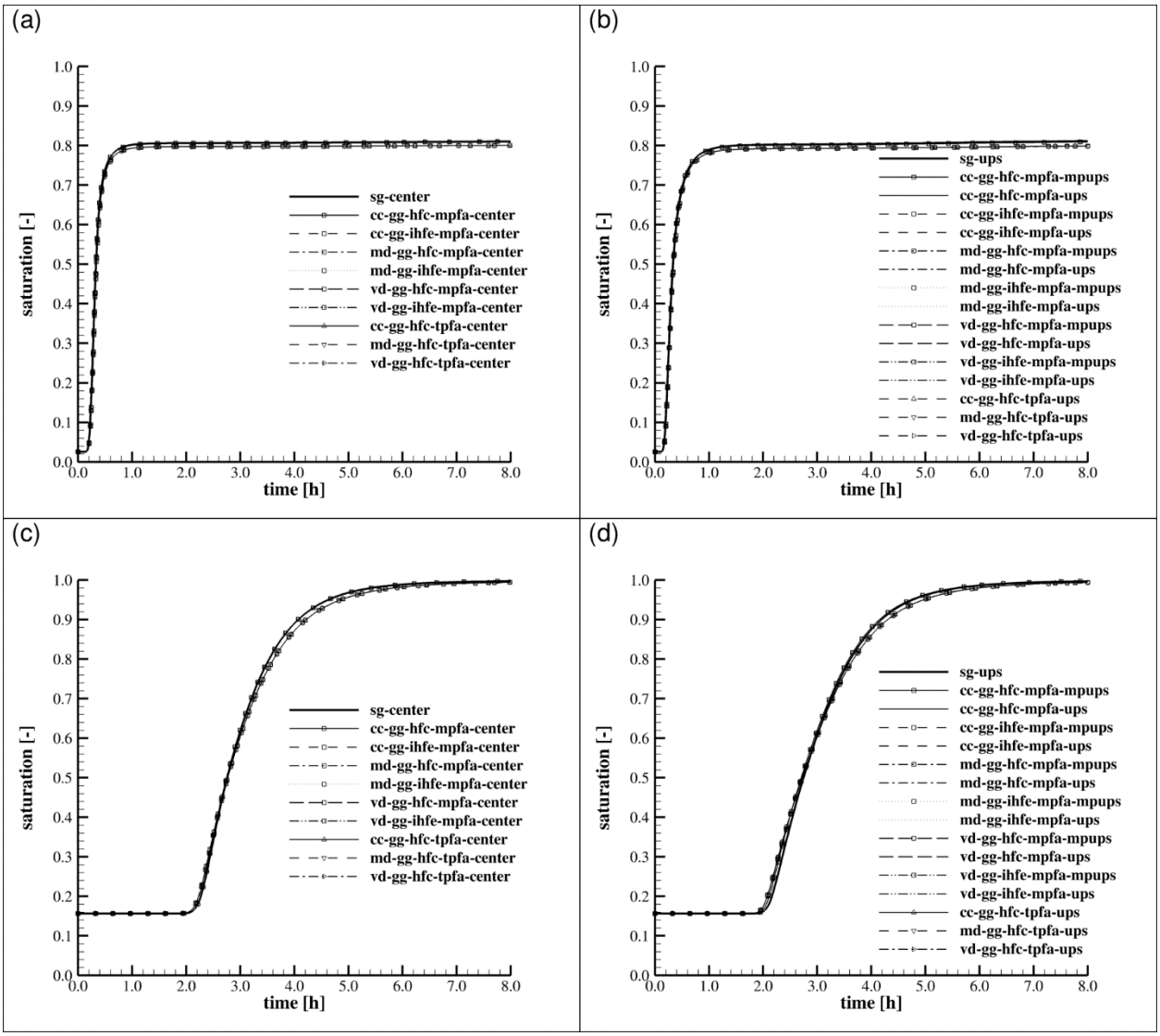

Figure 4-2: Transient Changes of Water Saturations at Observation Points P1 and P2 Obtained for Case I Using Different Numerical Methods, (a) P1 Based on Centered Weighting, (b) P1 Based on Upstream and Multipoint Upstream Weighting, (c) P2 Based on Centered Weighting, (d) P2 Based on Upstream and Multipoint Upstream Weighting

4.1.2 Spatial Distribution of Water Saturation

Although water saturations did not suffer from oscillations at the observation points, it is interesting to observe that non-physical oscillations of water saturation are possible in space, depending on the numerical scheme. After a period of 8 hours, simulated water saturations using different numerical schemes are generally in good agreement with each other. However, for CC and MD control volume types, oscillations near the wetting front are observed for both centered weighting and upstream weighting. For the VD control volume type, the simulation results indicate excellent agreement with results obtained by structured mesh. There is no significant difference between centered, upstream and multi-point upstream weighting. The simulation results also show that the accuracy of TPFA and MPFA methods are almost identical in this case.

Mesh resolution plays an important role in the accuracy of numerical results. To analyze the effect of grid resolution, four different meshes were used to test the effect of mesh resolution and refinement. The first mesh is the same as the one used above, with average nodal spacing 0.05 m. The second mesh is slightly different from the first mesh by adjusting some nodes but has the same resolution. The third mesh has a resolution of 0.025 m. The fourth mesh is based on the third mesh, but local refinement is applied to the top left region with a resolution of 0.005 m. The number of nodes in these four meshes are 3272, 3269, 12825 and 54725, respectively. A comparison of contour plots of water saturation after a period of 8 hours using different mesh resolutions and refinement is shown in Figure 4-3: . By comparing the results obtained from mesh 4 to the results obtained from mesh 1 to mesh 3, we can find that, for CC and MD control volume types, the oscillation in the wetting front can be improved by using a mesh with higher resolution and local refinement. The results also indicate that for the meshes with the same resolution, the nature of oscillations can be quite different. However, for the VD control volume type, there is no oscillation for either the coarse mesh nor the refined mesh. Similar results are obtained by using different gradient reconstruction methods, indicating that the gradient reconstruction method does not help in improving the oscillation problem at the wetting front.

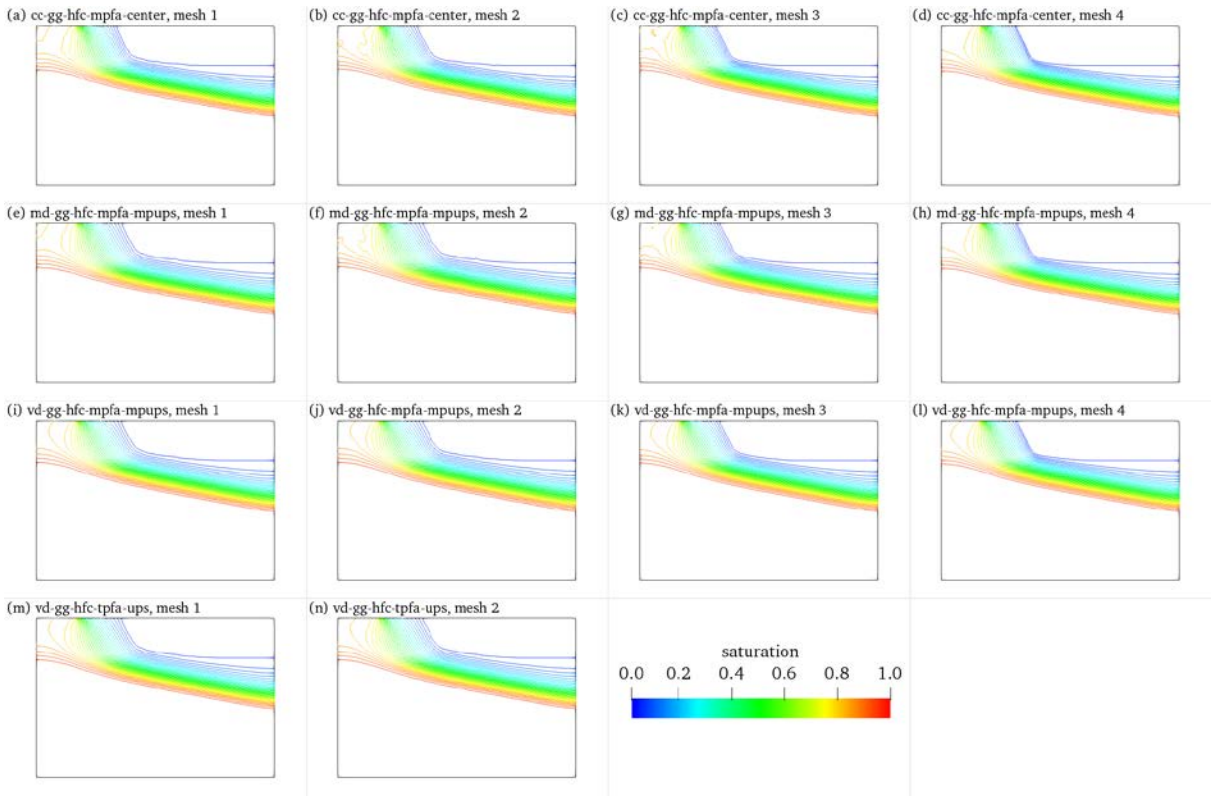

Figure 4-3: Comparison of Contour Plots of Water Saturation After a Period of 8 Hours in Case I Using Different Mesh Resolution and Refinement, (a) to (d) Cell Center Control Volume Type with Centered Weighting, (e) to (h) Medial Dual Control Volume Type with Multi-point Upstream Weighting, (i) to (l) Voronoi Diagram Control Volume Type with Multi-point Upstream Weighting, (m) and (n) Voronoi Diagram Control Volume Type with TPFA Flux Approximation and Upstream Weighting

4.2 Case II: Water Table Mounding in Anisotropic Soil

For this scenario, Case I was modified to demonstrate the ability of the MPFA-GRM method for simulating variably saturated flow in porous media with anisotropic material properties. The physical parameters, initial conditions and boundary conditions are the same as those used in Case I, except that the horizontal hydraulic conductivity was changed to 84.0 m/day while the vertical hydraulic conductivity was remained 8.4 m/day.

4.2.1 Transient Water Saturation for Observation Points

Temporal changes of water saturations obtained with different gradient reconstruction using different numerical methods and mesh resolution are shown in Figure 4-4. The results indicate that for the simulation with anisotropic material properties, the TPFA cannot generate correct results, compared to the results obtained from structured mesh. The numerical error using TPFA cannot be improved by using a grid with higher resolution. For the MPFA method, it can be observed that results based on centered weighting are in excellent agreement with each other. However, the results based on multi-point upstream weighing differ from each other. As shown in Figure 4-4(b) and (f), transient changes of water saturation for *P1* generally match each other. However, for *P2*, the results based on the VD control volume type are of better

quality than results based on the CC and MD control volume types, when compared to the results based on the structured mesh. The numerical error can be improved by using meshes with higher resolution, as shown in Figure 4-4 (d) and (h). It should be noted that standard two-point upstream weighting encounters convergence problems, requiring very small time steps, making the simulation impractical to complete. Similar results are obtained for the other gradient reconstruction methods.

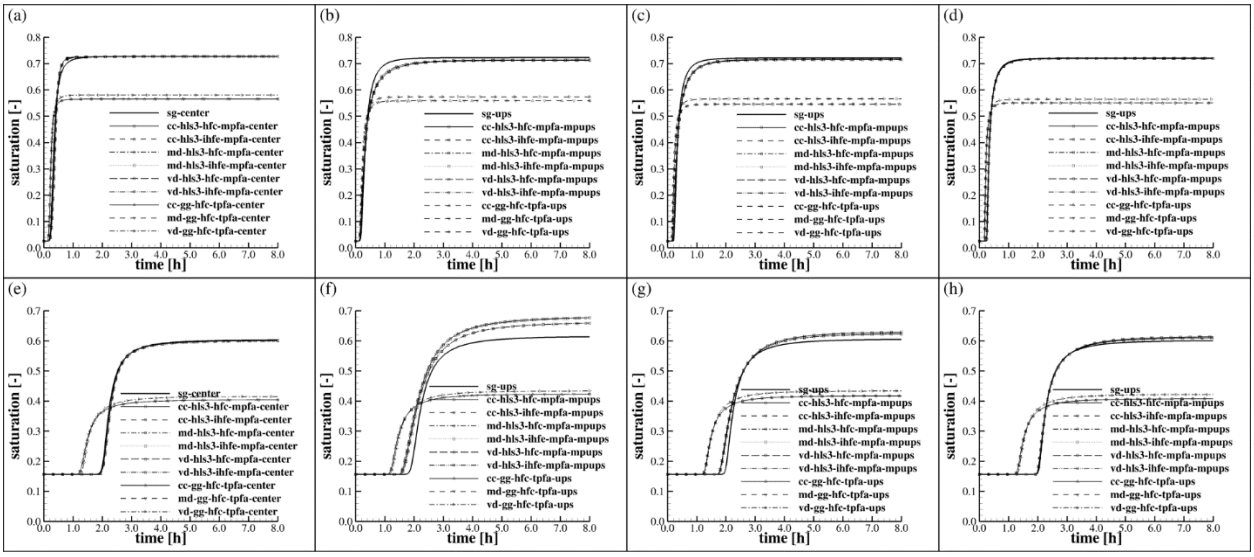

Figure 4-4: Transient Changes of Water Saturation for Observation Points P1 and P2 Obtained for Case II Using Different Numerical Methods and Mesh Resolutions, (a) P1 Based on Centered Weighting Using Mesh 1, (b) P1 Based on Upstream Weighting Using Mesh 1, (c) P1 Based on Upstream Weighting Using Mesh 3, (d) P1 Based on Upstream Weighting Using Mesh 4, (e) P2 Based on Centered Weighting Using Mesh 1, (f) P2 Based on Upstream Weighting using Mesh 1, (g) P2 Based on Upstream Weighting Using Mesh 3, and (h) P2 Based on Upstream Weighting Using Mesh 4

4.2.2 Spatial Distribution of Water Saturation

Contour plots of water saturation of Case II after a period of 8 hours using different numerical schemes are shown in Figure 4-5. Compared to the simulation results of Case I, the spatial distribution of water saturation here does not show non-physical oscillations for all simulations using the MPFA method. However, for simulations with the TPFA method, significant non-physical oscillations are observed, and the results lost accuracy compared to the MPFA and structured grid methods.

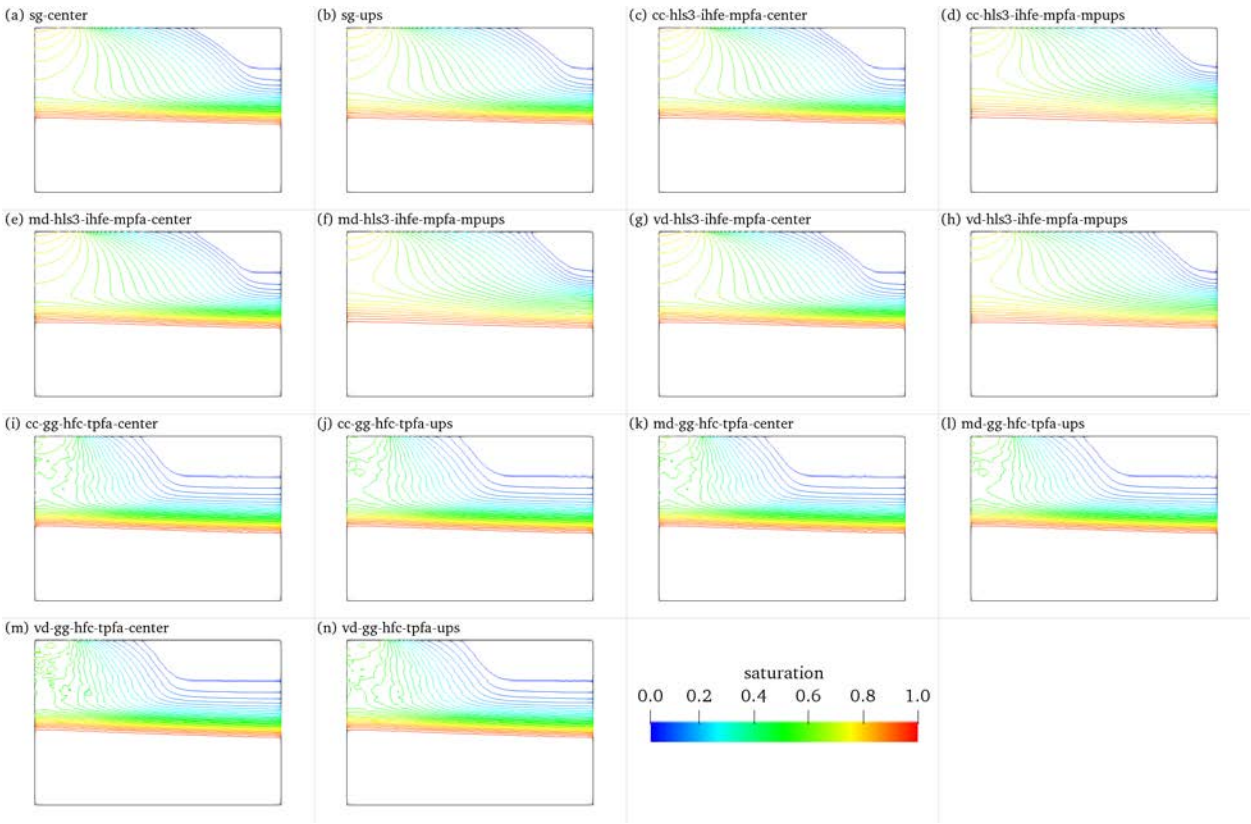

Figure 4-5: Contour Plots of Water Saturation After a Period of 8 Hours for Case II Using Different Numerical Schemes, (a) and (b) structured Mesh Using Centered Weighting and Upstream Weighting, (c) and (d) Unstructured Mesh with Cell-centered Control Volume Type Using Centered Weighting and Upstream Weighting, (e) and (f) Unstructured Mesh with Medial-dual Control Volume Type Using Centered Weighting and Upstream Weighting, (g) and (h) Unstructured Mesh with Voronoi-diagram Control Volume Type Using Centered Weighting and Upstream Weighting, (i) to (n) Same as (c) to (h), but Using Two Point Flux Approximation

4.3 Case III: Water Infiltration into a Heterogeneous Dry Soil

In this section, the MPFA-GRM method is used to simulate variably saturated flow in a heterogeneous soil with dry initial conditions. The test case deals with water infiltration into a very dry soil with initial pressure -880.0 kPa (Forsyth and Kropinski 1997). The spatial domain is 8.0 m x 6.5 m, which consists of 4 zones with different soil properties, as shown in Figure 4-6. All boundaries are impermeable, except the infiltration zone at the top left. The observation point *P1* is located at 2.0 m from the left boundary and 0.2 m below the top surface, and observation point *P2* is locates 0.4 m below *P1*. For the structured mesh, the nodal spacing is 0.1 m in the x and z directions while for the unstructured mesh, the average nodal spacing is 0.1 m. This results in the total number of control volumes of 5346 in the structured mesh and 6955 in the unstructured mesh.

The soil properties used in the model are shown in Table 4-3.

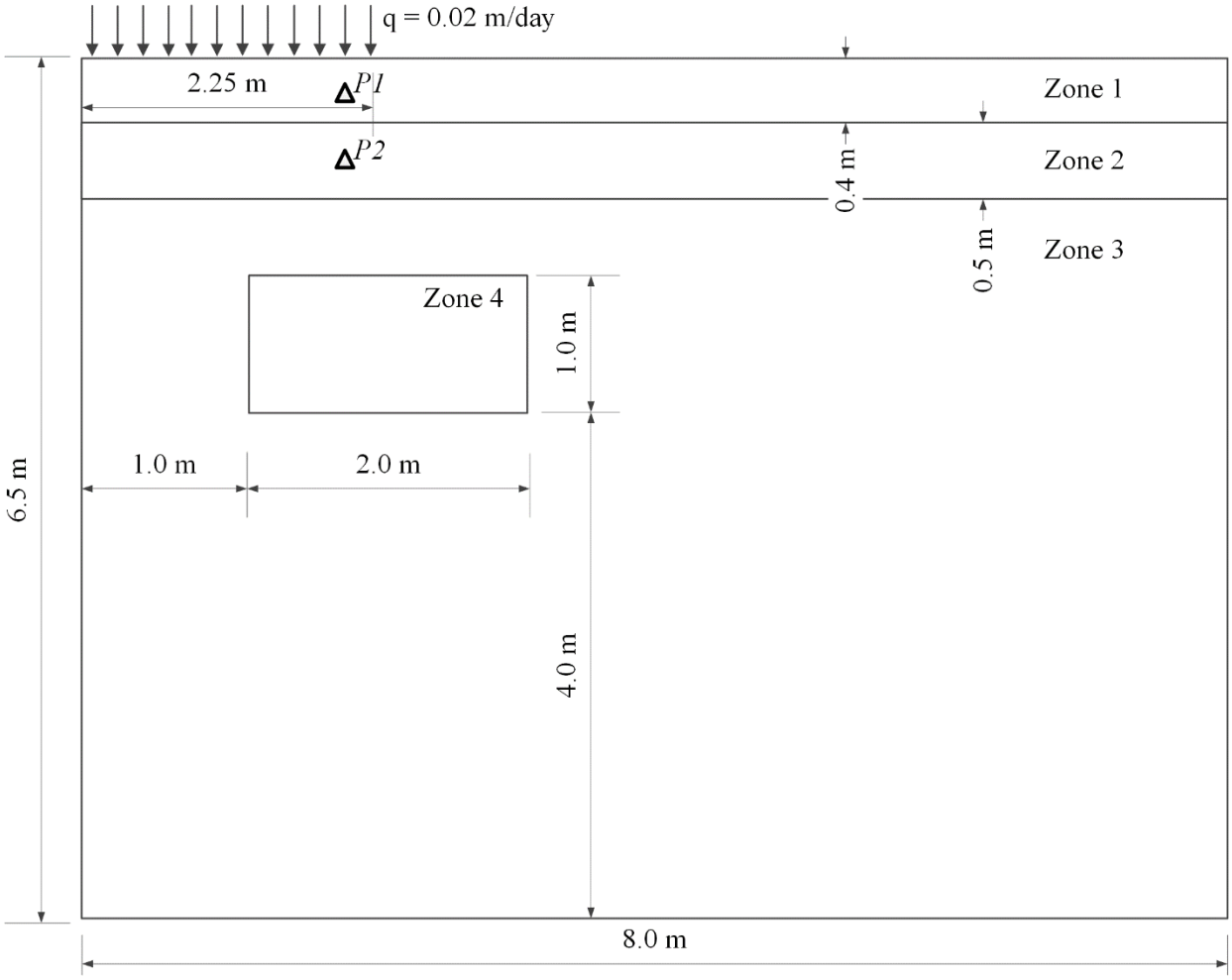

Figure 4-6: Spatial Domain of Water Infiltration into Very Dry Soil

Table 4-3: Material Properties for Water Infiltration into Very Dry Soil

Zone	$K_x = K_z$ (m s^{-1})	ϕ	S_r	α (m^{-1})	n
1	1.0×10^{-4}	3.70×10^{-1}	2.70×10^{-1}	3.34	1.98
2	6.1×10^{-5}	3.50×10^{-1}	2.80×10^{-1}	3.63	1.98
3	5.4×10^{-5}	3.30×10^{-1}	2.60×10^{-1}	3.45	5.00
4	5.4×10^{-4}	3.30×10^{-1}	2.60×10^{-1}	3.45	5.00

4.3.1 Transient Water Saturations at Observation Points

Similar to Cases I and II, simulating variably saturated flow in homogeneous soils, the changes of water saturation based on the different numerical schemes for the two observation points are in agreement with each other. The changes of water saturation for the two observation points are shown in Figure 4-7. It can be observed that the results obtained using the VD control volume type are in excellent agreement with the structured mesh. For CC and MD control volume types, the water saturation is slightly lower before reaching the maximum saturation, indicating that numerical dispersion for CC and MD control volume types is more significant than for VD control volume types.

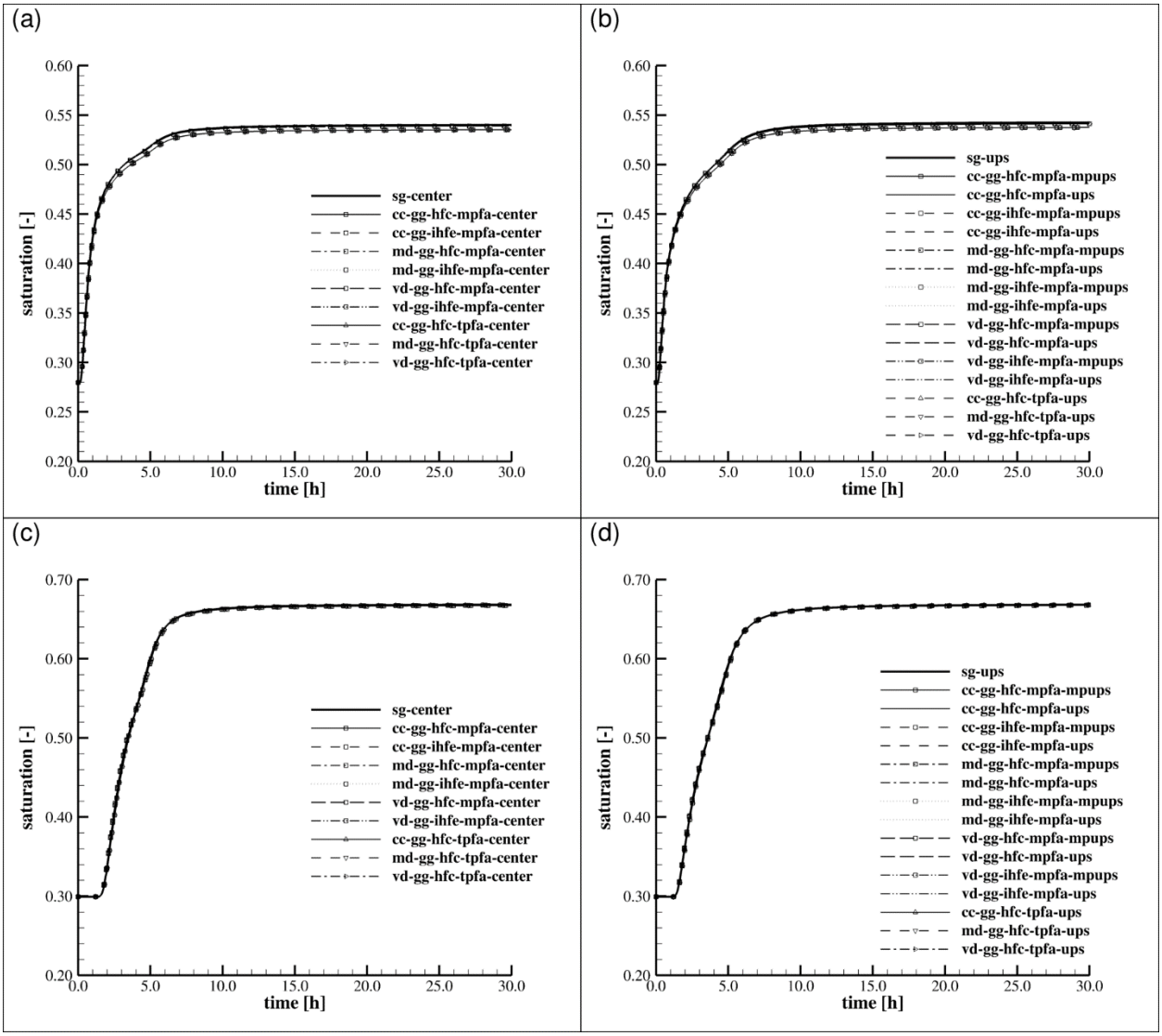

Figure 4-7: Transient Changes of Water Saturations for Observation Points P1 and P2 Obtained for Case III Using Different Numerical Methods, (a) P1 Based on Centered Weighting, (b) P1 Based on Upstream and Multipoint Upstream Weighting, (c) P2 Based on Centered Weighting, (d) P2 Based on Upstream and Multipoint Upstream Weighting

4.3.2 Spatial Distribution of Water Saturations

Although the transient changes of water saturations at the two observation points are smooth and in good agreement with each other, the spatial distribution of water saturations reveals that non-physical oscillation is possible. As shown in Figure 4-8, for CC and MD control volume types with MPFA flux approximation, significant oscillations are observed near the wetting front for both centered and upstream weighting. For the VD control volume type, the water saturations are oscillation-free and the results are well matched with that obtained from the structured mesh. Similar results are found for the TPFA method and other gradient reconstruction methods.

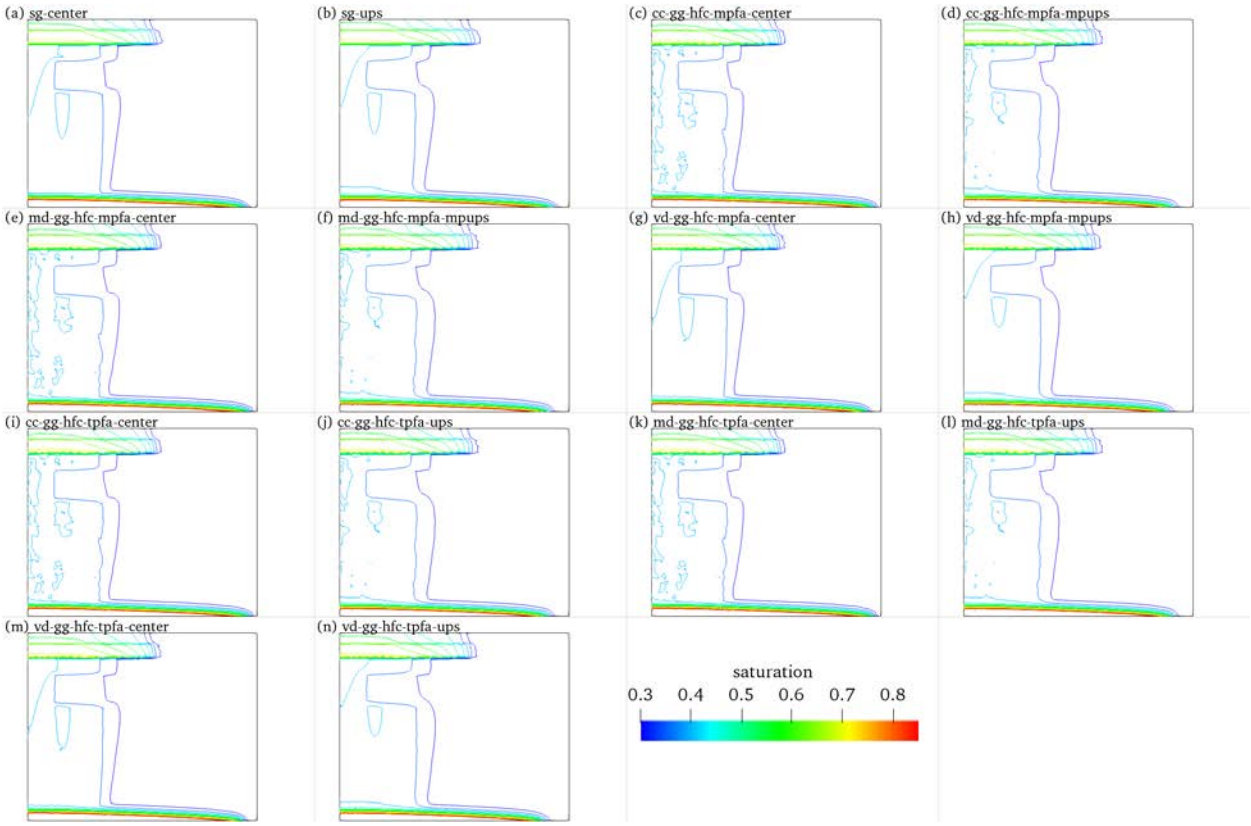

Figure 4-8: Contour Plots of Water Saturations After a Period of 30 Days for Case III Using Different Numerical Schemes as Listed in Appendix 1, (a) and (b) Structured Mesh Using Centered Weighting and Upstream Weighting, (c) and (d) Unstructured Mesh with Cell-centered Control Volume Type Using Centered Weighting and Upstream Weighting, (e) and (f) Unstructured Mesh with Medial-dual Control Volume Type Using Centered Weighting and Upstream Weighting, (g) and (h) Unstructured Mesh with Voronoi-diagram Control Volume Type Using Centered Weighting and Upstream Weighting, (i) to (n) Same as (c) to (h), but Using Two Point Flux Approximation

4.4 Case IV: Water Infiltration into a Heterogeneous and Anisotropic Dry Soil

For this section, Case III was modified to demonstrate the code's capability for simulating unsaturated flow in anisotropic and heterogeneous soil. The physical parameters, and boundary conditions are the same as those used in Case III, except that the vertical hydraulic conductivities ($\boldsymbol{K}_z$) in all the four zones were reduced by one order of magnitude. To compensate for the reduced hydraulic conductivity, the initial pressure was changed to -88.0 kPa. Three unstructured mesh meshes with resolutions of 0.1 m (mesh 1), 0.05 m (mesh 2) and 0.025 m (mesh 3) were used to analyze the effect of mesh resolution on the results accuracy. The number of nodes for the unstructured meshes are 6955, 27570 and 110847, respectively.

4.4.1 Transient Water Saturation at Observation Points

The changes of water saturation based on different gradient reconstruction methods for the two observation points are shown in Figure 4-9. Similar to Case II, the TPFA method cannot simulate results with acceptable accuracy compared to the MPFA method or the structured mesh. There are significant oscillations when using centered weighting for the MPFA method, as shown in Figure 4-9(a) and (e). However, no oscillations are visible for multi-point upstream weighting, as shown in Figure 4-9: (b) and (f). The oscillations using centered weighting can be improved by using meshes with higher resolution, as shown in Figure 4-9(c), (d), (g) and (h). For centered weighting using different control volume types, it can be seen that the VD control volume type generally leads to much smaller oscillations than CC and MD control volume types. Similar results were observed for the other gradient reconstruction methods.

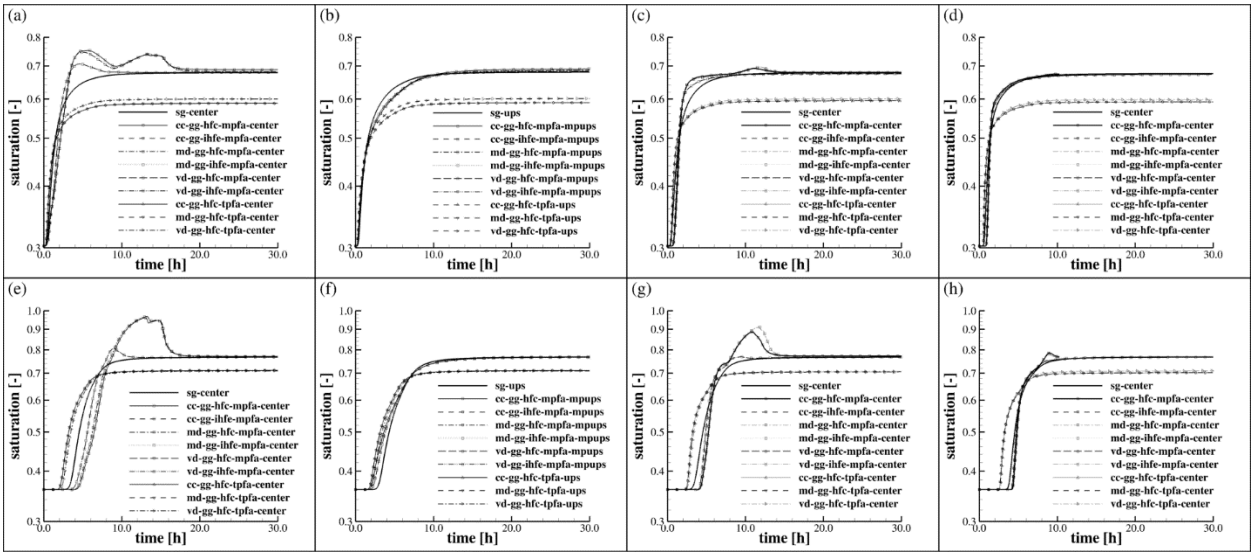

Figure 4-9: Transient Changes of Water Saturations at Observation Points P1 and P2 Obtained for Case IV Using Different Numerical Methods and Mesh Resolutions, (a) P1 Based on Centered Weighting Using Mesh 1, (b) P1 Based on Upstream Weighting Using Mesh 1, (c) P1 Based on Upstream Weighting Using Mesh 2, (d) P1 Based on Upstream Weighting Using Mesh 3, (e) P2 Based on Centered Weighting Using Mesh 1, (f) P2 Based on Upstream Weighting Using Mesh 1, (g) P2 Based on Upstream Weighting Using Mesh 2, and (h) P2 Based on Upstream Weighting Using Mesh 3

4.4.2 Spatial Distribution of Water Saturations

Corresponding to the transient changes of water saturations, the spatial distribution of water saturations after a period of 30 days is shown in Figure 4-10. Compared to the results obtained using the structured mesh, oscillations near the wetting front are obvious for centered weighting, especially for CC and MD control volume types, as shown in Figure 4-10 (c) and (e), and compared to the VD control volume type in Figure 4-10 (g). For multi-point upstream weighting, similar results are obtained using different control volume types, as shown in Figure 4-10 (d), (f) and (h). With the refinement in mesh resolution, the oscillation in the wetting front can be improved and more accurate results are obtained for both centered weighting and MPUPS weighting.

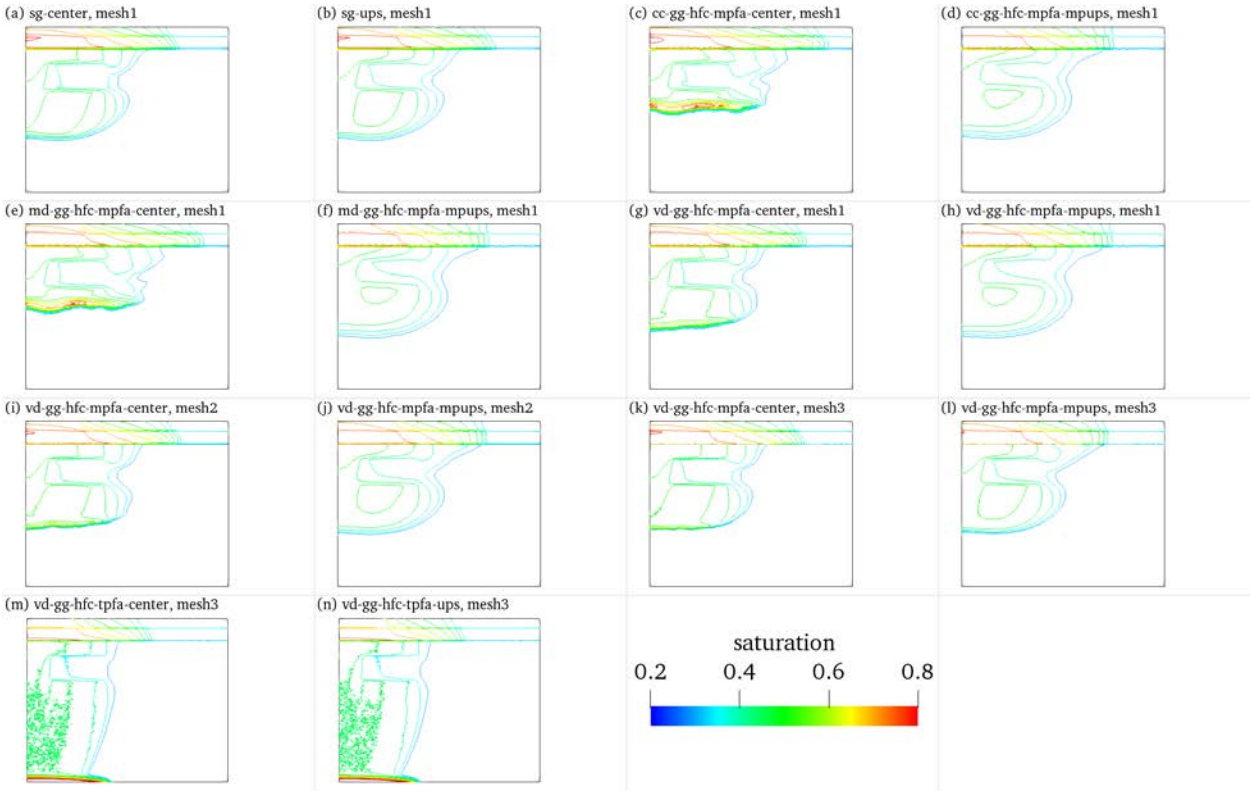

Figure 4-10: Contour Plots of Water Saturations After a Period of 30 Days for Case IV Using Different Numerical Schemes as Listed in Appendix 1, (a) and (b) Structured Mesh Using Centered Weighting and Upstream Weighting, (c) and (d) Unstructured Mesh with Cell-centered Control Volume Type Using Centered Weighting and Upstream Weighting, (e) and (f) Unstructured Mesh with Medial-dual Control Volume Type Using Centered Weighting and Upstream Weighting, (g) and (h) Unstructured Mesh with Voronoi-diagram Control Volume Type Using Centered Weighting and Upstream Weighting, (i) and (j) Same as (g) to (h) But Using Mesh 2, (k) and (l) Same as (g) to (h) But Using Mesh 3, (m) and (n) Unstructured Mesh with Voronoi-diagram Control Volume Type Using Two-point Flux Approximation

4.5 Monotonicity and Convergence Behavior

Both anisotropy and heterogeneity increase the complexity of the simulation case. Based on the numerical experiments of Case I to Case IV, we can conclude that, from the numerical point of view, the anisotropy plays a more important role than heterogeneity in causing oscillations and convergence problems. For simulations with isotropic conductivity tensors, despite of the heterogeneity in the system, the results are similar when different numerical methods, including different control volume types (CC, MD, VD), different gradient reconstruction methods (GG, LS, HLS2, HLS3, HLS3e, HLS4, HLS4e), different control volume interface center types (HFC, IHFE), different spatial weighting (Centered, UPS, MPUPS), and most importantly, different flux approximation methods (TPFA, MPFA) are used. However, in the simulations with anisotropic conductivity tensors, even though the system is homogeneous, these different methods have quite different effects on the quality of numerical results. In this section, the monotonicity and

convergence behavior are analyzed for simulations involving both isotropic and anisotropic material properties. Without loss of generality, the numerical experiments with homogeneous material properties (Case I and II) are used here.

4.5.1 Isotropic Material Properties

The monotonicity and convergence behavior of MPFA-GRM is analyzed for Case I based on the mesh with average nodal spacing 0.05 m. The maximum time step is 1.0 hour and the minimum time step is 1.0E-8 hour. The convergence tolerance for linear and nonlinear solvers are 1.0E-9 and 1.0E-6, respectively. For each gradient reconstruction method, 18 simulations using different control volume types, center of control volume interface and spatial weighting schemes were carried out. All simulations converged well, except those using fourth order HLS-GRM considering high order Taylor expansion remainder (HLS4e). The failure of HLS4e is attributed to the added nonlinearity, when more neighboring nodes are used together with methods using high order Taylor series expansion to estimate the gradient at the control volume interface. For the other gradient reconstruction methods with or without high order Taylor expansion, the convergence and mass balance error of different numerical scheme is shown in Figure 4-11. It is interesting to observe that the high order Taylor expansion remainder does not enhance the convergence. In contrast, the convergence properties deteriorate and more iterations and timesteps are required when the HFC method is used. The relative mass balance error considering higher order Taylor expansion is also significantly higher than the other methods. Simulations with centered weighting require more iterations and time steps than upstream weighting and MPUPS weighting. However, the relative mass balance errors remain similar. Comparing to CC and MD control volume types, the relative mass balance error based on VD control volume type is slightly smaller, on the expense of a few additional iterations and time steps.

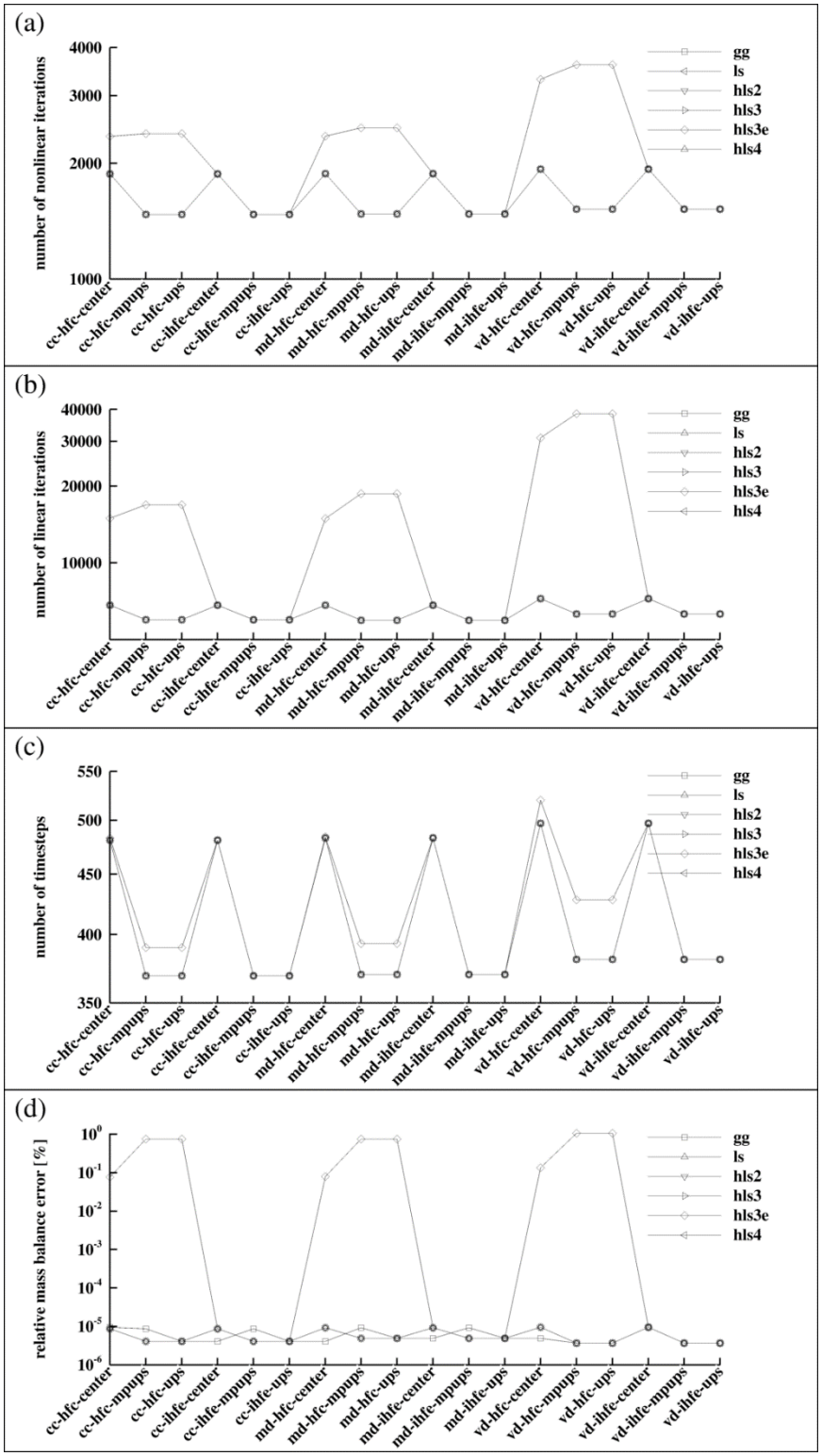

Figure 4-11: Convergence and Mass Balance Error of MPFA Methods for Variably Saturated Flow, Case I, Using Different Numerical Schemes, (a) Number of Nonlinear Iterations, (b) Number of Linear Iterations, (c) Number of Time Steps, and (d) Relative Mass Balance Error

4.5.2 Anisotropic Material Properties

Even though the TPFA method meets the positive transmissibility condition, we find that it is not sufficient to ensure the monotonicity for the solution of nonlinear unsaturated flow with anisotropic material properties. The code demonstrates that the standard two-point upstream weighting cannot guarantee monotonicity, showing difficulty in convergence. The convergence and mass balance error of different numerical schemes for anisotropic material properties are shown in Figure 4-12. All simulations using the fourth order HLS-GRM fail due to the lack of monotonicity. For GG, HLS3 and HLS3e methods, centered weighting requires more nonlinear iterations but less linear iterations than MPUPS weighting. However, for the HLS2 method, the MPUPS weighting requires more iterations than centered weighting in the nonlinear solver. For all gradient reconstruction methods, the MPUPS weighting takes fewer time steps than centered weighting. There is no significant difference between HFC and IHFE methods regarding number of linear iterations, nonlinear iterations and time steps. Regarding the relative mass balance error, the HLS3e method generates much larger errors than other gradient reconstruction methods when HFC method is used, indicating that the high order Taylor expansion does not work well with the HFC method. The relative mass balance error between HLS3 and HLS3e is almost identical with the IHFE method, implying that the the high order Taylor expansion does not reduce the numerical error in this case. In this case, it can be seen that the HLS2 method has the smallest mass balance error, especially in combination with the HFC method. The GG and LS methods show very close mass balance errors and the HLS3 method has a mass balance error between HLS2 and LS. We can also see that, compared to MD and CC control volume types, the VD control volume type is the most robust, as it requires fewer linear and nonlinear iterations.

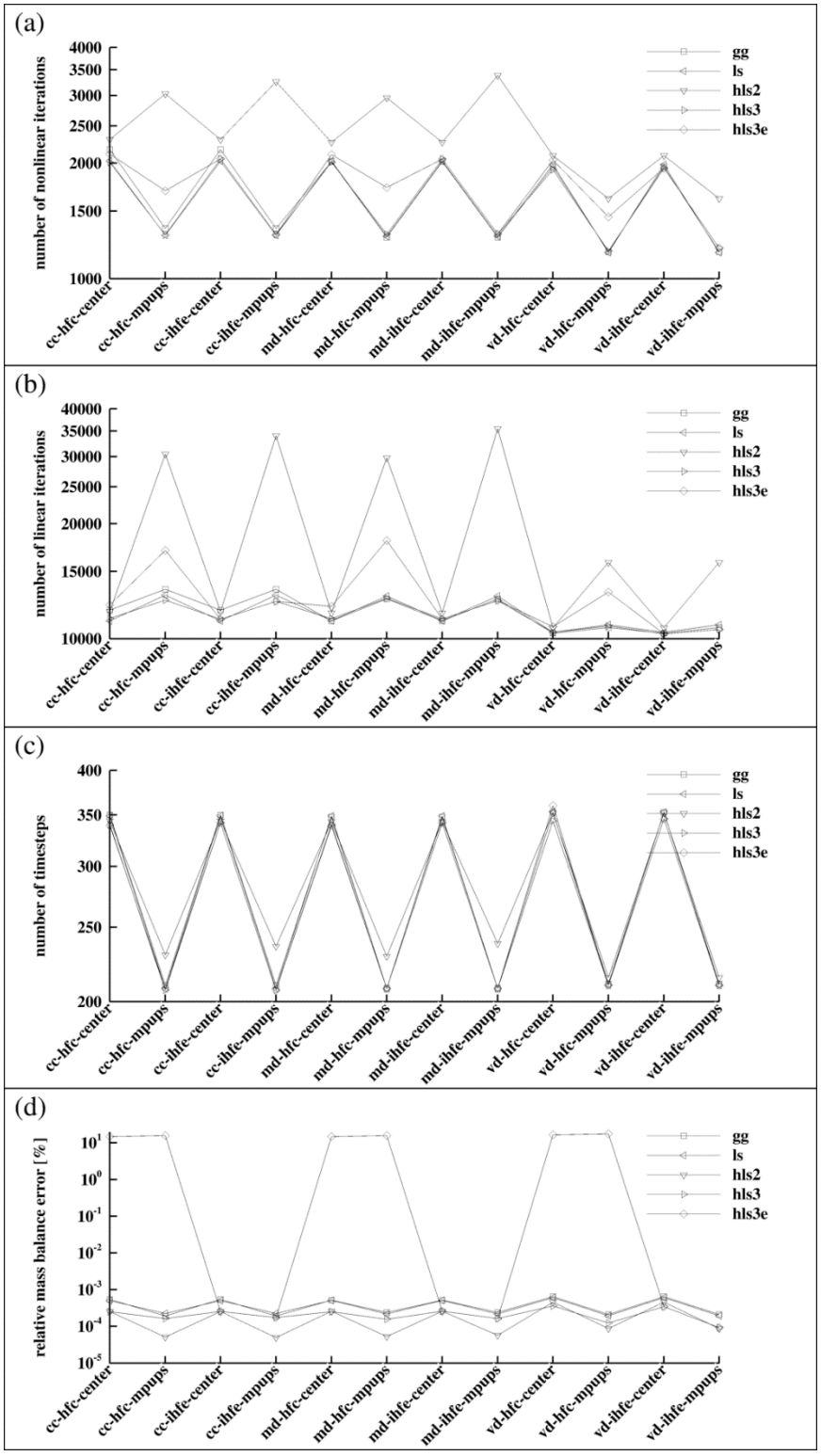

Figure 4-12: Convergence and Mass Balance Errors of MPFA Methods for Variably Saturated Flow, Case II Using Different Numerical Schemes, (a) Number of Nonlinear Iterations, (b) Number of Linear Iterations, (c) Number of Time Steps, and (d) Relative Mass Balance Error

5. Verification of MIN3P-THCm V2.0 and Demonstration Examples

The structured grid version of MIN3P-THCm has been verified against many other reactive transport codes (Carrayrou et al. 2010, Marty et al. 2015, Perko et al. 2015, Şengör et al. 2015). MIN3P-THCm V1.1 has also been verified by comparing the results to those of the sequential version for a wide range of verification problems (Su et al. 2017). Verification of MIN3P-THCm V2.0 was carried out by comparing the results to analytical solutions, structured grid solutions obtained with MIN3P-THCm and MIN3P-THCm V1.1, and another reactive transport code, namely PFLOTRAN (Lichtner et al. 2018a, 2018b).

Based on the analysis of the MPFA method for variably saturated flow, we found that for numerical experiments with isotropic conductivity tensors, results are similar for different numerical methods. However, these different methods can have quite different effects on the accuracy of the results and efficiency of the simulations in the case of anisotropic conductivity tensors. It was shown that the VD control volume type has the best accuracy and can avoid non-physical oscillations for meshes with different resolutions. In the following analysis, if not specified, the VD control volume type is used for the simulations, together with control volume interface centers determined by the IHFE method, GG gradient reconstruction, MPFA flux approximation and MPUPS weighting.

5.1 Verification against Analytical Solutions

5.1.1 Case V: Solute Transport in 2D

The first case is based on the migration of chloride in a 2D vertical corss-section simulating in the migration of landfill leachate through a narrow, relatively thin, valley-fill aquifer (Wexler 1992). The solute source is at the inflow boundary on the left side of the simulation domain. Physical parameters are summarized as in Table 5-1.

Table 5-1: Physical Parameters for 2D Solute Transport Problem

Parameter	Symbol	Value	Unit
Aquifer width	W	1.37×10^{3}	m
Aquifer height	H	9.14×10^{3}	m
Aquifer porosity	ϕ	2.50×10^{-1}	-
Groundwater velocity	V_x	3.05×10^{-1}	m d^{-1}
Longitudial dispersivity	α_l	6.10×10^{1}	m
Transverse dispersivity[1]	α_t	0.0	m
Molecular diffusion coefficient[2]	D_0	1.25×10^{-4}	m^2 s^{-1}
Source concentration	C_0	1.0	g L^{-1}
Lower limit of source	Z_1	1.22×10^{2}	m
Upper limit of source	Z_2	6.10×10^{2}	m

[1] Not available in PFLOTRAN

[2] Coefficient is upscaled to account for the effect of transverse dispersivity

It should be noted that transverse dispersivity is not supported by PFLOTRAN. An increased molecular diffusion coefficient is used to account for transverse dispersivity effect. The analytical

solution is based on the algorithm provided in the literature (Wexler 1992). A structured grid and an unstructured triangular mesh are used for both MIN3P-THCm V2.0 and PFLORTRAN, as shown in Figure 5-1.

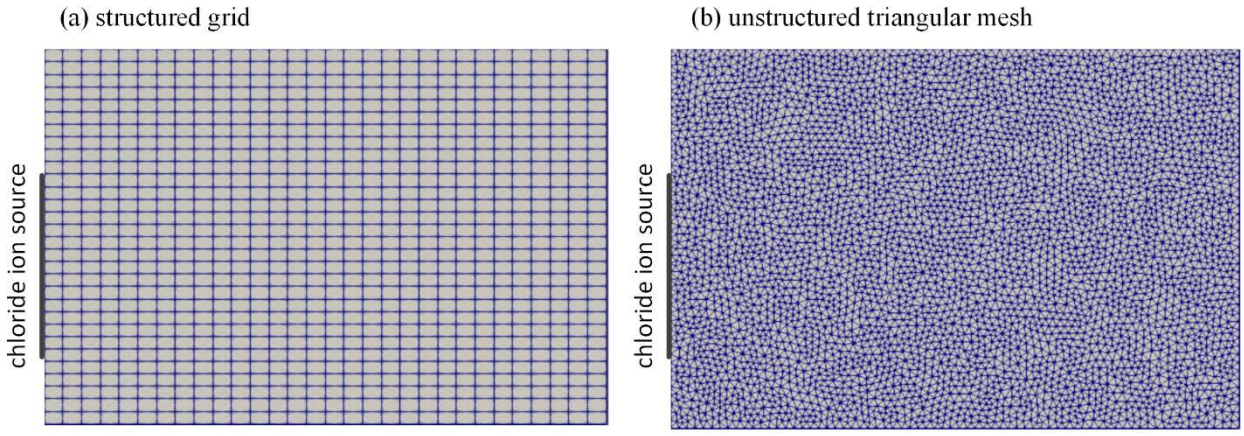

Figure 5-1: Mesh for 2D Simulation of Chloride Migration Through an Aquifer, (a) Structured Grid, and (b) Unstructured Triangular Mesh

With the analytical solution, concentrations are calculated for nodal locations of the structured grid, as shown in Figure 5-1 (a). The normalized concentration C/C_0 distributions after 1500 and 3000 days are simulated, as shown in Figure 5-2. Results from MIN3P-THCm V2.0 and PFLOTRAN both fit well with the analytical solution. Small differences in source concentrations on the left boundary are caused by the different numerical schemes between MIN3P-THCm V2.0 and PFLOTRAN, as MIN3P-THCm V2.0 uses a vertex-centered discretization, while PFLOTRAN uses cell-centered discretization. Using the same mesh, there is a small shift when applying the boundary condition, as the values are stored at the nodes for the vertex-centered scheme, but at the cell center for cell-centered scheme. Compared to the analytical solution and the solution based on the structured grid, the solutions obtained using the unstructured grid show a small degree of numerical dispersion for both MIN3P-THCm V2.0 and PFLOTRAN, which cannot be avoided unless the mesh is fully orthogonal. This numerical error is generally observed in cases with strict one-dimensional velocity but without transverse dispersion. For cases with a non-uniform velocity distribution, or with both transverse and longitudinal dispersion, this error is less visible and is equally present in structured grid simulations.

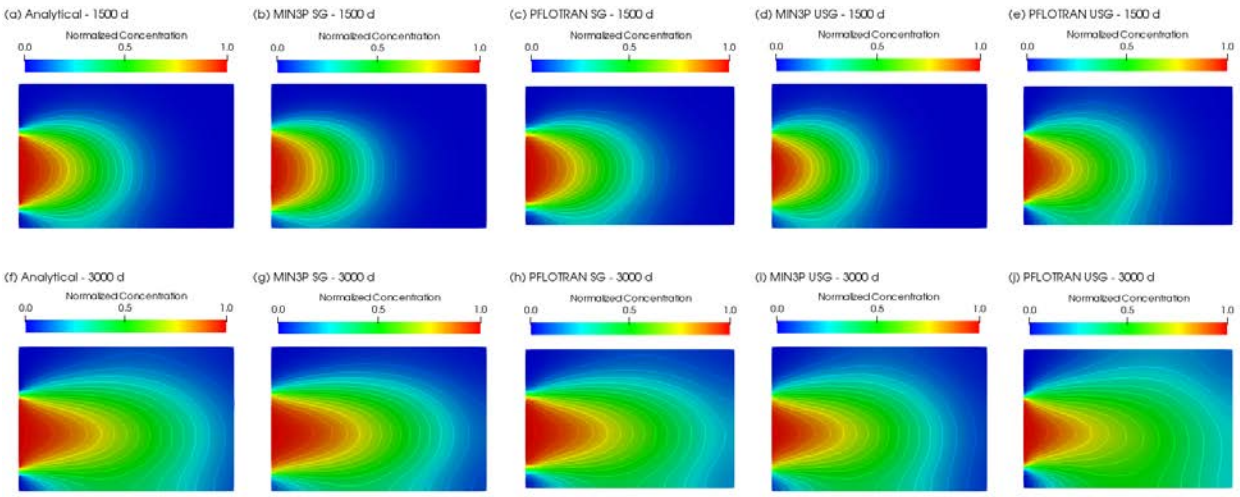

Figure 5-2: Comparison of Normalized Concentrations After 1500 Days and 3000 Days for Case V, SG Stands for Structured Grid, USG Stands for Unstructured Grid, (a) and (f) Analytical Solution, (b) and (g) MIN3P Structured Grid Solution, (c) and (h) PFLOTRAN Structured Grid Solution, (d) and (i) MIN3P Unstructured Grid Solution, (e) and (j) PFLOTRAN Unstructured Grid Solution

5.1.2 Case VI: Solute Transport in 3D

A 3D solute transport case, for which an analytical solution is available, is considered.The test case is based on 3D-migration of chloride from a landfill, created by filling in a gravel pit excavated in a valley-fill aquifer (Wexler 1992). The solute source is at the inflow boundary on the left side of the simulation domain. Physical parameters are summarized in Table 5-2.

Table 5-2: Physical Parameters for 3D Solute Transport Problem

Parameter	Symbol	Value	Unit
Aquifer length	L	1.37×10^{3}	m
Aquifer width	W	9.14×10^{2}	m
Aquifer height	H	3.05×10^{2}	m
Aquifer porosity	ϕ	2.50×10^{-1}	-
Groundwater velocity	V_x	3.05×10^{-1}	m d^{-1}
Longitudial dispersivity	α_l	6.10×10^{1}	m
Transverse dispersivity[1]	α_t	0.0	m
Molecular diffusion coefficient[2]	D_0	1.25×10^{-4}	m^2 s^{-1}
Source concentration	C_0	1.0	g L^{-1}
Y-coordinate of lower limit of source	Y_1	1.07×10^{2}	m
Y-coordinate of upper limit of source	Y_2	6.25×10^{2}	m
Z-coordinate of lower limit of source	Z_1	1.37×10^{2}	m
Z-coordinate of upper limit of source	Z_2	2.59×10^{2}	m

[1] Not available in PFLOTRAN

[2] Coefficient is upscaled to account for the effect of transverse dispersivity

As for the 2D case, molecular diffusion is added to account for the effect of transverse dispersion, via an upscaled diffusion coefficient. The analytical solution is provided in the literature (Wexler 1992). A structured grid mesh, an unstructured mesh consisting of prisms and an unstructured mesh consisting of tetrahedra are used for both MIN3P-THCm V2.0 and PFLOTRAN, as shown in Figure 5-3.

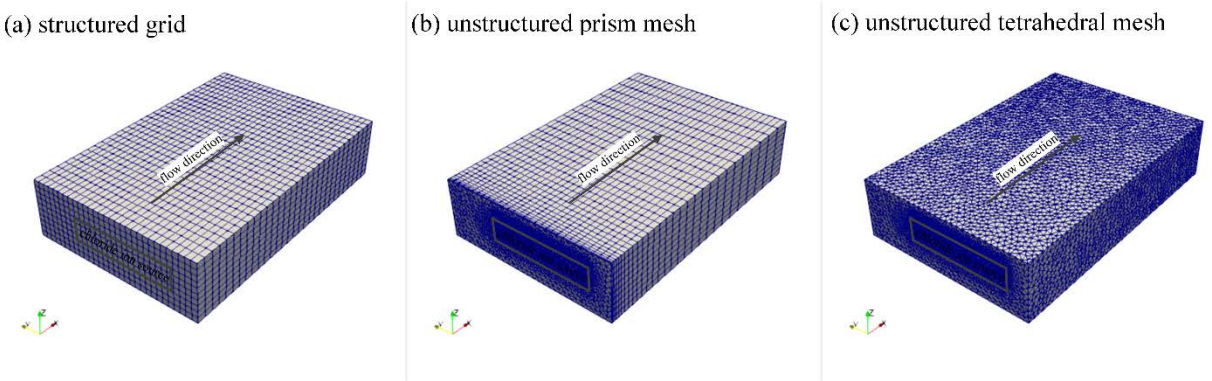

Figure 5-3: Mesh for 3D Chloride Transport Through an Aquifer, (a) Structured Grid, (b) Unstructured Prism Mesh, and (c) Unstructured Tetrahedral Mesh

Concentrations from the analytical solution are calculated for locations defined by the structured grid in Figure 5-3(a). The normalized concentration C/C_0 distribution after 1500 and 3000 days

is shown in Figure 5-4. The results from MIN3P-THCm V2.0 and PFLOTRAN both agree well with the analytical solution. There are small differences in the source concentrations on the left boundary that are caused by the different numerical schemes of MIN3P-THCm V2.0 and PFLOTRAN, similar to the 2D case. PFLOTRAN uses a cell-centered scheme where the unknowns (here chloride concentrations) are set at the cell center, while MIN3P-THCm V2.0 uses a vertex-centered scheme, where the unknowns are set at the vertices. Compared to the solutions obtained analytically and with the structured grid method, the unstructured grid solutions obtained with both MIN3P-THCm V2.0 and PFLOTRAN show a low level of numerical dispersion, which, as for the 2D case, cannot be avoided unless the mesh is fully orthogonal. The tetrahedral mesh produces more significant dispersion than the structured grid or prism mesh, which implies that the mesh quality of the orthogonal and prism meshes are better than the discretization based on tetrahedral cells. Nevertheless, MIN3P-THCm V2.0 using the tetrahedral mesh still generates smooth results of acceptable accuracy.

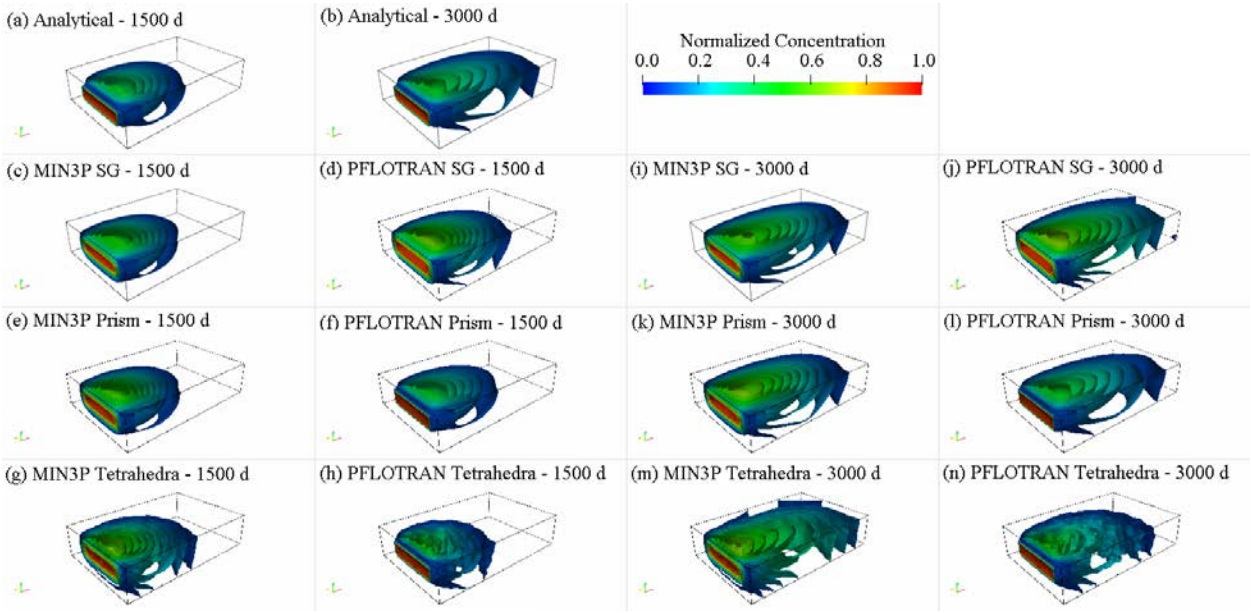

Figure 5-4: Comparison of Normalized Concentrations After 1500 Days and 3000 Days for Case VI, SG Stands for Structured Grid, Prism Stands for Prism Mesh and Tetrahedra Stands for Tetrahedral Mesh, (a) and (b) Analytical Solutions After 1500 Days and 3000 Days, (c) to (h) MIN3P-THCm V2.0 and PFLOTRAN Solutions for Different Meshes After 1500 Days, (i) to (n) MIN3P-THCm V2.0 and PFLOTRAN Solutions for Different Meshes After 3000 Days

5.2 Verification against Structured Grid Solutions

Considering that analytical solutions for reactive transport problems with heterogeneous material properties, complex reactions and/or density dependent flow do not exist, an alternative option for verification is comparison of results obtained from the unstructured grid implementation to those obtained from the structured grid version. For this purpose, a density dependent flow problem is selected to evaluate accuracy of the code. In this context, it is worth mentioning that density dependent flow and transport is very sensitive to the simulation mesh, thus proving a suitable test for the unstructured grid implementation.

5.2.1 Case VII: Density Dependent Flow in 2D Space

The density dependent flow and transport problem presented here is the Elder problem, a well known 2D fluid convection problem affected by solute concentration gradients (Souza and Voss 1987, Simmons and Elder 2017). The Elder problem domain consists of a cross-section containing a zone of freshwater underlying a source of brine. A concentration of 0 g/L was assigned to the lower part of the domain and the concentration was set to C_s at the upper boundary. No flow boundaries were assigned to all four sides of the domain. A constant fluid pressure of 0 Pa was assigned to the upper left corner of the domain. The physical input parameters are specified as shown in Table 5-3.

Table 5-3: Physical Parameters for 2D Density Dependent Flow and Transport Problem

Parameter	Symbol	Value	Unit
Domain width	W	3.00×10^{2}	m
Domain height	H	1.50×10^{2}	m
Porosity	ϕ	1.00×10^{-1}	-
Hydraulic conductivity	K	4.75×10^{-6}	m s^{-1}
Dispersivity	$\alpha_l = \alpha_t$	0.0	m
Molecular diffusion coefficient	D_0	0.0	m^2 s^{-1}
Saltwater density	ρ_s	1.20×10^{3}	kg m^{-3}
Freshwater density	ρ_0	1.00×10^{3}	kg m^{-3}
Maximum density ratio	ρ_{max}	1.20	-
Coefficient of density variation	$\frac{\partial \rho}{\partial c}$	7.00×10^{-1}	-
Saltwater concentration	C_s	2.86×10^{2}	g L^{-1}
X-coordinate of left limit of source	X_1	1.50×10^{2}	m
X-coordinate of right limit of source	X_2	3.00×10^{2}	m

Three meshes were considered in this verification problem. A structured grid, an unstructured mesh triangulated from the structured grid and a general, unstructured triangular mesh, as shown in Figure 5-5. The structured and triangulated structured grids (Figure 5-5 a and b) contain 8192 nodes and the unstructured grid (Figure 5-5 c) contains 7390 nodes.

Velocity and concentration distributions indicate that the results obtained with the unstructured grid method compare well with those from the structured grids. Although this problem is very sensitive towards mesh quality and other possible stable solutions have been obtained (Simmons and Elder 2017), the various unstructured grid implementations are able to reproduce the dimensions and temporal evolution of the convection cells in a consistent fashion.

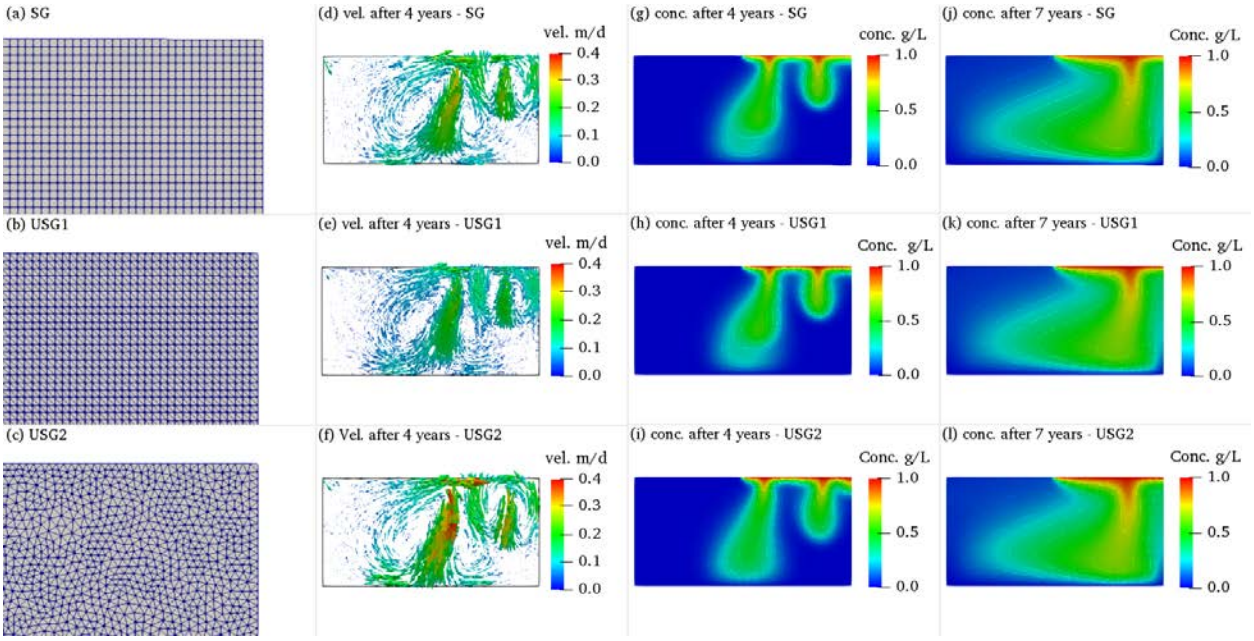

Figure 5-5: Grids and Results for the Elder Problem, (a) Structured Grid - SG (Top Right Part), (b) Triangulated Structured Grid - USG1 (Top Right Part), (c) Unstructured Grid - USG2 (Top Right Part), (d) to (f) Velocity Distributions After 4 Years, (g) to (i) Concentration Distributions After 4 Years, (j) to (l) Concentration Distributions After 7 Years

5.2.2 Case VIII: Reactive Transport in Heterogeneous Porous Media

This case focuses on calcite dissolution in a fully saturated heterogeneous porous medium. The simulation domain contains two materials with different hydraulic conductivites, porosities and dispersivities. The components H^+, CO_3^{2-} and Ca^{2+}, the secondary species OH^-, HCO_3^- and H_2CO_3(aq), and the mineral calcite are included in the geochemical system. Two fixed hydraulic heads were specified at the bottom left boundary and at the top right boundary. An acidic solution with elevated concentrations of carbonic acid was specified at the inflow boundary, reacting with the mineral calcite ($CaCO_3$). Reaction products then exit at the top right boundary, as shown in Figure 5-6 (a) and (b). Physical and chemical input parameters are given in Table 5-4. Four different mesh sizes were used for both structured and unstructured grids. The average cell/edge size for the four meshes were 0.01 m, 0.005 m, 0.0025 m and 0.00125 m. For the structured grid, the total number of nodes was 561, 2145, 8385 and 33153, respectively and for the unstructured grid, the total number of nodes was 666, 2499, 9448 and 37129.

The simulation was carried out for a period of 100 days. The calcite volume fractions after 100 days are shown in Figure 5-6 (c) to (j). The dissolution front of calcite advances fast in the zone with higher hydraulic conductivity, leading to sharp gradients when it reaches the zone with lower hydraulic conductivity. At the interface of these two zones, the dissolution front can advance differently depending on the cell size. The simulation results indicate that the structured grid implementation requires a fine mesh with a cell size no larger than 0.0025 m to produce accurate results, while a mesh resolution of 0.005 m is sufficient for the unstructured grid solution. This corresponds to a total number of 8385 nodes for the structured grid and 2499 nodes for the unstructured grid. The structured grid is not able to capture the spatial distribution of hydraulic conductivities adequately and cannot produce an accurate solution without a high mesh resolution. Compared to the structured grid, the unstructured grid can represent the

irregular distribution of hydraulic conductivities much better and does not require a highly refined mesh to obtain accurate results. The simulated results illustrate that geochemical reactions tend to occur at interfaces of adjacent materials with varying properties, implying that gradients controlling fluid and solute exchange are often large near the interfaces, requiring refined spatial discretization in these regions.

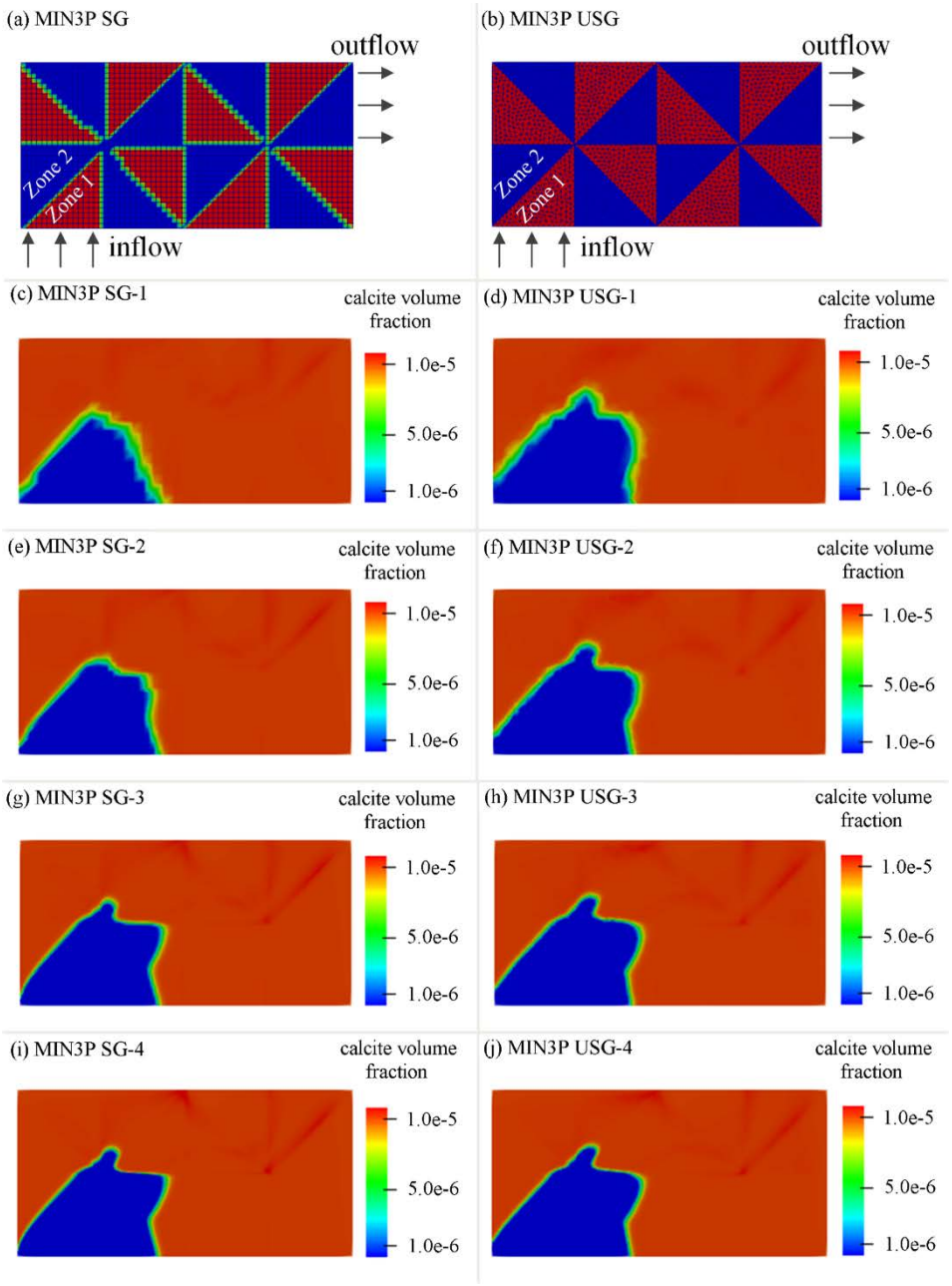

Figure 5-6: 2D Reactive Transport in a Heterogeneous Porous Medium, (a) Structured Grid, (b) Unstructured Grid, (c), (e), (g), (i) Calcite Volume Fractions After 100 Days with Average Cell Size Ranging from 0.01 m to 0.00125 m for the Structured Grid, and (d), (f), (h), (j) Calcite Volume Fractions After 100 Days with Average Cell Size Ranging from 0.01 m to 0.00125 m for the Unstructured Grid

Table 5-4: 2D Reactive Transport Problem in a Heterogeneous Porous Medium - Physical and Chemical Parameters

Parameter	Symbol	Value	Unit
Domain width	W	3.20×10^{-1}	m
Domain height	H	1.60×10^{-1}	m
Porosity in Zone 1	ϕ_1	3.50×10^{-1}	-
Porosity in Zone 2	ϕ_2	1.50×10^{-1}	-
Hydraulic conductivity in Zone 1	K_1	1.16×10^{-5}	m s^{-1}
Hydraulic conductivity in Zone 2	K_2	1.16×10^{-6}	m s^{-1}
Dispersivity in Zone 1	$\alpha_{l1} = 40\alpha_{t1}$	5.00×10^{-4}	m
Dispersivity in Zone 2	$\alpha_{l2} = 40\alpha_{t2}$	5.00×10^{-3}	m
Molecular diffusion coefficient	D_0	0.0	m^2 s^{-1}
Hydraulic head at inflow boundary	h_{in}	1.40×10^{-3}	m
Hydraulic head at outflow boundary	h_{out}	0.0	m
Initial calcite volume fraction	ϕ_m	1.00×10^{-5}	-
Initial total concentration of H^+	T_{H^+}	2.00×10^{-7}	mol L^{-1}
Initial total concentration of CO_3^{2-}	$T_{CO3^{2-}}$	1.00×10^{-7}	mol L^{-1}
Initial total concentration of Ca^{2+}	$T_{Ca^{2+}}$	1.00×10^{-8}	mol L^{-1}
Boundary total concentration of H^+	T_{H^+}	2.00×10^{-4}	mol L^{-1}
Boundary total concentration of CO_3^{2-}	$T_{CO3^{2-}}$	1.00×10^{-4}	mol L^{-1}
Boundary total concentration of Ca^{2+}	$T_{Ca^{2+}}$	1.00×10^{-8}	mol L^{-1}

5.3 Demonstration of Reactive Transport in a Complex Domain

5.3.1 Case IX: Reactive Transport in 2D Space

This demonstration case focuses on calcite dissolution through a variably saturated porous medium with heterogeneous and anisotropic hydraulic conductivities, as shown in Figure 5-7(a). The flow is considered steady in this case. The simulation domain contains three materials with different hydraulic conductivities, porosities and dispersivities. The top and bottom boundaries are assumed to be zero flux. Fixed hydraulic heads were specified at the left and right boundaries. As for the first demonstration example, a solution rich in carbonic acid enters the solution domain across the inflow boundary, reacts with the mineral calcite and reaction products exit across the right boundary. The physical and chemical input parameters are given in Table 5-5.

The simulation was carried out for a period of 500 days. As shown in Figure 5-7, flow and reactive transport in the simulation domain occur in three distinct regions, including 1) slow flow and transport through the low permeability Zone 1, 2) fast flow and transport through the high permeability Zone 2 and 3) diffusion-dominated transport in the very low permeability Zone 3. The results for water saturation, flow velocity, calcite volume fractions and pH after 100 days, 200 days and 500 days are shown in Figure 5-7 (b) to (j). The dissolution front of calcite advances quickly through Zone 2, but is inhibited by limited access to Zones 1 and 3, leaving behind an extensive region containing residual calcite. The pH value in the simulation domain

changes as calcite dissolves and becomes depleted. The unsaturated zone above the water table is not exposed to the acidic solution; calcite remains present throughout the simulation and pH remains elevated. The simulation demonstrates the versatility of the code to simulate flow and reactive transport in a complex domain with irregular boundaries and heterogeneous and anisotropic material properties.

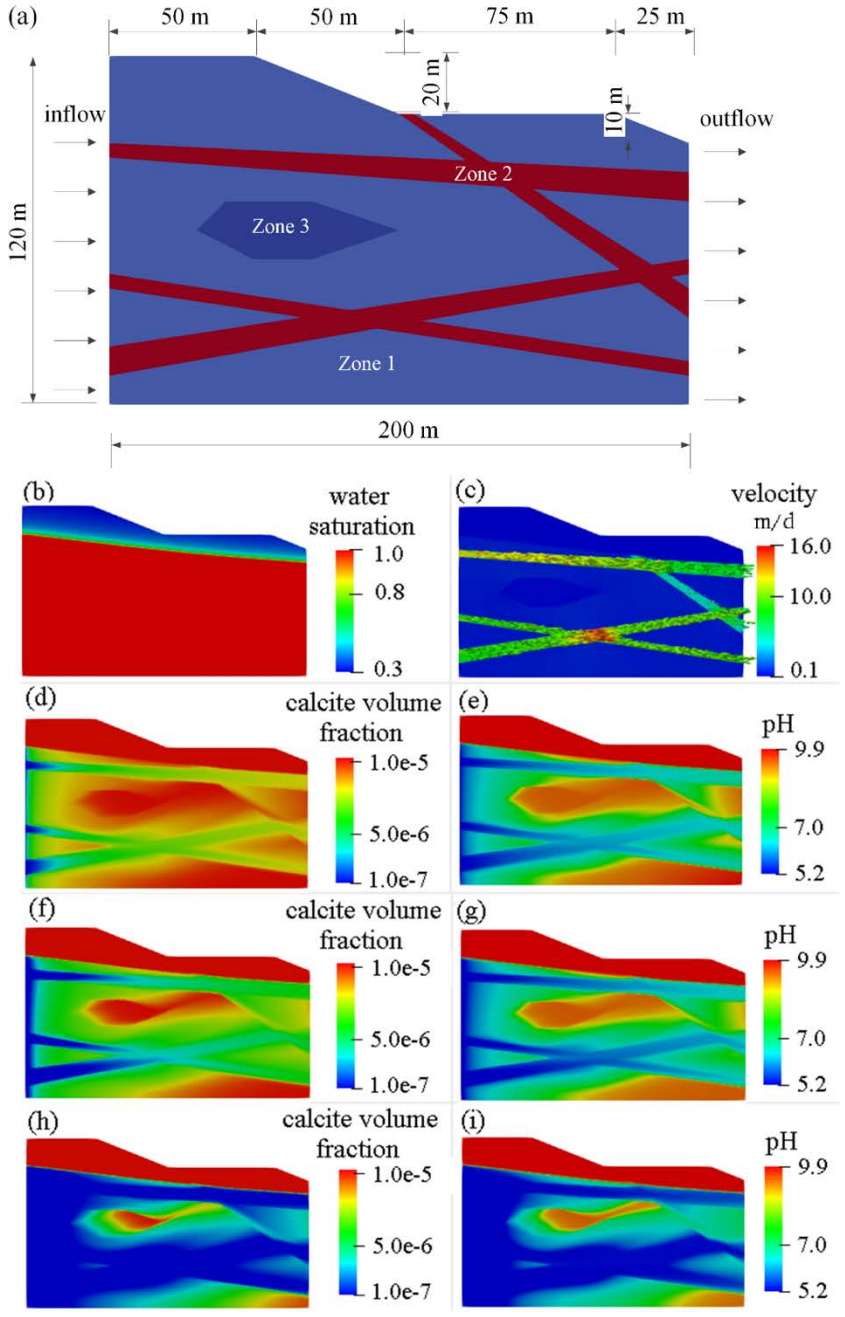

Figure 5-7: 2D Reactive Transport in a Complex Domain, (a) Simulation Domain and Boundary Conditions, (b) Water Saturation, (c) Flow Velocity [m day^{-1}], (d), (f), (h) Calcite Volume Fractions After 100 Days, 200 Days and 500 Days, and (e), (g), (i) pH After 100 Days, 200 Days and 500 Days

Table 5-5: 2D Reactive Transport in a Complex Domain - Physical and Chemical Parameters

Parameter	Symbol	Value	Unit
Domain width	W	2.00×10^{2}	m
Domain height	H	1.20×10^{2}	m
Porosity in Zone 1	ϕ_1	2.00×10^{-1}	-
Porosity in Zone 2	ϕ_2	5.00×10^{-1}	-
Porosity in Zone 3	ϕ_3	5.00×10^{-2}	-
Hydraulic conductivity in Zone 1	$K_{xx1} = K_{zz1}$	5.80×10^{-5}	m s^{-1}
Hydraulic conductivity in Zone 2	$K_{xx2} = 2K_{zz2}$	1.16×10^{-3}	m s^{-1}
Hydraulic conductivity in Zone 3	$K_{xx2} = 10K_{zz3}$	1.16×10^{-5}	m s^{-1}
Residual water saturation	S_r	2.80×10^{-1}	-
van Genuchten parameter α	α	2.58	m^{-1}
van Genuchten parameter n	n	1.47	-
pore connectivity parameter l	l	5.00×10^{-1}	-
Dispersivity in Zone 1	$\alpha_{l1} = 10\alpha_{t1}$	5.00×10^{-5}	m
Dispersivity in Zone 2	$\alpha_{l2} = 2\alpha_{t2}$	5.00×10^{-4}	m
Dispersivity in Zone 3	$\alpha_{l3} = 10\alpha_{t3}$	5.00×10^{-6}	m
Molecular diffusion coefficient	D_0	1.00×10^{-9}	m^2 s^{-1}
Hydraulic head at inflow boundary	h_{in}	1.00×10^{2}	m
Hydraulic head at outflow boundary	h_{out}	8.00×10^{1}	m
Initial calcite volume fraction	ϕ_m	1.00×10^{-5}	-
Initial total concentration of H^+	T_{H^+}	2.00×10^{-7}	mol L^{-1}
Initial total concentration of CO_3^{2-}	$T_{CO3^{2-}}$	1.00×10^{-7}	mol L^{-1}
Initial total concentration of Ca^{2+}	$T_{Ca^{2+}}$	1.00×10^{-8}	mol L^{-1}
Boundary total concentration of H^+	T_{H^+}	2.00×10^{-4}	mol L^{-1}
Boundary total concentration of CO_3^{2-}	$T_{CO3^{2-}}$	1.00×10^{-4}	mol L^{-1}
Boundary total concentration of Ca^{2+}	$T_{Ca^{2+}}$	1.00×10^{-8}	mol L^{-1}

6. Parallel Performance of MIN3P-THCm V2.0

A parallel performance test was carried out on Compute Canada's Cedar cluster (www.computecanada.ca) and on the Orcinus cluster managed by WestGrid (www.westgrid.ca). As shown in Table 6-1: , seven scenarios have been tested, which includes both solute transport and reactive transport test cases in 2D and 3D. The 2D solute transport test cases include simulations using a coarse mesh (trans-2d-a), a fine mesh (trans-2d-b), and a highly refined mesh (trans-2d-c). The 3D solute transport test cases include simulations using a coarse mesh (trans-3d-a) and a fine mesh (trans-3d-b). The reactive transport test cases include 2D simulations using a fine mesh (reactran-2d) and 3D simulation using a fine mesh (reactran-3d). For solute transport test cases, the initial and boundary conditions are the same as those shown in Table 6-1: , except that the 2D solute transport test cases use a Z-plane domain cutting through the source center ($Z = 198.12$ m). The reactive transport cases use the same domain as the solute transport cases; however, the initial and boundary conditions of components are changed to those listed in Table 6-1. The total degrees of freedom (tdof) of the 2D solute transport problem ranges from 4,250 for the coarse mesh to 33,601 for the highly refined mesh, and tdof of 3D solute transport problem ranges from 49,321 for the coarse mesh to 664,671 for the fine mesh. The tdof of reactive transport problem is 43,395 for the 2D problem and 1,994,013 for the 3D problem, respectively. All scenarios have been tested using the MPI and OpenMP versions. Scenarios trans-2d-b, trans-2d-c and reactran-2d have also been tested for the hybrid MPI-OpenMP version. The parallel performance of the structured grid version has been comprehensively analyzed in a previous study (Su et al. 2017). In this report, the parallel performance analysis focused on the total runtime, without correcting for input and output times. For the OpenMP version, the performance has been tested for up to 32 processors for the 2D case and 48 processors for the 3D case. For the MPI version, the performance has been tested for up to 32 processors for the 2D case and 192 processors for the 3D case. The hybrid version was tested for up to 192 processors.

Table 6-1: Parallel Performance Test Scenarios

scenario	mesh	nodes	dof	tdof	OpenMP	MPI	hybrid
trans-2d-a	triangle	4,250	1	4,250	yes	yes	no
trans-2d-b	triangle	14,465	1	14,465	yes	yes	yes
trans-2d-c	triangle	33,601	1	33,601	yes	yes	yes
trans-3d-a	prism	49,321	1	49,321	yes	yes	no
trans-3d-b	prism	664,671	1	664,671	yes	yes	no
reactran-2d	triangle	14,465	3	43,395	yes	yes	yes
reactran-3d	prism	664,671	3	1,994,013	yes	yes	no

6.1 Parallel Performance for Solute Transport Case

The total runtime and speedup related to the number of processors (nprocs) are shown in Figure 6-1. Both OpenMP and MPI versions show significant runtime decreases and speedup increases as the number of processors increases. Generally, the performance of the OpenMP version is better than that of the MPI version when tdof is small, as shown in Figure 6-1 (a), (b) and (c). This is mainly due to the communication overhead in the MPI parallelization for cases with small tdof. As the tdof increases, the MPI parallelization provides better performance than

the OpenMP version. As shown in Figure 6-1 (d), the total runtime for the MPI version is generally less than that of the OpenMP version. This is caused by the overhead incurred in creating the threads for the OpenMP version. For the small simulation case, the communication overhead for the MPI version is significant compared to the overhead of creating threads for the OpenMP version. For the large simulation case, the overhead of the OpenMP version can be more substantial than that for the MPI version. It can also be observed that the OpenMP version can gain super-linear speedup by taking advantage of better usage of cache of the CPU, as shown in Figure 6-1 (c) and (d). Super-linear speedup depends on the cache size of the CPU, total memory required for the case, memory used by each thread and OpenMP overhead. Super-linear speedup only occurs when memory used by each thread just fits the cache size and OpenMP overhead is not significant. For both MPI and OpenMP versions, it can be estimated from Figure 6-1: that parallel performance yields near linear speedup when tdof per processor is larger than 2000.

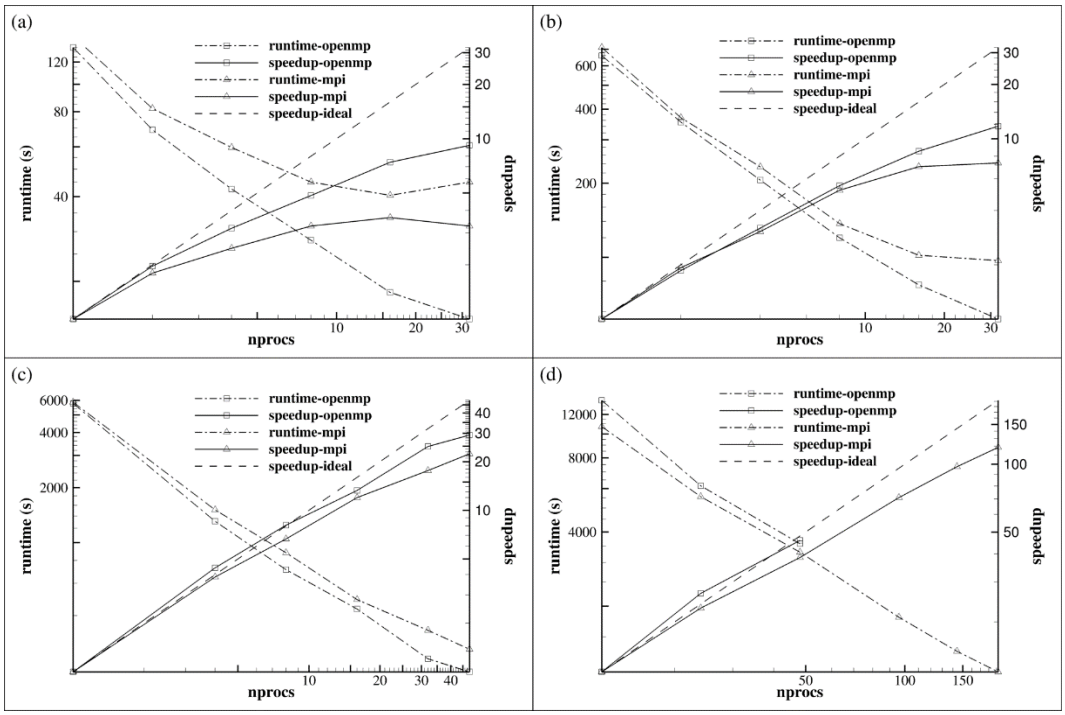

Figure 6-1: Parallel Runtime and Speedup, (a) 2D Solute Transport with Original Mesh, (b) 2D Solute Transport with Refined Mesh, (c) 3D Solute Transport with Original Mesh, and (d) 3D Solute Transport with Refined Mesh

6.2 Parallel Performance for Reactive Transport Case

To test the performance for reactive transport simulations, the 2D and 3D solute transport cases were modified by including calcite precipitation/dissolution reactions and aqueous complexation of calcium and carbonate species. The performance for reactive transport simulations is shown in Figure 6-2. Compared to the solute transport simulations, reactive transport simulations add additional computational burden to the system caused by local geochemical reactions and their coupling to the transport equations. Since this extra burden does not require additional communication cost, it does not negatively affect the parallel performance. However, this extra burden may change cache efficiency, depending on the problem size. As shown in Figure 6-2

(a) and (b), for a 2D reactive transport simulation that does not require large memory, the simulation is "cache-friendly" and produces better performance than the solute transport simulation. For large 3D reactive transport simulations, in which the memory demand is far more than the cache size, the parallel performance declines relative to the solute transport simulation with the same grid resolution, as shown in Figure 6-2 (c) and (d). Comparing Figure 6-2 (a) to (b) and (c) to (d), we can also observe that the OpenMP parallel version generally provides better speedup than the MPI parallel version.

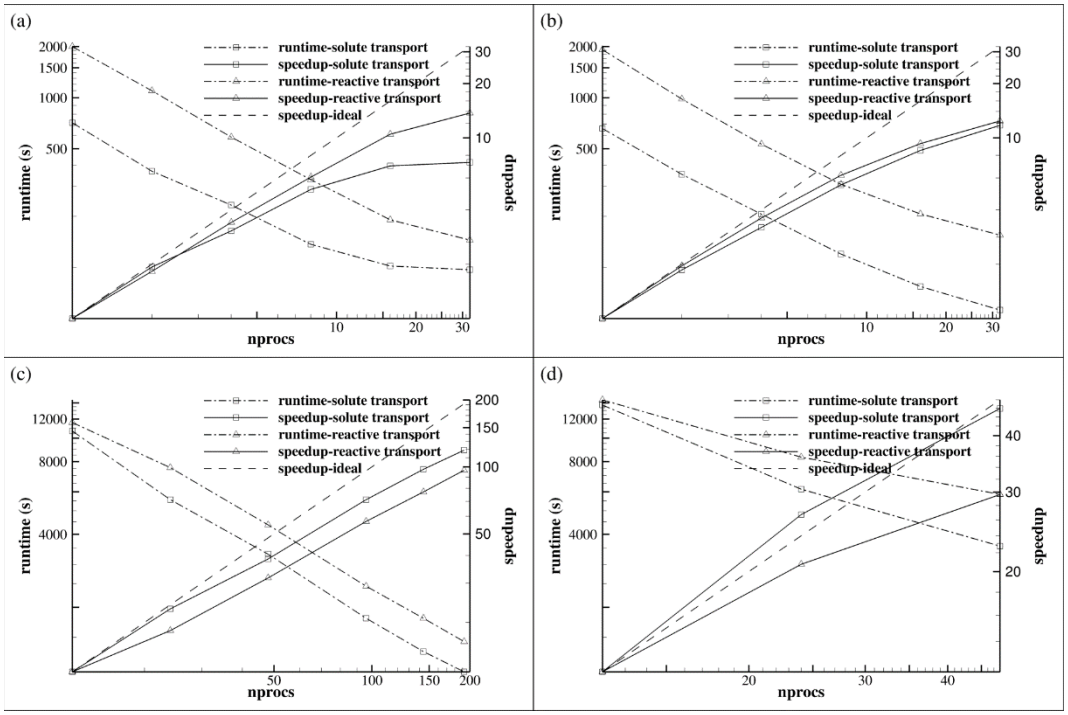

Figure 6-2: Parallel Runtime and Speedup for Solute Transport and Reactive Transport, (a) 2D Case Using MPI Parallel Version, (b) 2D Case Using OpenMP Parallel Version, (c) 3D Case Using MPI Parallel Version and (d) 3D Case Using OpenMP Parallel Version

6.3 Parallel Performance of Hybrid MPI-OpenMP Version

Both MPI parallelization and OpenMP parallelization have their own advantages and limitations. In the MIN3P-THCm V2.0 code, a hybrid MPI-OpenMP parallelization is implemented by taking advantage of both parallelization methods. For evaluating the parallel performance of the hybrid version, three cases were selected, as shown in Table 6-1: . In this context, computational costs are reported for runtimes associated with computing matrix entries, solving linear equations and for the total runtime. All local geochemical reaction calculations were included in computing the matrix entries. Case trans-2d-b and reactran-2d were tested with the hybrid version using 2 threads for each MPI process and the code performance was compared to OpenMP and MPI versions. Case trans-2d-c was tested with the hybrid version using numbers of threads ranging from 2 to 6 for each MPI process. Here nprocs refers to the total number of processors and threads used. As shown in Figure 6-3, performance of the hybrid version depends on the case size and computational cost. For small cases (trans-2d-b) that use low computational resources, as shown in Figure 6-3 (a), the hybrid version does not produce benefits compared to the

OpenMP and MPI versions, indicating that the overhead in the hybrid version cannot be further reduced for this case and that the OpenMP version has much better performance than the other two versions. With geochemical reactions added into the case, the hybrid version generally yields better performance than the MPI version when nprocs is small (e.g., < 10), as shown in Figure 6-3 (b). Performance for matrix entries computations is good and of similar efficiency for all parallel versions, but the hybrid version generally yields better performance as nprocs increases. However, the performance of the linear solver investigated here may deteriorate as nprocs increases, thus slowing the total performance.

To test the role of threads on the performance of the hybrid version, case trans-2d-c was tested for up to 192 total number of processors and threads. As shown in Figure 6-3 (c), using more threads gives better performance as nprocs increases. In this case, when nprocs is less than 10, using 2 threads gives the best performance. Using 4 threads provides the best performance when nprocs is around 100, and 6 threads yield the best performance when nprocs is larger than 100. It can be deduced that performance of the hybrid parallel version depends on the problem size, number of threads per processor and total number of processors and threads used. For the case of limited computer resources, the hybrid version gives better performance when the number of threads per processor is small. In contrast, if more substantial computational resources are available, a larger number of threads per processor provides better performance when using the hybrid version.

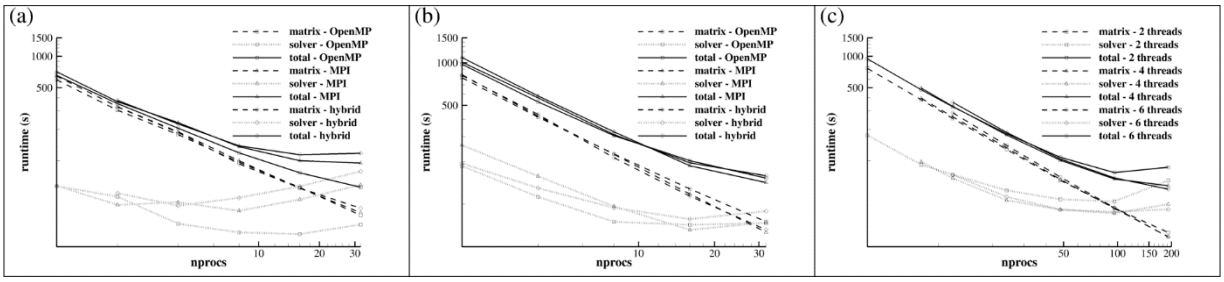

Figure 6-3: Parallel Runtime of Hybrid Version, (a) Case Trans-2d-b, (b) Case Reactran-2d and (c) Case Trans-2d-c

7. Verification of Existing MIN3P-THCm Benchmarks

The verification examples included here cover most of the 2D verification examples included in the current verification problems used for the structured grid version (Xie et al. 2015). In Addition, several demonstration examples were derived from the existing problems. These new problems cover irregular domain shapes.

In a first step, simulation results obtained with MIN3P-THCm V2.0 were verified by comparing the results to previous results obtained with the structured grid version of MIN3P-THCm. For each verification at least three different meshes were used, including one structured mesh and two or three unstructured meshes with different structure or resolution. For the verification of flow problems, the results of hydraulic head or pressure head distribution are shown, together with velocity vectors. For the verification of reactive transport problems, the spatial distribution of concentrations or mineral volume fractions are selected. In addition to the verification using different unstructured meshes, comparison between simulations using Green-Gauss gradient reconstruction and least-squares gradient reconstruction are also given for selected cases. Furthermore, comparison between simulations using the VD method and the MD method are also made for some cases. For the detailed verification of the structured grid version of MIN3P-THCm, which provides the foundation for the current verification of MIN3P-THCm V2.0, we refer to the MIN3P-THCm verification report (Xie et al. 2015).

7.1 Variably Saturated Groundwater Flow

7.1.1 2D Transient Water Table Mounding – Clement Case

7.1.1.1 Problem Definition

This benchmark is a two-dimensional unsaturated water flow problem reported by Vauclin et al. (1979) describing recharge in a water table aquifer. A schematic diagram of the flow domain and experimental details are given in Figure 7-1.

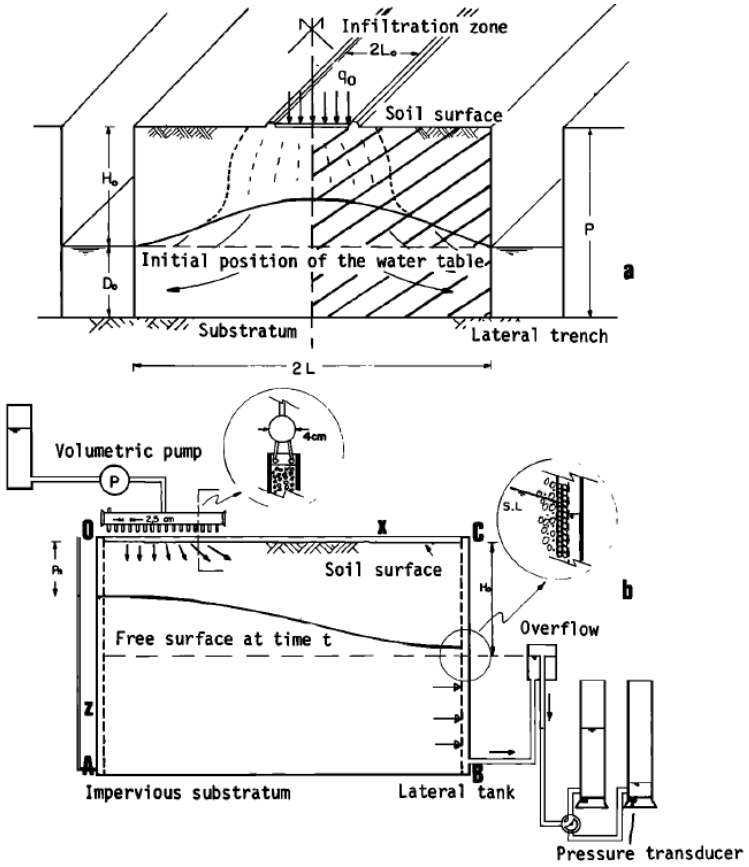

Figure 7-1: (a) Schematic Diagram of the Flow Domain and (b) Experimental Details and Numerical Simulation Domain (Vauclin et al. 1979)

7.1.1.2 Model Setup

The domain of this case is 3.0 m in width and 2.0 m in height. For the structured mesh, the entire domain is discretized into 1271 control volumes yielding a discretization interval of 0.1 m horizontally and 0.05 m vertically for the interior control volumes, and 0.05 m horizontally and 0.025 m vertically for the control volumes on the boundary. For the unstructured mesh three different triangular meshes were used with a range of control volumes: 2542 (mesh USG), 1644 (mesh USG2) and 6296 (mesh USG3), respectively. The four meshes are shown in Figure 7-2.

The initial condition for the flow problem is set at a hydraulic head of 0.65 m for the entire domain. Boundary conditions for the flow problem consist of a flux of 4.11×10^{-5} m s^{-1} on the top-left boundary (0.5 m) and a hydraulic head of 0.65 m on the right side boundary.

For the unstructured mesh simulation, the VD control volume method and the Green-Gauss gradient reconstruction were used.

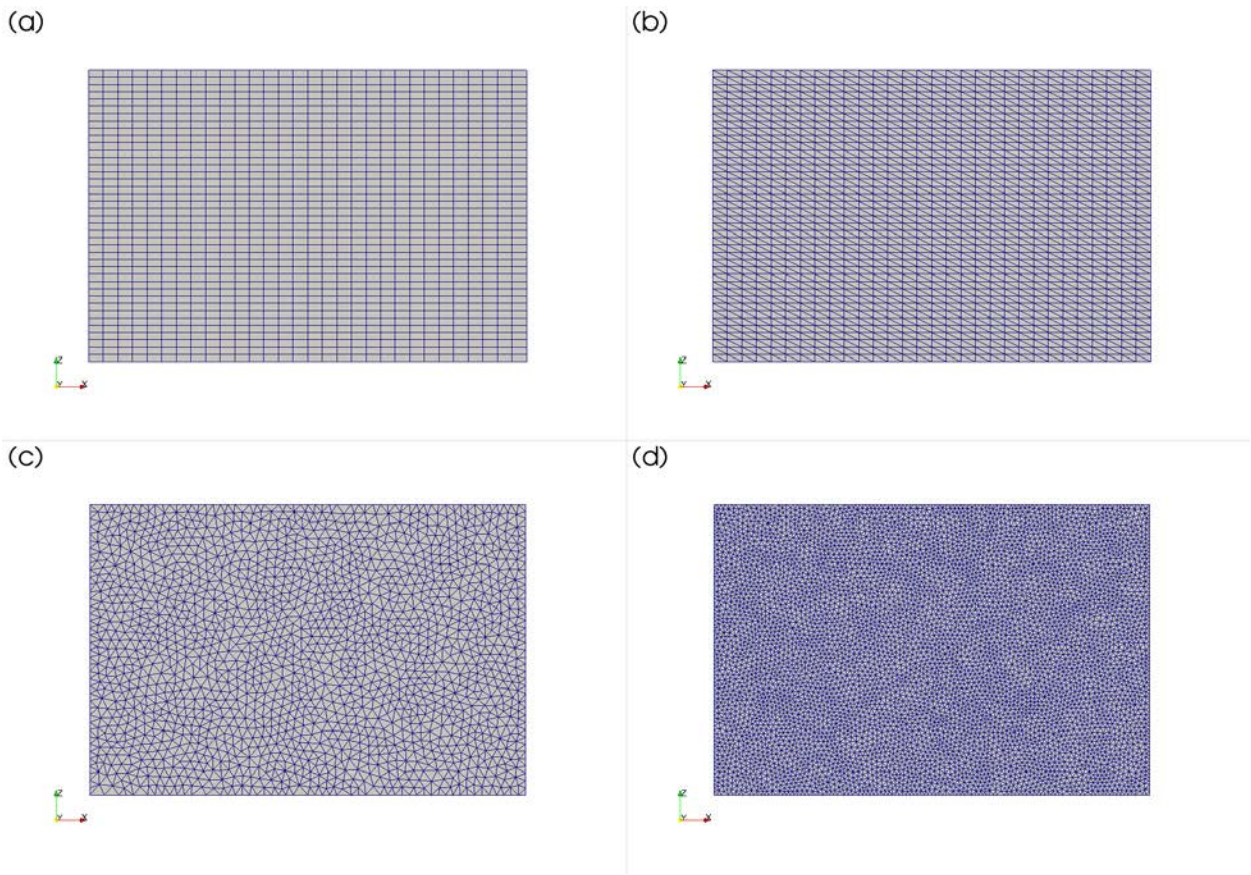

Figure 7-2: Illustration of Meshes Used for Clement Case, (a) Mesh SG, (b) Mesh USG, (c) Mesh USG2, and (d) Mesh USG3

7.1.1.3 Parameters

The physical parameters (material properties) used for the simulations are summarized in Table 7-1.

Table 7-1: Physical Parameters for Benchmark Clement

Parameter	Symbol	Value	Unit
Width of domain	L_x	3.00	m
Height of domain	L_z	2.00	m
Porosity	ϕ	3.00×10^{-1}	-
Hydraulic conductivity	K_{zz}, K_{xx}	9.72×10^{-5}	m s^{-1}
Specific storage coefficient	Ss	0.00	m^{-1}
Residual saturation	S_{ra}	0.01	-
Van Genuchten parameter α	α	3.30	m^{-1}
Van Genuchten parameter n	n	4.10	-

7.1.1.4 Results

Water flow was simulated for a period of 8 hours. The simulated hydraulic head contours after 8 hours are given in Figure 7-3. The numerical predictions of hydraulic head using different meshes are in excellent agreement.

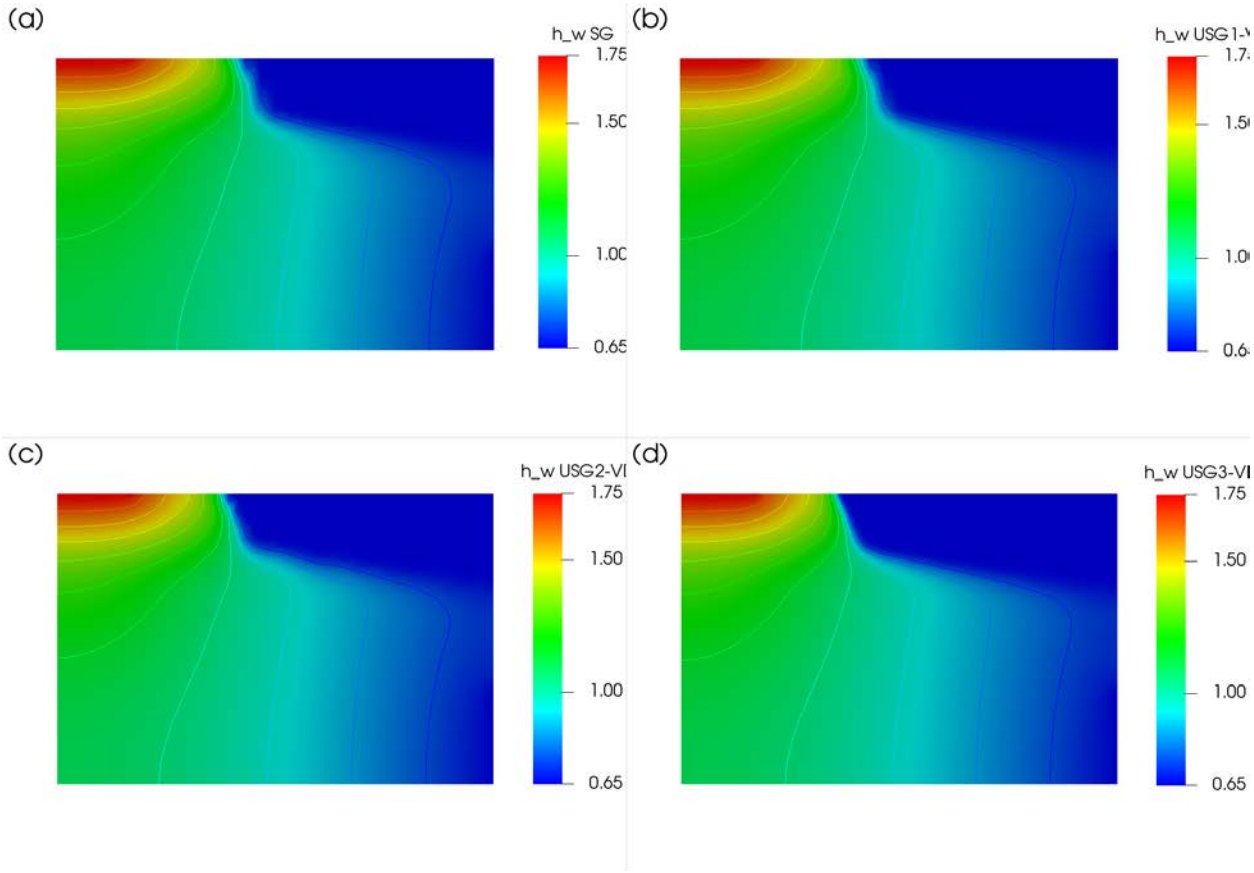

Figure 7-3: Comparison of Hydraulic Head Distributions [m] After 8 Hours Calculated by MIN3P-THCm V1.0 and MIN3P-THCm V2.0 for the Clement Case, (a) Mesh SG, (b) Mesh USG, (c) Mesh USG2, and (d) Mesh USG3

The simulated velocity vectors after 8 hours are depicted in Figure 7-4. The numerical predictions of velocity vectors using different meshes are in good agreement. It should be noted that for the structured mesh the interfacial velocity is used in the plot, while for the unstructured meshes the nodal velocity is used instead. This is necessary because the external file storage of interfacial velocities for the unstructured mesh uses a different format. To maximize model efficiency, nodal velocities are interpolated from interfacial velocities. The advantage of this approach is that all plots are vertex based, using the same mesh data, while the disadvantage is that the interpolation of the velocity values on the boundary or at the interfaces between materials with large differences in hydraulic conductivities may cause non-physical oscillation. Since this does not affect the simulation results of head distribution (Figure 7-3), the inaccurate representation of velocities on the boundaries or the interface of two materials is not significant.

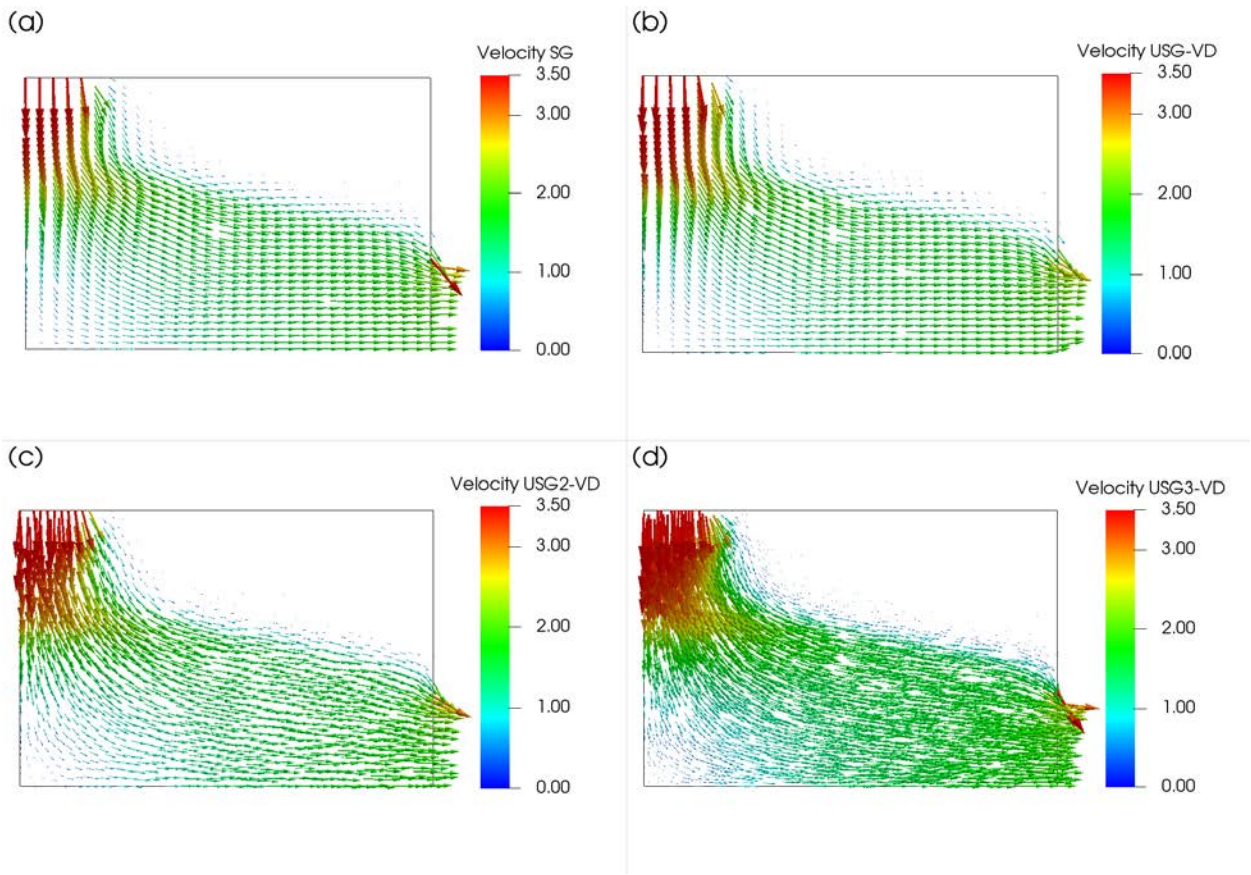

Figure 7-4: Comparison of Velocity Vectors [m day^{-1}] After 8 Hours Calculated by MIN3P-THCm V1.0 and MIN3P-THCm V2.0 for the Clement Case, (a) Mesh SG, (b) Mesh USG, (c) Mesh USG2, and (d) Mesh USG3

7.2 Density Dependent Flow and Conservative Solute Transport

7.2.1 Modified Henry Problem

7.2.1.1 Problem Definition

The modified Henry problem (Croucher and O'Sullivan 1995) describes lateral saltwater intrusion into a homogeneous confined aquifer and the development of a mixing zone between freshwater and saltwater. This problem definition was used to benchmark MIN3P-THCm (Bea et al. 2011).

7.2.1.2 Model Setup

The domain consists of a two-dimensional vertical cross-section, bounded at the top and bottom by no flow boundaries, as shown in Figure 7-5. A constant freshwater flux is applied to the left boundary. The right model boundary represents a hydrostatic column of seawater with a fixed concentration. The model domain extends 2 m in the horizontal direction and 1 m in the vertical direction. For the structured mesh, the domain was discretized using a uniform grid with 861 control volumes (mesh SG) with $\Delta x = \Delta z = 0.05$ m. For the unstructured simulations, the

domain was discretized into 1722 (mesh USG), 618 (mesh USG2) and 2274 (mesh USG3) control volumes, respectively. The four meshes are shown in Figure 7-6.

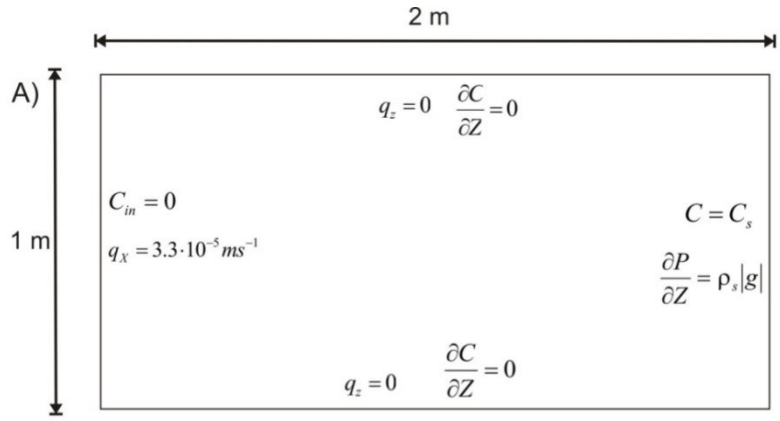

Figure 7-5: Simulation Domain with Flow and Transport Boundary Conditions for Modified Henry Problem

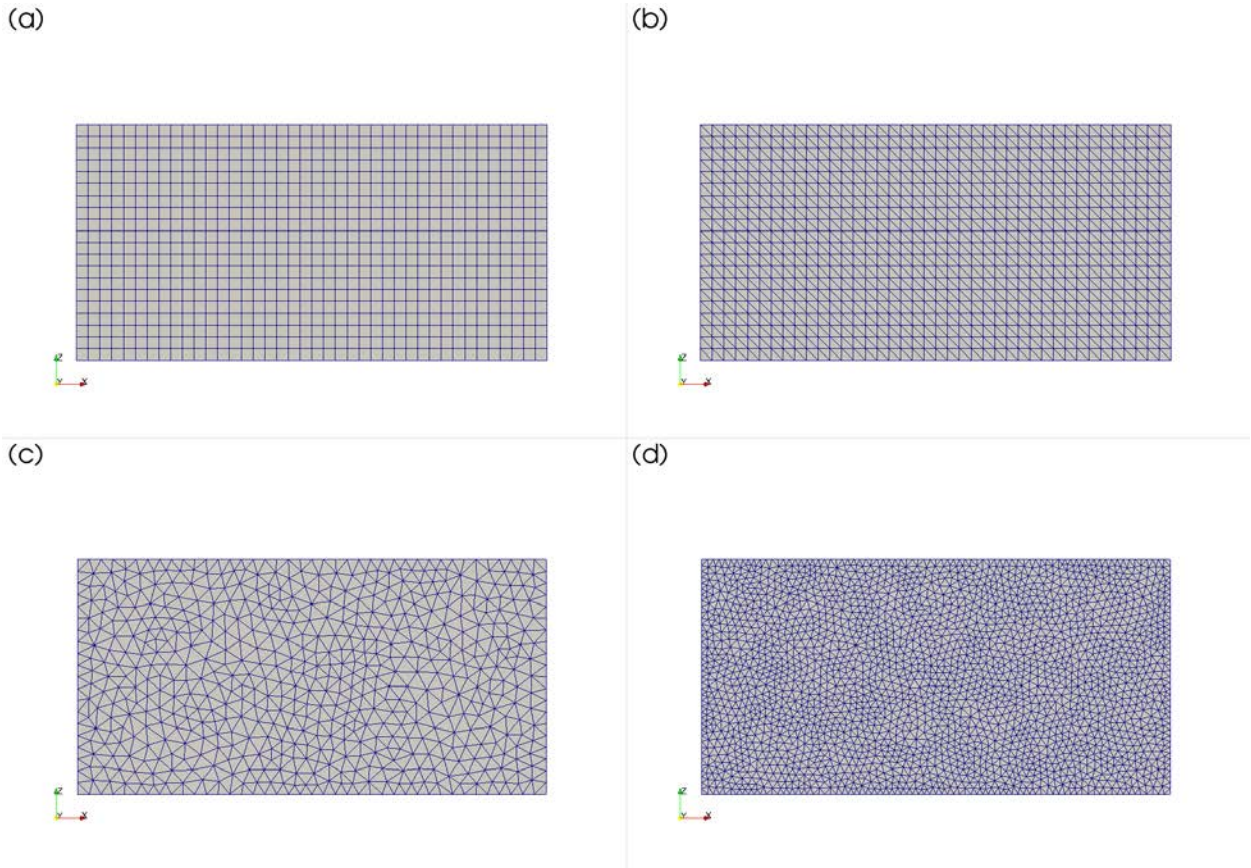

Figure 7-6: Illustration of Meshes Used in Modified Henry Case, (a) Mesh SG, (b) Mesh USG, (c) Mesh USG2, and (d) Mesh USG3

7.2.1.3 Parameters

The MIN3P-THCm V1.0 and MIN3P-THCm V2.0 simulations were performed using the parameter values provided by Simpson and Clement (2004). Flow and transport parameters are summarized in Table 7-2. The Henry problem was simulated for a period of 0.833 days, representing the point at which a stationary solute distribution is achieved.

Table 7-2: Parameters for Modified Henry Saltwater Intrusion Problem (Bea et al. 2011)

Parameter	Symbol	Value	Units
Hydraulic conductivity	K	1.00×10^{-2}	$m\ s^{-1}$
Porosity	ϕ	3.50×10^{-1}	-
Specific storage	S_s	0.00	m^{-1}
Longitudinal dispersivity	α_l	0.00	m
Transverse dispersivity	α_t	0.00	m
Molecular diffusion coefficient	D_0	1.89×10^{-5}	$m^2\ s^{-1}$
Freshwater flux per unit width	q_x	3.30×10^{-5}	$m\ s^{-1}$
Saltwater density	ρ_s	1.03×10^{3}	$kg\ m^{-3}$
Freshwater density	ρ_0	1.00×10^{2}	$kg\ m^{-3}$
Maximum density ratio	ρ_{max}	1.03	-
Coefficient of density variation	$\partial\rho/\partial c$	7.13×10^{-1}	-
Saltwater concentration	C_s	3.50×10^{1}	$g\ L^{-1}$

7.2.1.4 Results

The results in Figure 7-7 show the encroachment of a wedge of saltwater into the freshwater aquifer, in the opposite direction of groundwater flow. The results obtained with the different meshes are in excellent agreement.

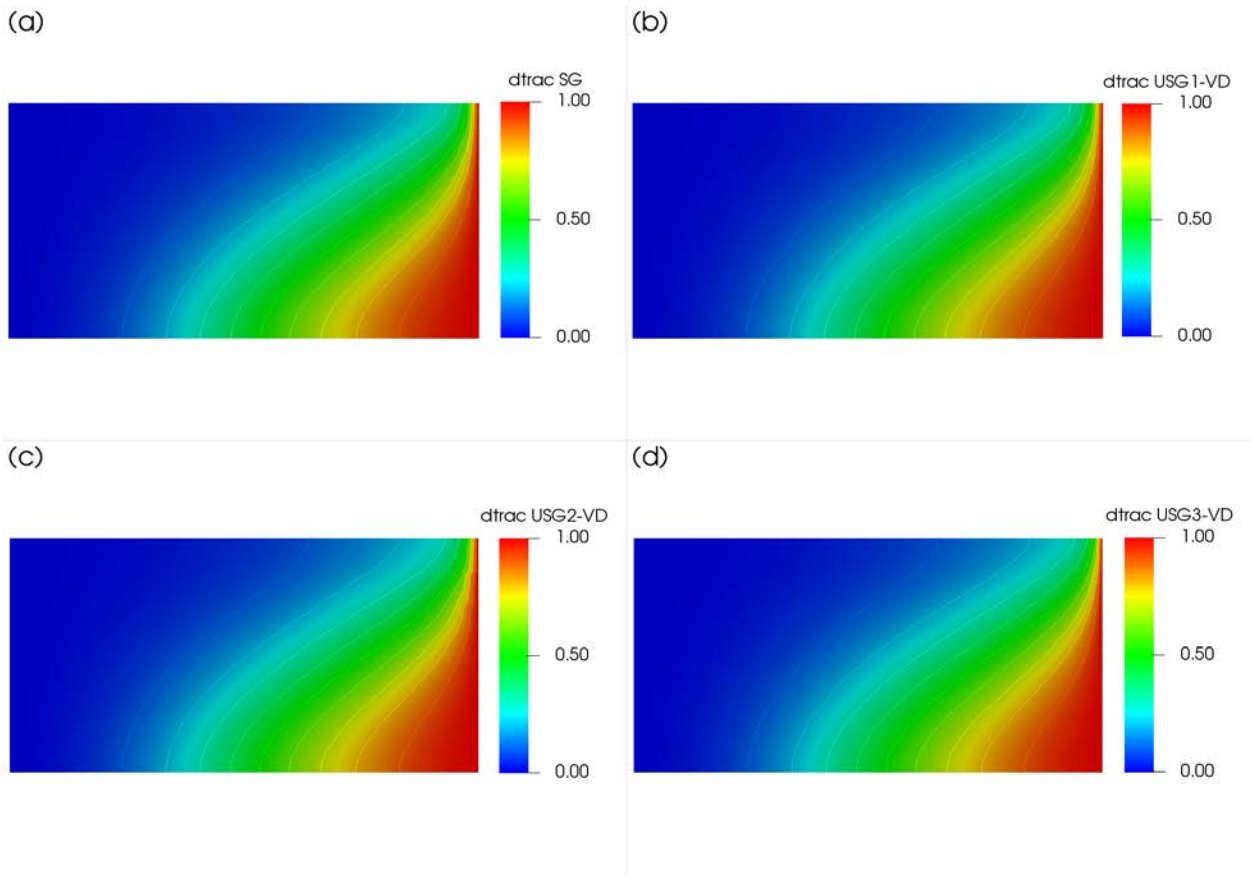

Figure 7-7: Relative Solute Concentration at 0.833 Days Simulated by MIN3P-THCm V1.0 and MIN3P-THCm V2.0, (a) Mesh SG, (b) Mesh USG, (c) Mesh USG2, and (d) Mesh USG3

The simulated velocity vectors after 0.833 days are depicted in Figure 7-8. The numerical predictions of velocity distribution using different meshes are in good agreement. There are some differences between the solutions due to different grid resolutions and for reasons discussed above.

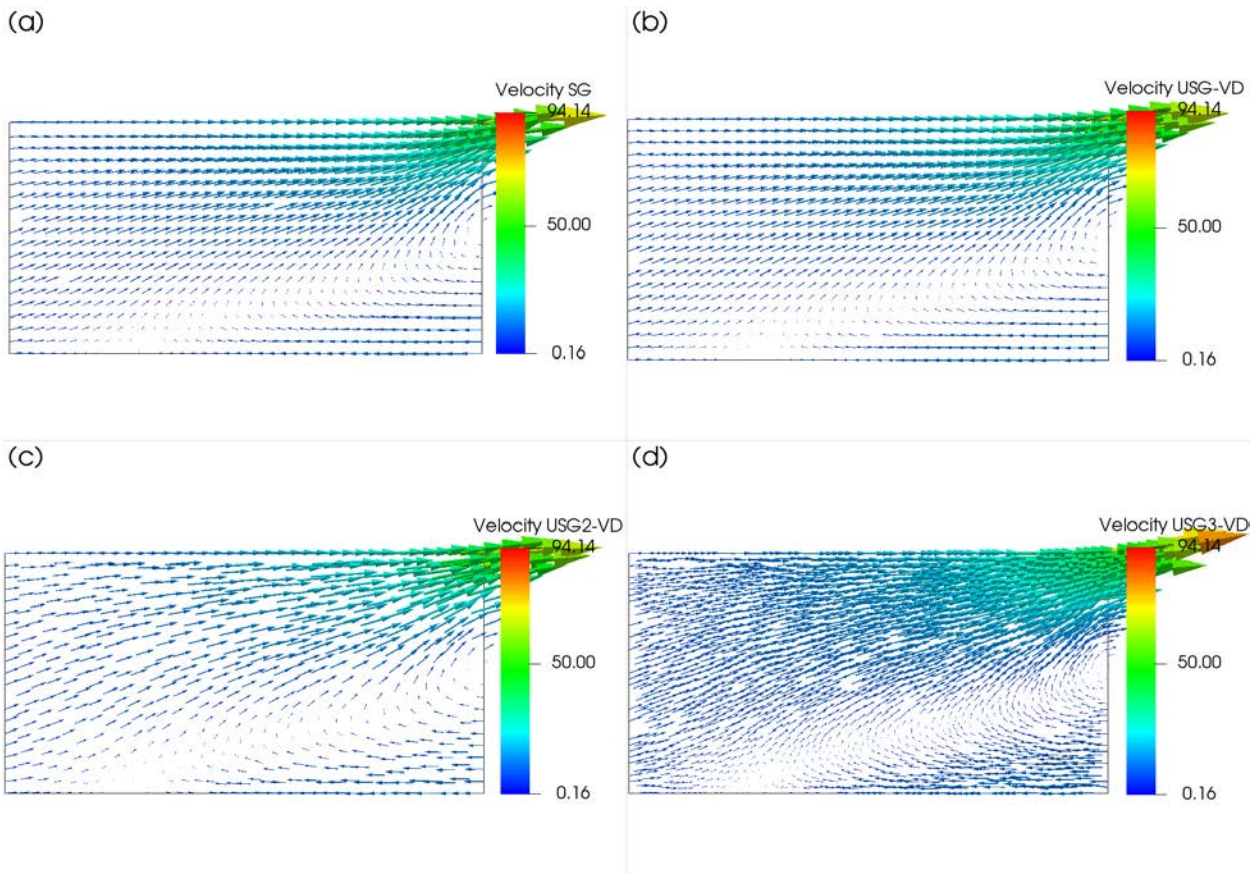

Figure 7-8: Velocity Vectors [m day^{-1}] at 0.833 Days Simulated by MIN3P-THCm V1.0 and MIN3P-THCm V2.0, (a) Mesh SG, (b) Mesh USG, (c) Mesh USG2, and (d) Mesh USG3

7.3 Heat and Solute Transport

7.3.1 Density Dependent Flow with Heat and Solute Transport

7.3.1.1 Problem Definition

This benchmark considers seawater intrusion into a non-isothermal confined aquifer under transient conditions (Henry and Hilleke 1972). Freshwater flows from an inland boundary over dense saline water, which enters from a seaward boundary, and discharges along the upper portions of the vertical seaward boundary.

7.3.1.2 Model Setup

The benchmark simulates a two-dimensional cross section (1.0 m in length and 1.0 m in height). Initially, hydrostatic pressure conditions are present throughout the aquifer with linear variations of seawater concentrations and temperatures, as shown in Figure 7-9.

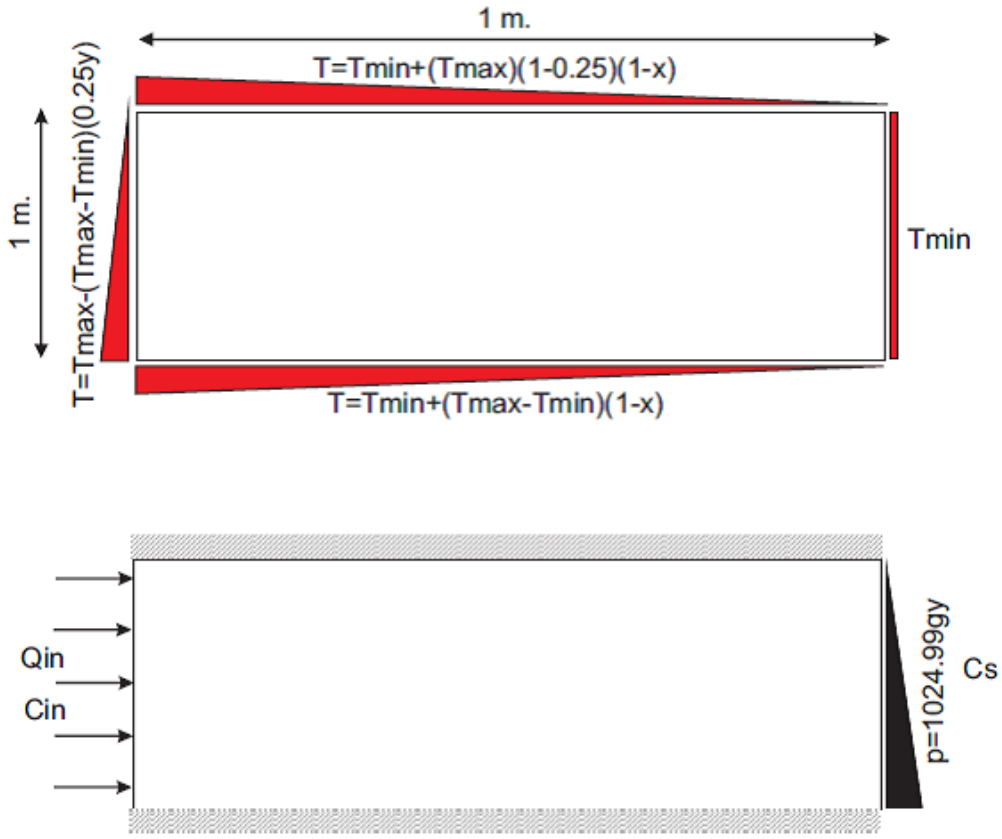

Figure 7-9: Boundary Conditions of Henry-Hilleke Problem (a) Domain and Energy Transport Boundary Condition and (b) Flow and Solute Transport Boundary Conditions

For the structured mesh, the domain was discretized using a uniform grid with 2091 control volumes (mesh SG) with $\Delta x = 0.025$ m and $\Delta z = 0.02$ m. For the unstructured meshes, the domain was discretized into 4182 (mesh USG), 1688 (mesh USG2) and 6605 (mesh USG3) control volumes, respectively. The four meshes are shown in Figure 7-10.

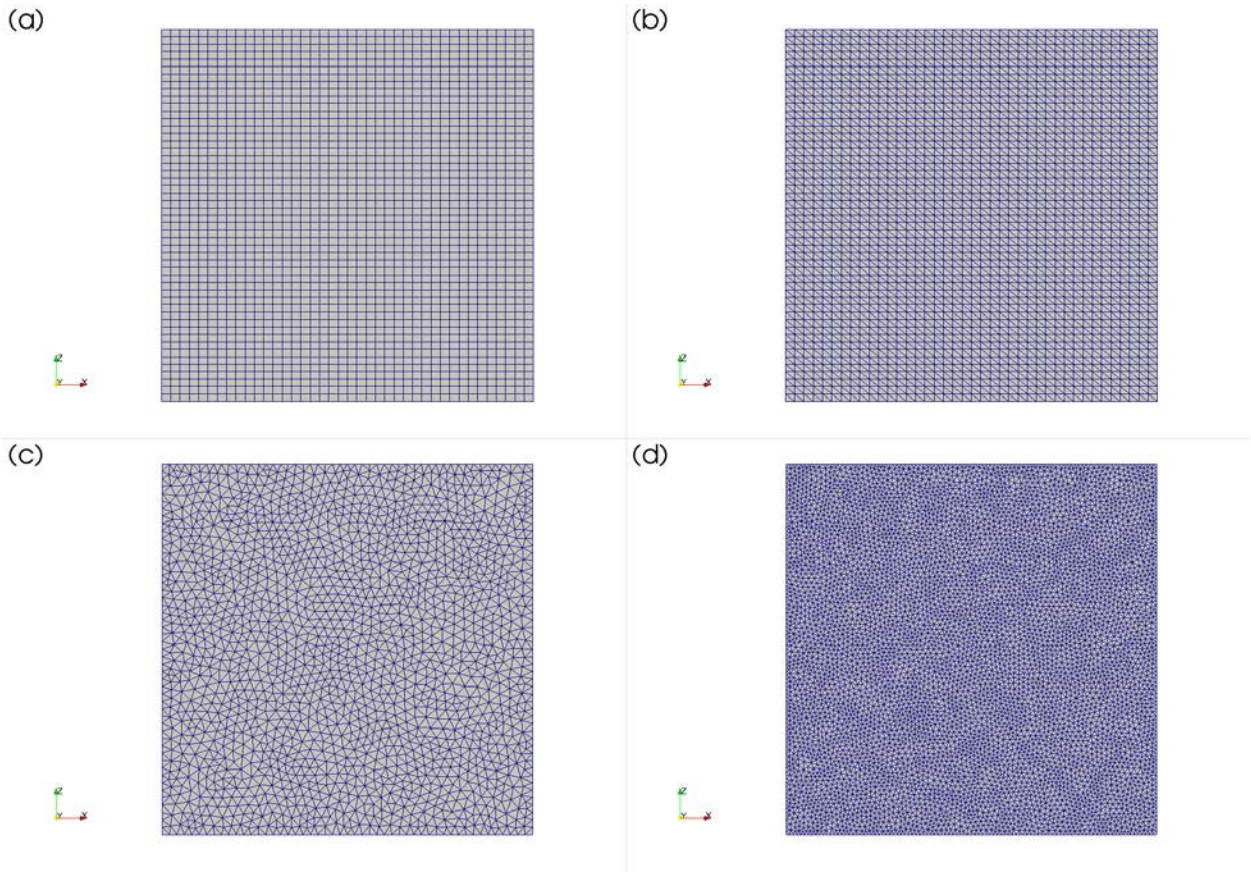

Figure 7-10: Illustration of Meshes Used in Henry-Hilleke Case, (a) Mesh SG, (b) Mesh USG, (c) Mesh USG2 and (d) Mesh USG3

7.3.1.3 Parameters

Parameters for the Henry-Hilleke problem are provided in Table 7-3.

Table 7-3: Parameters for Henry-Hilleke Problem (Bea et al. 2011)

Parameter	Value	Unit
Solid density	2.60×10^{3}	kg m^{-3}
Fresh-water density	1.00×10^{3}	kg m^{-3}
Sea-water density	1.02×10^{3}	kg m^{-3}
Dynamic fluid viscosity	1.00×10^{-3}	kg m^{-1} s^{-1}
Concentration C_s	3.57×10^{1}	kg m^{-3}
Concentration C_{in}	0.00	kg m^{-3}
Injection rate Q_{in}	8.33×10^{-6}	kg s^{-1}
Porosity	3.50×10^{-1}	-
Permeability	1.20×10^{-9}	m^2
Diffusion-dispersion (solute transport)	2.38×10^{-5}	m^2 s^{-1}
Diffusion-dispersion (energy transport)	2.38×10^{-4}	m^2 s^{-1}
Water thermal conductivity	9.96×10^{2}	J s^{-1} m^{-1} $^oC^{-1}$
Solid thermal conductivity	0.00	J s^{-1} m^{-1} $^oC^{-1}$
Specific heat capacity of water	4.18×10^{3}	J kg^{-1} $^oC^{-1}$
Rock Density	2.65×10^{3}	kg m^{-3}
T_{min}	5.00	^oC
T_{max}	5.00×10^{1}	^oC
$\frac{\partial \rho}{\partial TDS}$	7.00×10^{-1}	-
$\frac{\partial \rho}{\partial T}$	-3.75×10^{-1}	kg m^{-3} $^oC^{-1}$

7.3.1.4 Results

Simulation results depict the seawater isochlors (Figure 7-12). Comparing the results against each other demonstrates excellent agreement for the different meshes.

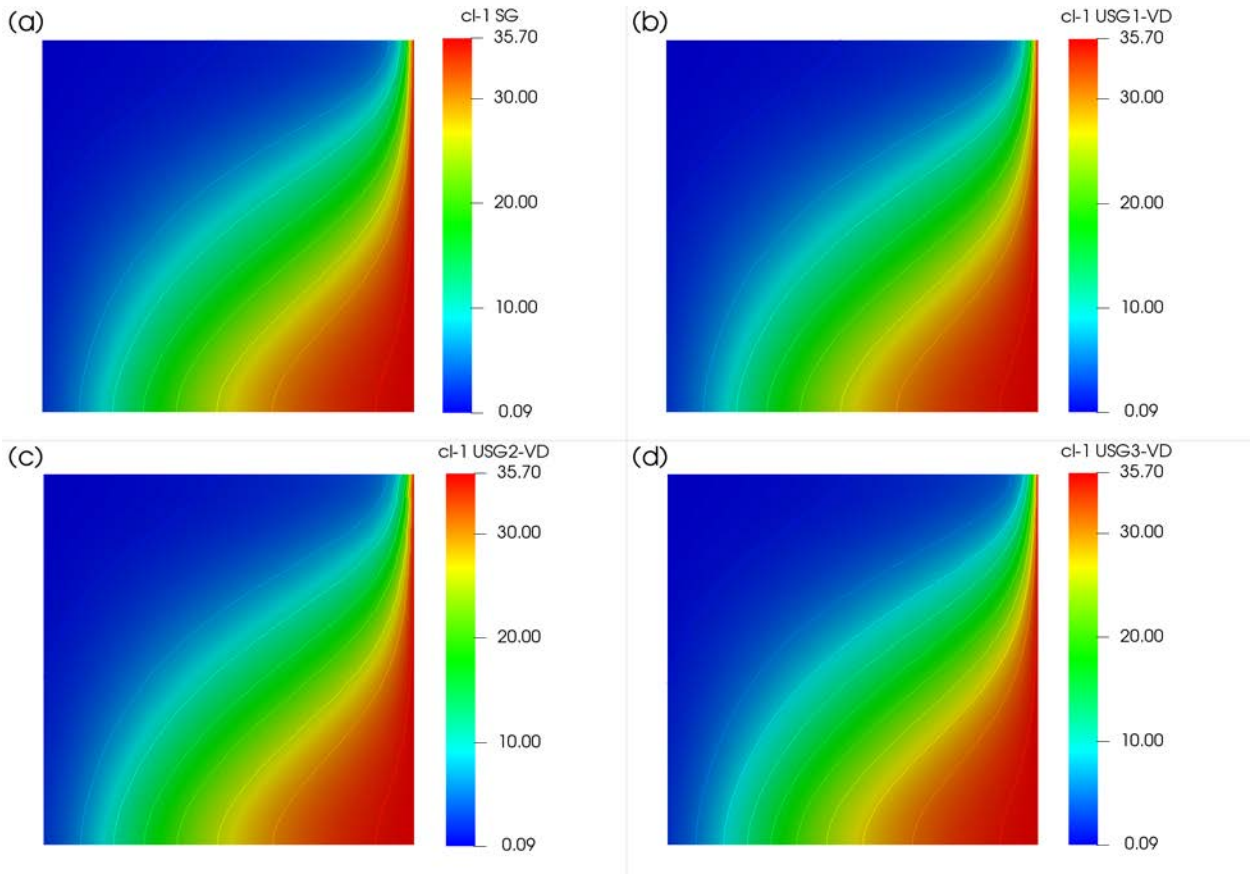

Figure 7-11: Percent Seawater Isochlors for the Henry-Hilleke Problem Simulated by MIN3P-THCm V1.0 and MIN3P-THCm V2.0, (a) Mesh SG, (b) Mesh USG, (c) Mesh USG2, and (d) Mesh USG3

The simulated velocity vectors are given in Figure 7-12. The numerical predictions of velocity distributions using different meshes are in good agreement, reflecting differences in discretization.

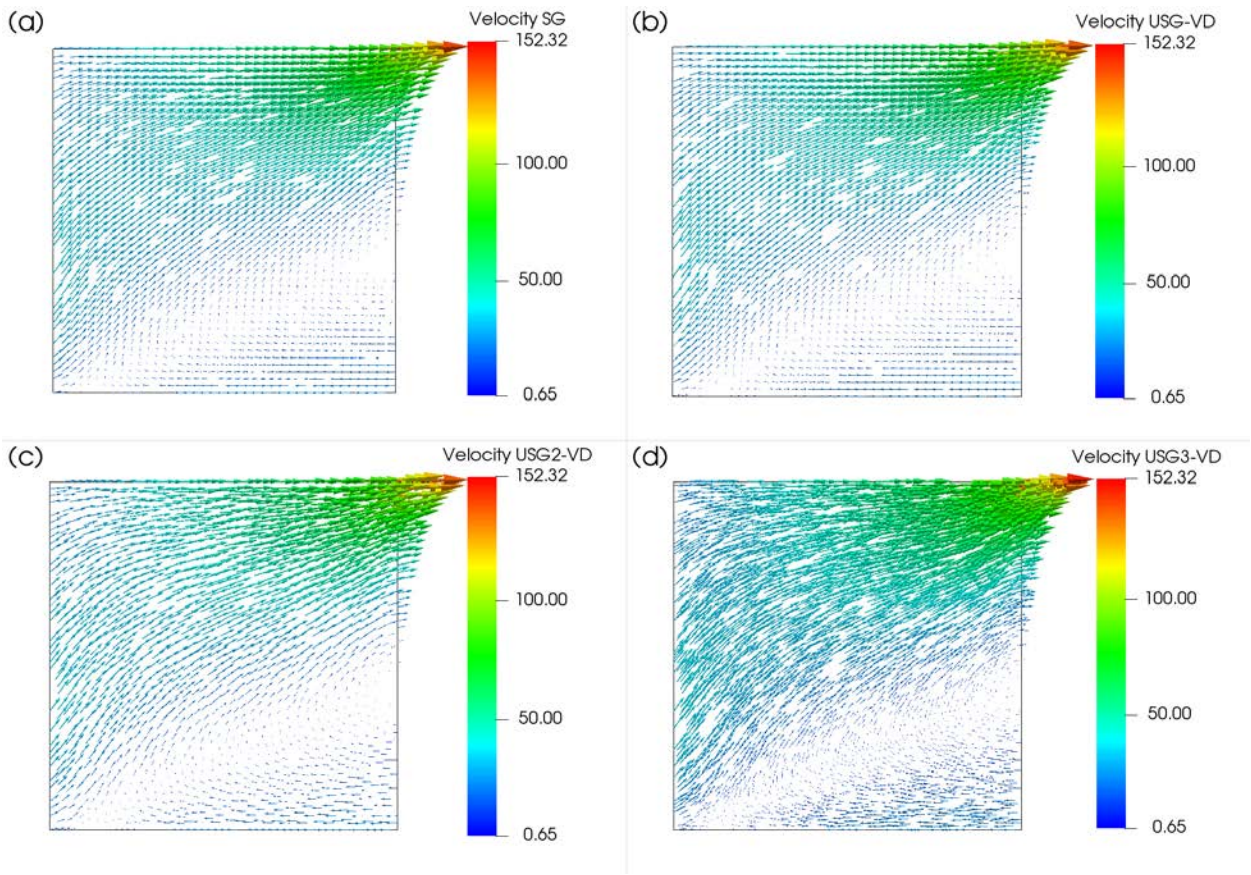

Figure 7-12: Velocity Vectors [m day^{-1}] for the Henry-Hilleke Problem Simulated by MIN3P-THCm V1.0 and MIN3P-THCm V2.0, (a) Mesh SG, (b) Mesh USG, (c) Mesh USG2, and (d) Mesh USG3

7.4 Multicomponent Reactive Transport

7.4.1 Uranium Remediation by Lactate Injection

7.4.1.1 Problem Definition

This case explores the hydro-geochemical patterns that develop under transient groundwater flow conditions during uranium bioremediation, following the work of Şengör et al.(2015). The main challenge of this case is the complexity of the biogeochemical reaction network, which includes various parallel, sequential and competing kinetic reactions with strong nonlinear interdependency of processes. In addition, some of the reactions are mixing-controlled and the reaction progress as well as the resulting solution are highly sensitive to physical mixing and therefore potentially compromised by numerical dispersion. These characteristics cause a strong coupling between the physical transport and geochemical reactions. The problem also includes injection of a treatment solution. Some parts of the domain will at times see no changes, while other regions see substantial and rapid changes in flow rates and aqueous concentrations in response to the injection. Since this case is very time consuming using fine resolution meshes and long-term lactate injection, the spatial discretization and lactate injection

time as well as the total simulation time have been modified for this report to reduce execution times.

7.4.1.2 Model Setup

The model domain for the 2D simulation is 18 m in length and 10.5 m in width. An injection well is located 7.25 m downstream from the influent boundary. The injection of a lactate-containing solution was simulated at this location at a rate of 0.2 m^3 day^{-1} during the initial 4 days (modified from 8 days in Şengör et al., 2015), as shown in Figure 7-13. The simulation was conducted using a longitudinal dispersivity of 1 m and a transverse dispersivity of 0.1 m. The total simulation period was set at 8 days (modified from 60 days in (Şengör et al. 2015)) with a nominal time step size of 0.01 days.

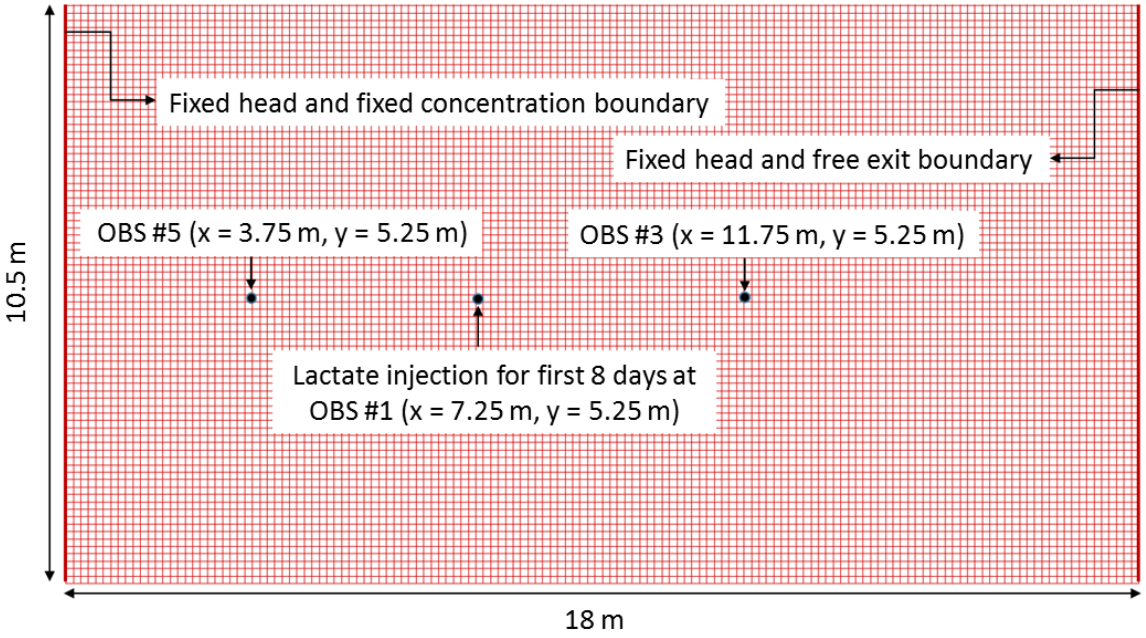

Figure 7-13: Simulation Domain and Boundary Conditions for the Uranium Bioremediation Case

The structured mesh and the three unstructured meshes are shown in Figure 7-14. For the structured mesh, a uniform grid discretization of 0.5 m in both the horizontal and vertical directions was used, resulting in 814 control volumes, as shown in Figure 7-14 (a). For the unstructured meshes, three different meshes with 1628 (Figure 7-14 b), 562 (Figure 7-14 c) and 2062 (Figure 7-14 d) control volumes were used.

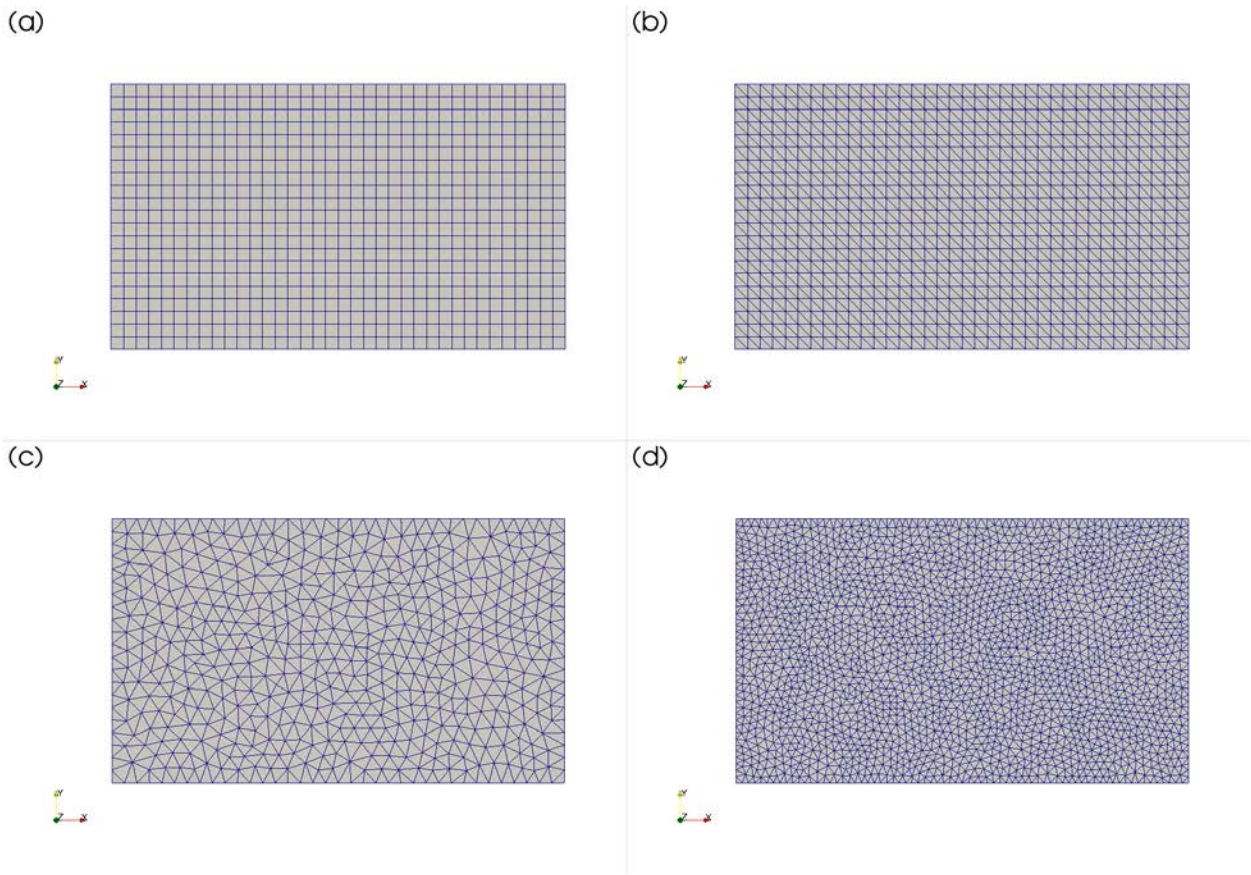

Figure 7-14: Illustration of Meshes Used in the Uranium Bioremediation Case, (a) Mesh SG, (b) Mesh USG, (c) Mesh USG2 and (d) Mesh USG3

7.4.1.3 Parameters

We refer to Şengör et al. (2015) for the detailed parameter set.

7.4.1.4 Results

Concentration distributions for selected aqueous components and biomass at 8 days are shown in Figure 7-15 to Figure 7-18. The results for the different meshes are in good agreement. Since this case is highly sensitive to physical mixing, the results are compromised by numerical dispersion, especially for mesh SG and mesh USG. In this case, the unstructured grid simulations give more representative results. Results obtained using the structured grid and the USG grid suffer from diagonal flow across the grid alignment, leading to somewhat distorted concentration distributions in response to the injection. Results obtained with USG3 provide the best solution to the problem, showing that unstructured grids are beneficial, even for regular domains.

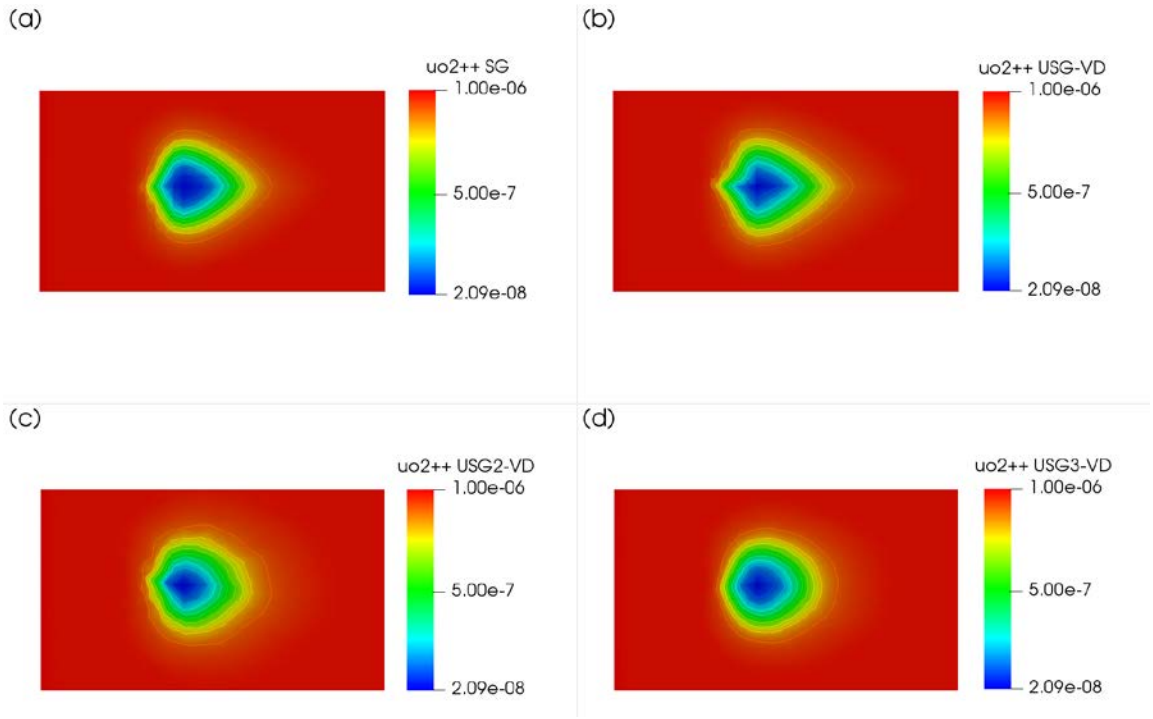

Figure 7-15: Concentrations of Fe^{2+} [mol L^{-1}] Calculated by MIN3P-THCm V1.0 and MIN3P-THCm V2.0, (a) Mesh SG, (b) Mesh USG, (c) Mesh USG2, and (d) Mesh USG3

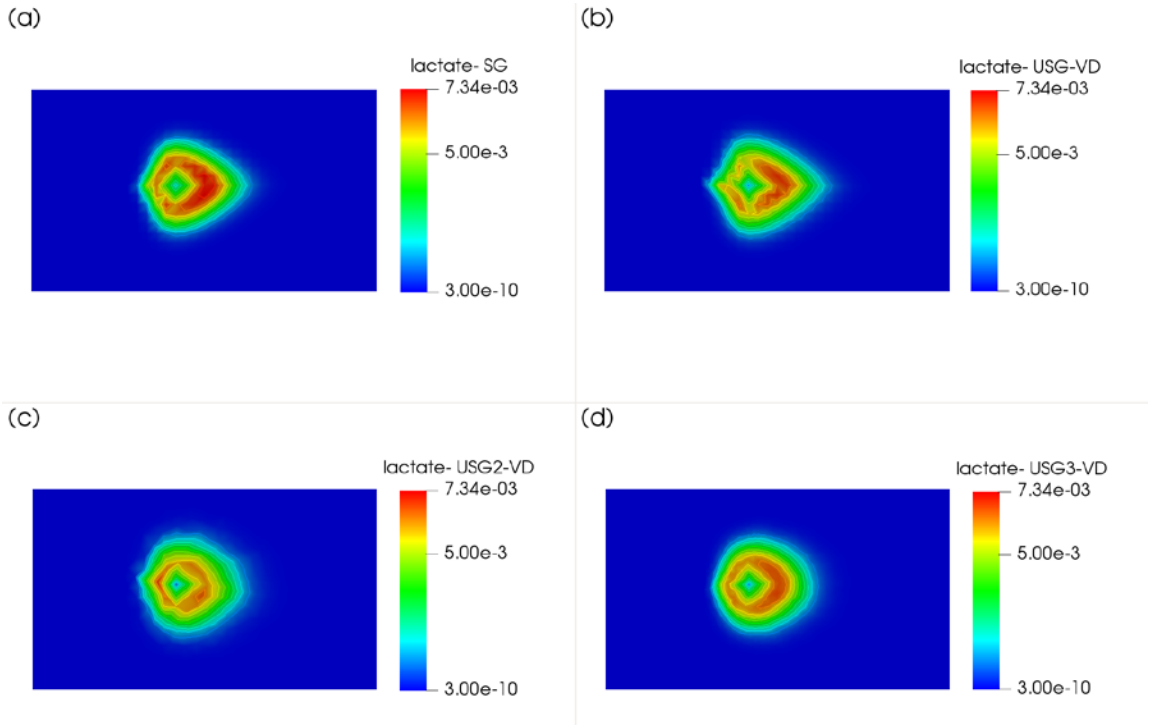

Figure 7-16: Concentrations of Lactate [mol L^{-1}] Calculated by MIN3P-THCm V1.0 and MIN3P-THCm V2.0, (a) Mesh SG, (b) Mesh USG, (c) Mesh USG2 and (d) Mesh USG3

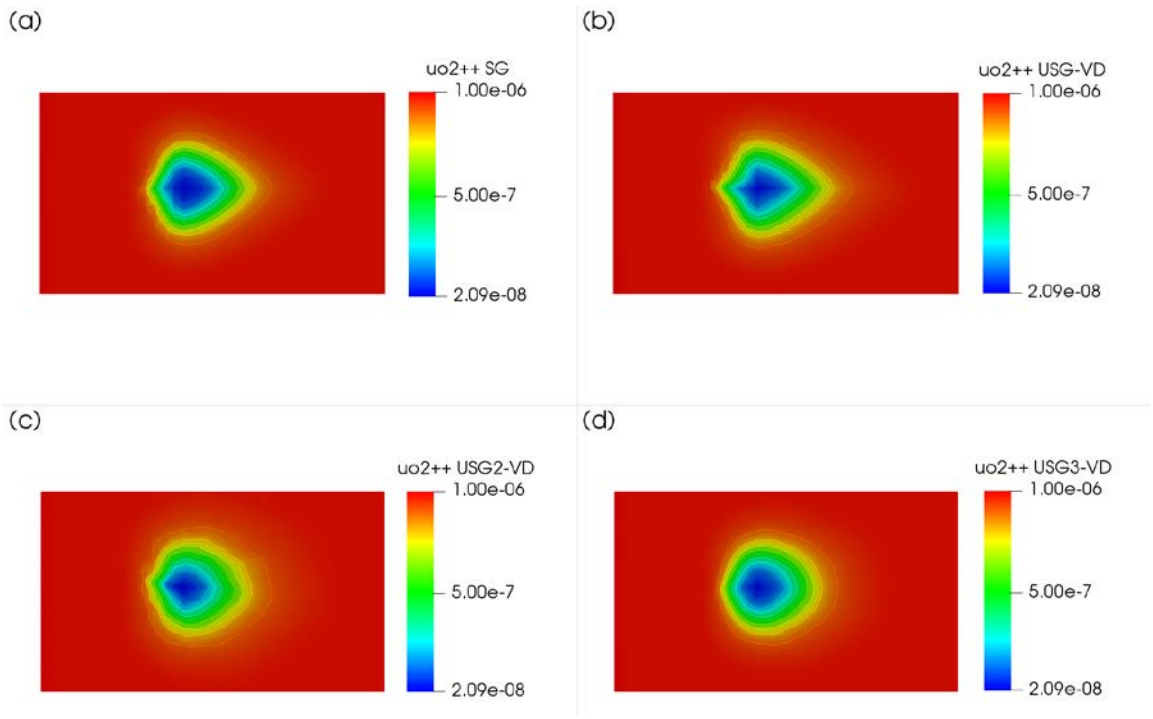

Figure 7-17: Concentrations of UO_2^{2+} [mol L^{-1}] Calculated by MIN3P-THCm V1.0 and MIN3P-THCm V2.0, (a) Mesh SG, (b) Mesh USG, (c) Mesh USG2, and (d) Mesh USG3

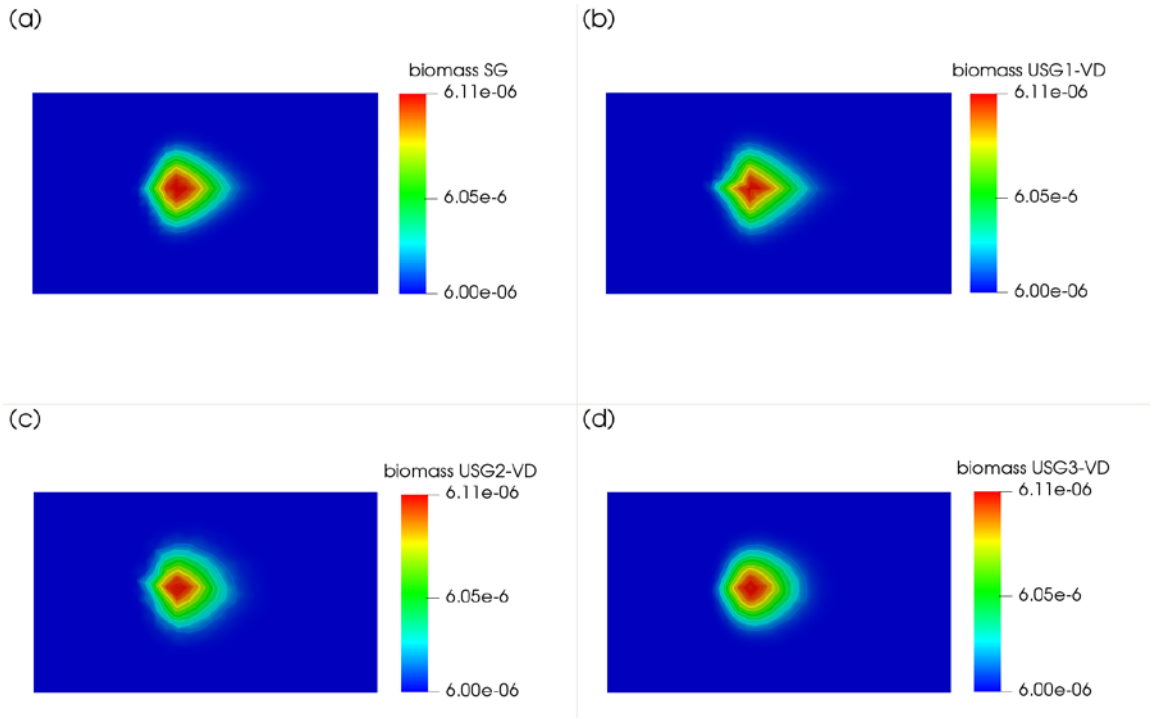

Figure 7-18: Concentrations of Biomass [mol L^{-1}] Calculated by MIN3P-THCm V1.0 and MIN3P-THCm V2.0, (a) Mesh SG, (b) Mesh USG, (c) Mesh USG2 and (d) Mesh USG3

The simulated velocity vectors are shown in Figure 7-19. The numerical predictions of velocity distributions using different meshes are overall in good agreement. It should be noted that the large velocity vectors in mesh SG are caused by differences in spatial discretization. For the lactate injection event, the interface area for mesh SG and USG3 for the injection location is smaller than that of mesh USG and mesh USG2, resulting in relatively large velocities near the injection point.

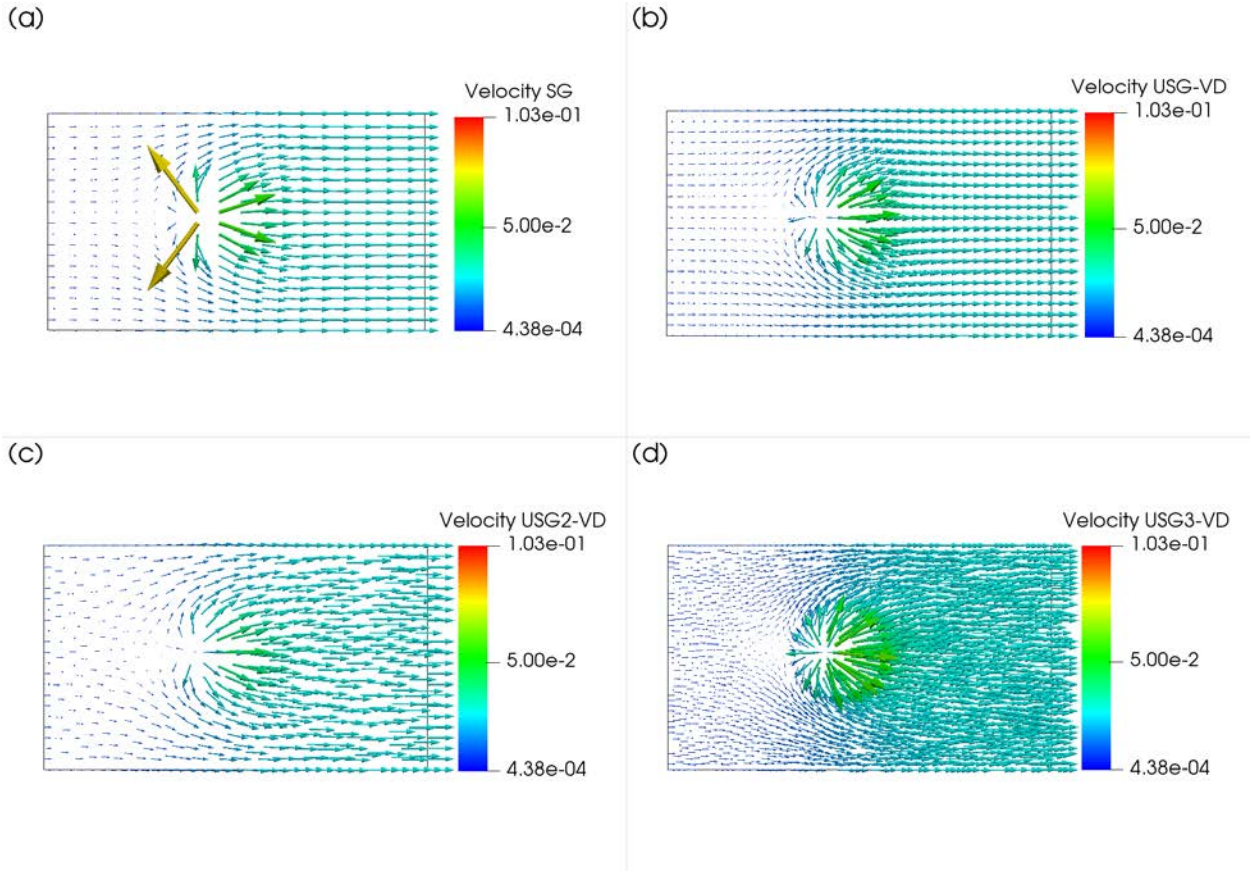

Figure 7-19: Velocity Vectors [m day^{-1}] Calculated by MIN3P-THCm V1.0 and MIN3P-THCm V2.0, (a) Mesh SG, (b) Mesh USG, (c) Mesh USG2, and (d) Mesh USG3

8. Demonstration Examples - Existing MIN3P-THCm Benchmarks

In this section, the applicability of the unstructured grid code is demonstrated for selected MIN3P-THCm benchmarks, including variably saturated flow and reactive transport in complex domains. These benchmarks are not verified against experimental data or against other codes. However, the results obtained from simulations using the unstructured mesh are compared to those obtained from structured mesh. These examples are included here to demonstrate model applicability to a range of problems.

8.1 Variably Saturated Groundwater Flow

8.1.1 2D Variably-Saturated Steady State Flow with Seepage

8.1.1.1 Problem Definition

This demonstration example is a two-dimensional variably-saturated, steady-state flow problem reported by Davis and Neuman (1983).

8.1.1.2 Model Setup

The simulation domain is 6.0 m in width and 1.2 m in height. As shown in Figure 8-1, for the structured mesh, the domain was discretized into 3146 control volumes (mesh SG) yielding a discretization interval of 0.05 m in width and 0.048 m in height for the interior control volumes, and 0.025 m in width and 0.024 m in height for the control volumes on the boundary. For the unstructured meshes, the simulation domain was discretized into 6292, 1972 and 7403 control volumes, respectively.

The initial condition for the flow problem is a hydraulic head of 0 m for the entire domain. Boundary conditions for the flow problem consist of a flux of 1.20×10^{-6} m s^{-1} on the top boundary, a hydraulic head of 0 m on the left bottom boundary, and a seepage face condition on the left boundary.

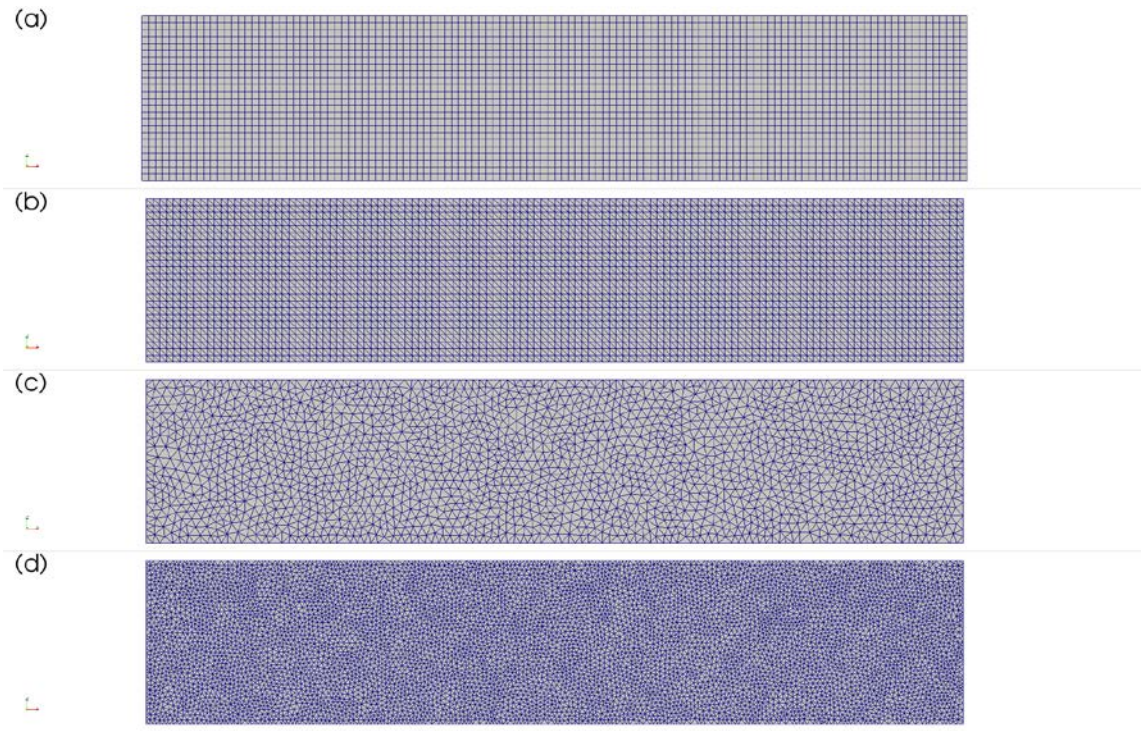

Figure 8-1: Illustration of Meshes Used for 2D Variably-saturated Steady State Flow Demonstration Example with Seepage, (a) Mesh SG, (b) Mesh USG, (c) Mesh USG2 and (d) Mesh USG3

8.1.1.3 Parameters

The physical parameters (material properties) used for the simulations are summarized in Table 8-1.

Table 8-1: Physical Parameters for 2D Variably-saturated Steady State Flow Demonstration Example with Seepage

Parameter	Symbol	Value	Unit
Width of domain	L_x	6.00	m
Height of domain	L_z	1.20	m
Porosity	ϕ	3.48×10^{-1}	-
Hydraulic conductivity	K_{zz}, K_{xx}	6.43×10^{-5}	m s^{-1}
Specific storage coefficient	Ss	0.00	-
Residual saturation	S_{ra}	4.95×10^{-2}	-
Van Genuchten parameter α	α	3.43	m^{-1}
Van Genuchten parameter n	n	4.71	-

8.1.1.4 Results

The simulated hydraulic head contours are provided in Figure 8-2 and the simulated velocity vectors are provided in Figure 8-3. The results obtained with the different meshes are in good agreement.

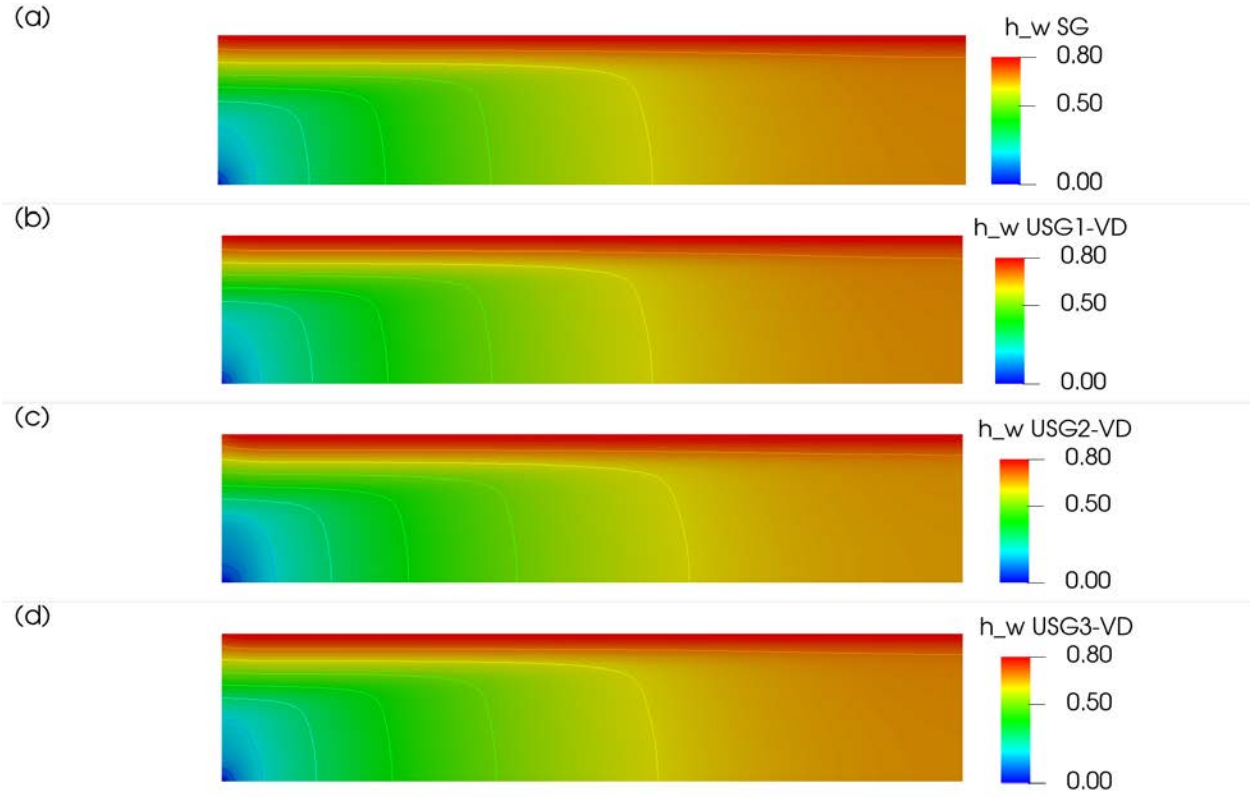

Figure 8-2: Distribution of Hydraulic Head [m] for 2D Variably-saturated Steady State Flow Demonstration Example with Seepage Calculated by MIN3P-THCm V1.0 and MIN3P-THCm V2.0, (a) Mesh SG, (b) Mesh USG, (c) Mesh USG2 and (d) Mesh USG3

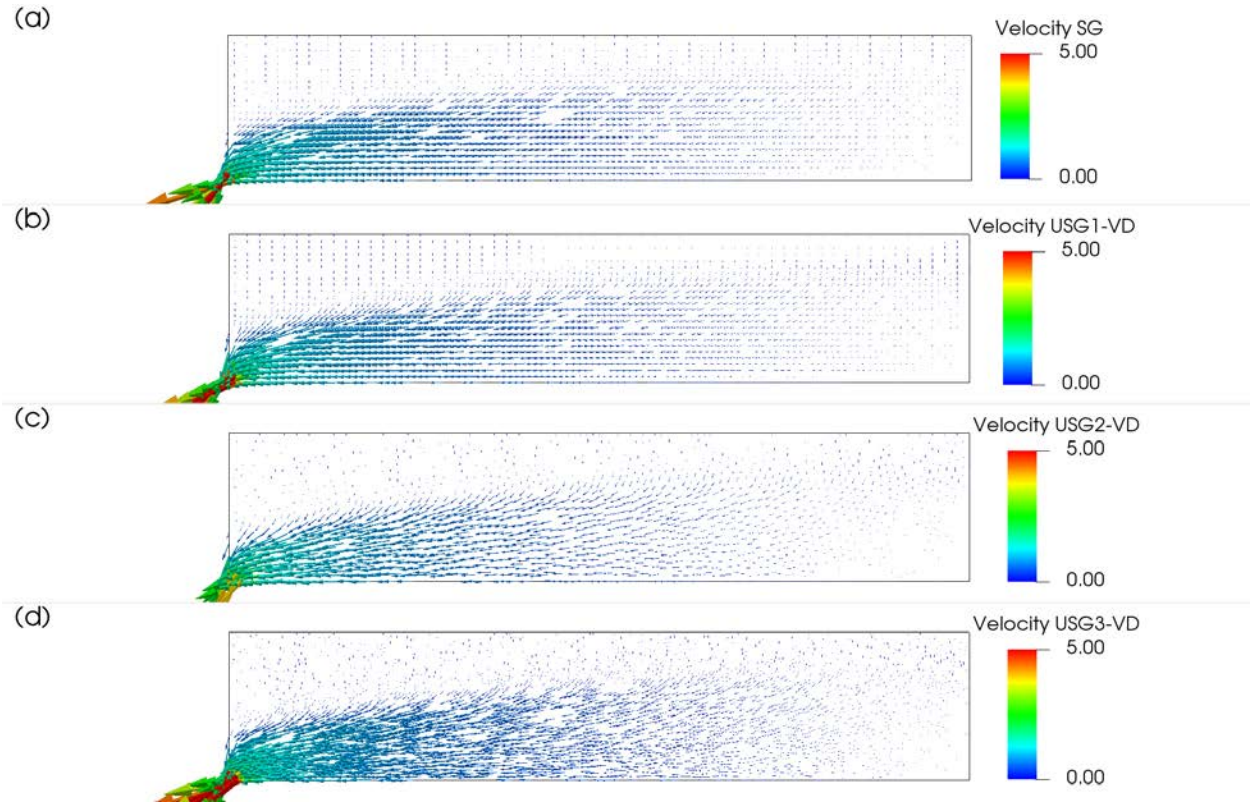

Figure 8-3: Distribution of Velocity Vectors [m day^{-1}] for 2D Variably-saturated Steady State Flow Demonstration Example with Seepage Calculated by MIN3P-THCm V1.0 and MIN3P-THCm V2.0, (a) Mesh SG, (b) Mesh USG, (c) Mesh USG2 and (d) Mesh USG3

8.1.2 2D Variably-Saturated Transient Flow with Seepage

8.1.2.1 Problem Definition

This demonstration example is a two-dimensional variably-saturated transient flow problem reported by Davis and Neuman (1983). The problem is identical to the demonstration example described above, with the exception that transient flow is considered.

8.1.2.2 Model Setup

The simulation domain and spatial discretization are identical to the corresponding steady state flow example, as shown in Figure 8-1. The initial condition for the flow problem is a hydraulic head of 0 m for the entire domain. Boundary conditions for the flow problem consist of a flux of 1.20×10^{-6} m/s on the top boundary, a hydraulic head of 0 m on the left bottom boundary, and a seepage face on the left boundary.

8.1.2.3 Parameters

The physical parameters (material properties) used for the simulations are summarized in Table 8-2.

Table 8-2: Physical Parameters for 2D Variably-saturated Transient Flow Demonstration Example with Seepage

Parameter	Symbol	Value	Unit
Width of domain	L_x	6.00	m
Height of domain	L_z	1.20	m
Porosity	ϕ	3.48×10^{-1}	-
Hydraulic conductivity	K_{zz}, K_{xx}	6.43×10^{-5}	m s^{-1}
Specific storage coefficient	Ss	0.00	-
Residual saturation	S_{ra}	4.95×10^{-2}	-
Van Genuchten parameter α	α	3.43	m^{-1}
Van Genuchten parameter n	n	4.71	-

8.1.2.4 Results

Water flow was simulated for a period of 8 days. The simulated hydraulic heads and velocity vectors are shown in Figure 8-4 and Figure 8-5. The results obtained using the different meshes are again in good agreement.

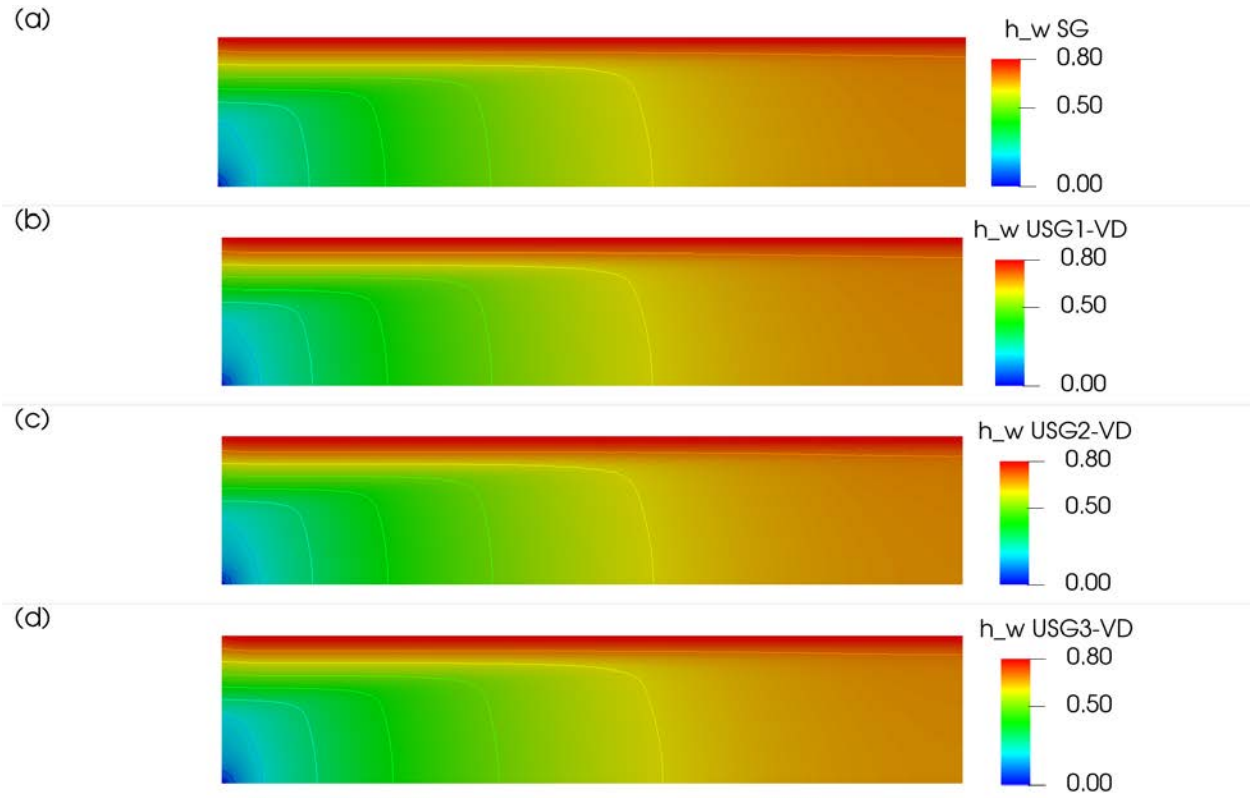

Figure 8-4: Distribution of Hydraulic Head [m] for 2D variably-saturated Transient Flow Demonstration Example with Seepage Calculated by MIN3P-THCm V1.0 and MIN3P-THCm V2.0, (a) Mesh SG, (b) Mesh USG, (c) Mesh USG2 and (d) Mesh USG3

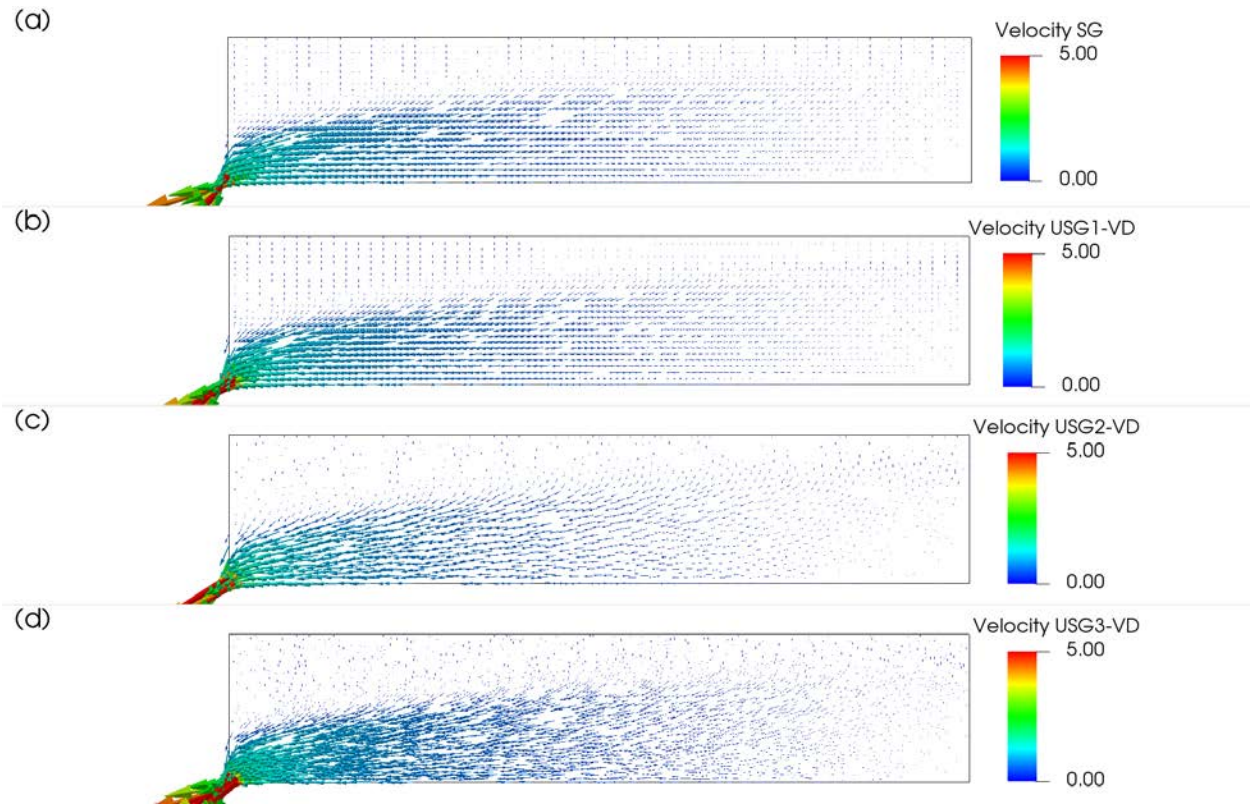

Figure 8-5: Distribution of Velocity Vectors [m day^{-1}] for 2D Variably-saturated Transient Flow Demonstration Example with Seepage Calculated by MIN3P-THCm V1.0 and MIN3P-THCm V2.0, (a) Mesh SG, (b) Mesh USG, (c) Mesh USG2 and (d) Mesh USG3

8.1.3 2D Steady State Fully Saturated Flow

8.1.3.1 Problem Definition

This demonstration example (entitled “stedfs”) simulates two-dimensional steady state fully-saturated flow.

8.1.3.2 Model Setup

The simulation domain is 1.0 m in width, and 1.0 m in height. For the structured mesh, the domain was discretized into 121 control volumes (mesh SG) yielding a discretization interval of 0.1 m for the interior control volumes and 0.05 m for the control volumes on the boundary. For the unstructured meshes, the domain was discretized into 242, 128 and 1221 control volumes, respectively. Figure 8-6 shows the domain discretization of the four meshes.

Boundary conditions for the flow problem consist of a flux of 5.79×10^{-5} m s^{-1} across a central region (0.1 m in length) of the top boundary, and an outflow boundary at the lower left corner of the domain with a hydraulic head of 2.0 m.

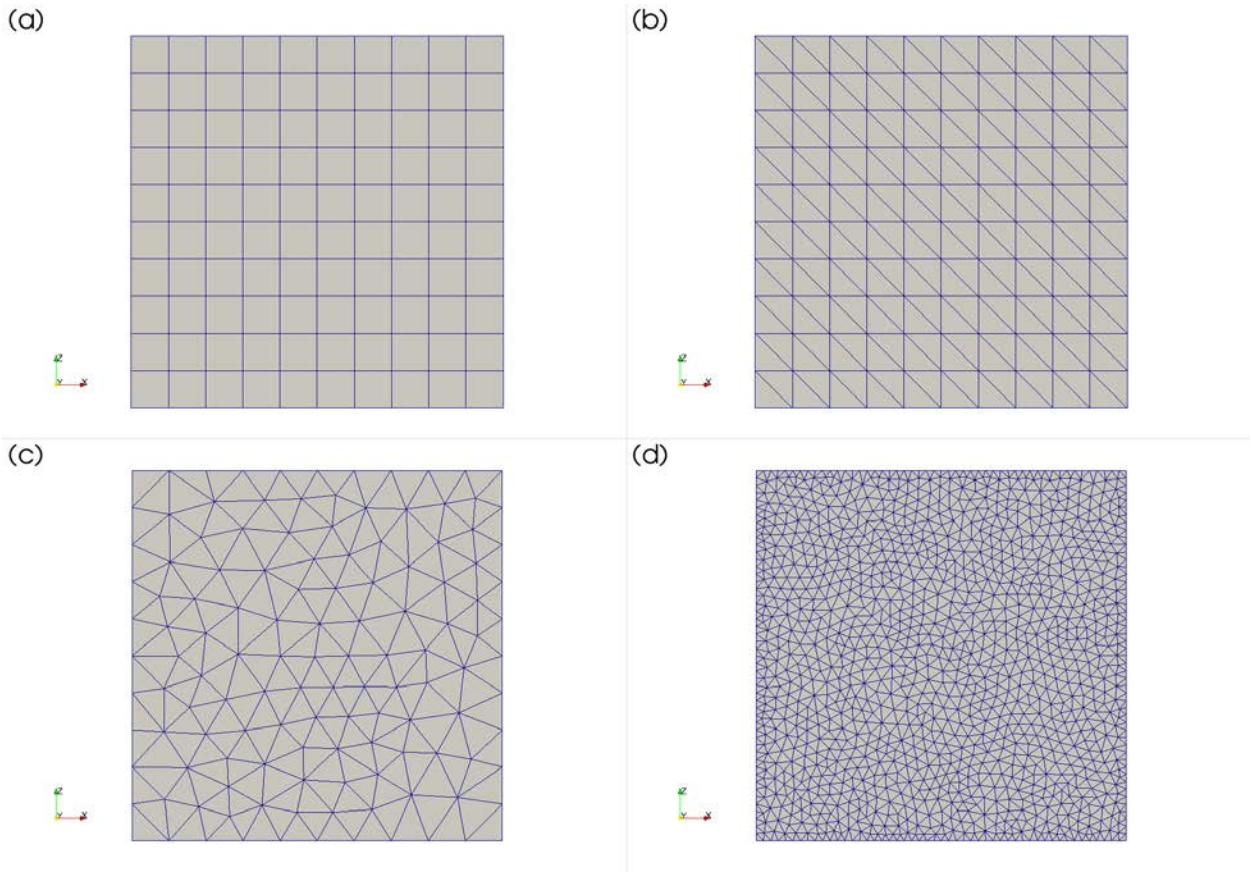

Figure 8-6: Illustration of Meshes Used in Demonstration Example Stedfs, (a) Mesh SG, (b) Mesh USG, (c) Mesh USG2 and (d) Mesh USG3

8.1.3.3 Results

The simulated pressure head contours and velocity vectors are shown in Figure 8-7 and Figure 8-8. The results are in good agreement. Taking into consideration the physics of divergent flow near the inflow location, the refined unstructured grid (USG3) provides the most representative solution for this problem.

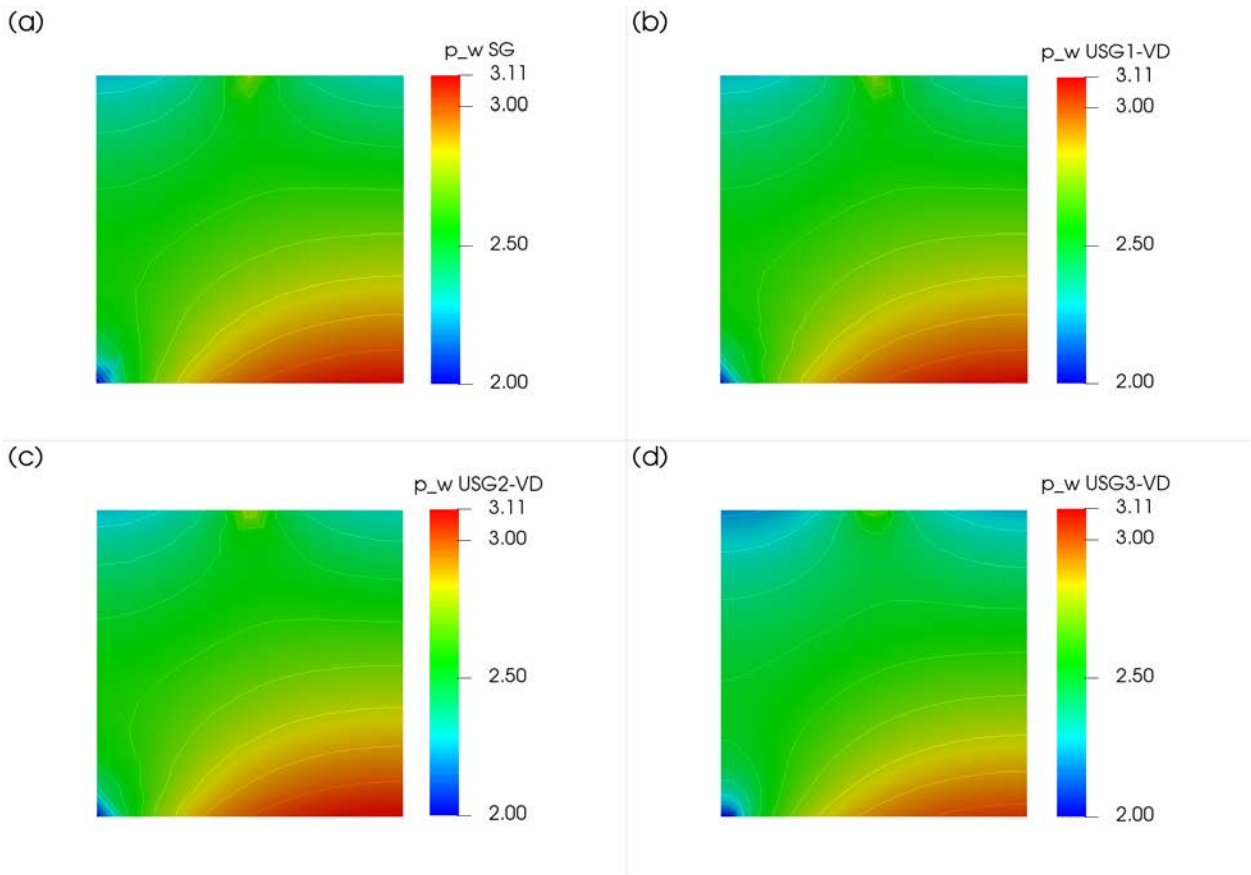

Figure 8-7: Distribution of Pressure Head [m] for Demonstration Example Stedfs Calculated by MIN3P-THCm V1.0 and MIN3P-THCm V2.0, (a) Mesh SG, (b) Mesh USG, (c) Mesh USG2 and (d) Mesh USG3

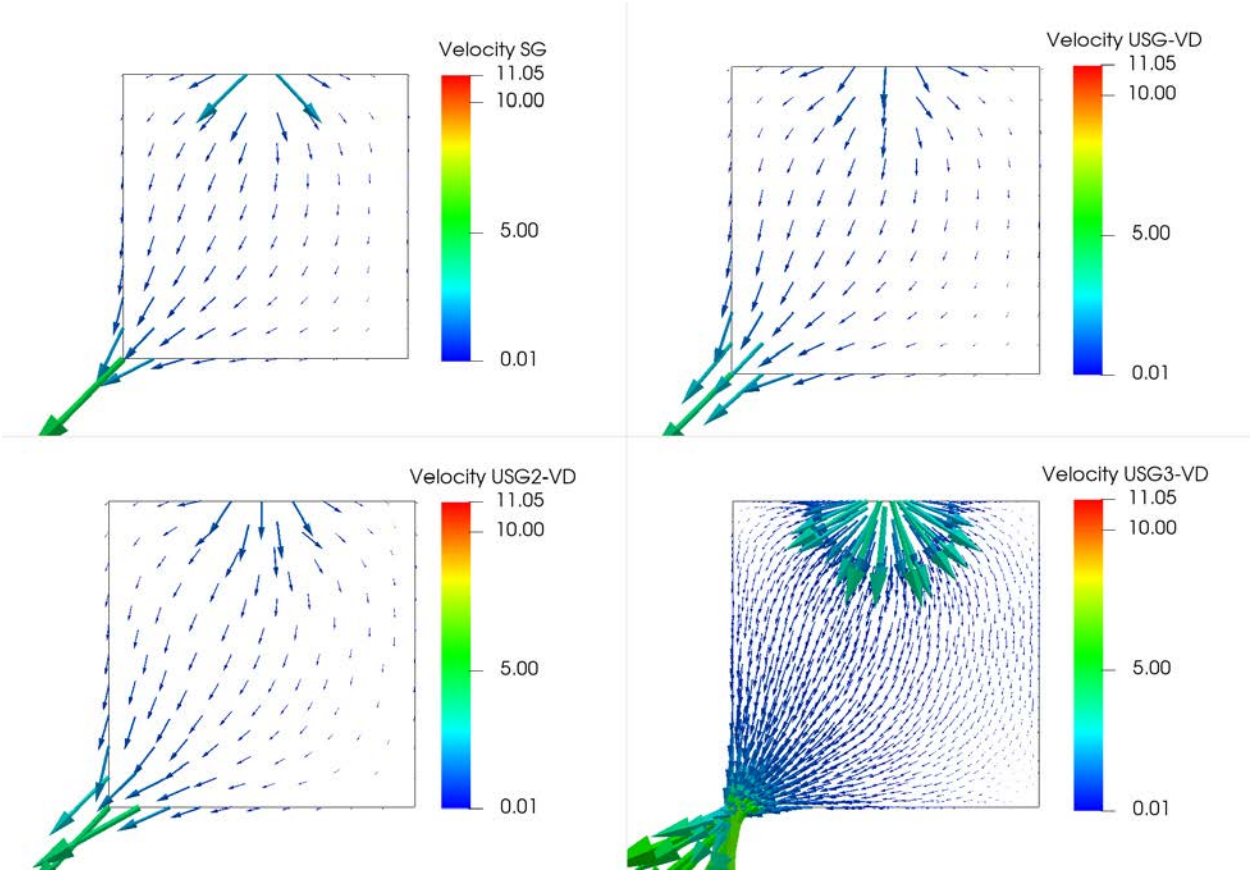

Figure 8-8: Distribution of Velocity Vectors [m day^{-1}] for Demonstration Example Stedfs Calculated by MIN3P-THCm V1.0 and MIN3P-THCm V2.0, (a) Mesh SG, (b) Mesh USG, (c) Mesh USG2 and (d) Mesh USG3

8.1.4 2D Steady-State Variably Saturated Flow

8.1.4.1 Problem Definition

This demonstration example is a two-dimensional steady–state, variably-saturated flow problem (entitled 'stedvs'). The domain is generally characterized by a high hydraulic conductivity, but contains a low conductivity region on the left side near the center of the domain.

8.1.4.2 Model Setup

The simulation domain is 1.0 m in width and 2.0 m in height. For the structured mesh, the domain was discretized into 441 control volumes yielding a discretization interval of 0.05 m in width and 0.1 m in height for the interior control volumes, and 0.025 m in width and 0.05 m in height for the control volumes on the boundary. For the unstructured meshes, the domain was discretized into 882, 591 and 12974 control volumes, respectively. Figure 8-9 shows the domain discretization of the four meshes.

The initial condition for the flow problem is defined by a pressure head of 1.0 m for the entire domain. Boundary conditions for the flow problem consist of a flux of 1.74×10^{-6} m s^{-1} on the left-top boundary (0.2 m), and an outflow boundary for the right-bottom boundary (0.5 m) with zero pressure head.

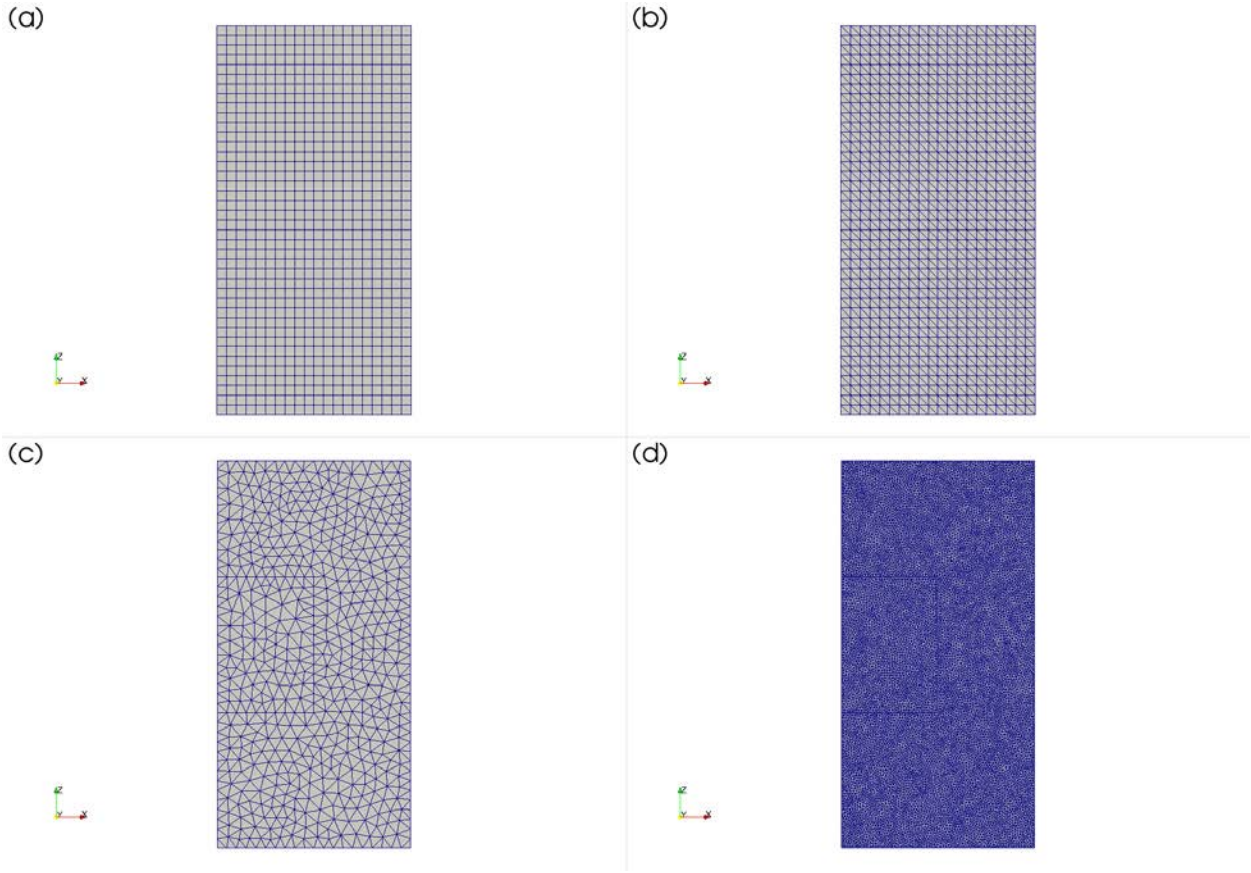

Figure 8-9: Illustration of Meshes Used in Demonstration Example Stedvs, (a) Mesh SG, (b) Mesh USG, (c) Mesh USG2 and (d) Mesh USG3

8.1.4.3 Parameters

The physical parameters (material properties) used for the simulations are summarized in Table 8-3.

Table 8-3: Physical Parameters for Demonstration Example Stedvs

Parameter	Symbol	Value	Unit
Width of domain	L_x	1.00	m
Height of domain	L_z	2.00	m
Porosity	ϕ	1.00	-
Hydraulic conductivity zone 1	K_{zz}	1.16×10^{-5}	m s^{-1}
Hydraulic conductivity zone 2	K_{zz}	1.16×10^{-13}	m s^{-1}

8.1.4.4 Results

The simulated pressure head contours and velocity distributions are shown in Figure 8-10 and Figure 8-11. The results are in good agreement.

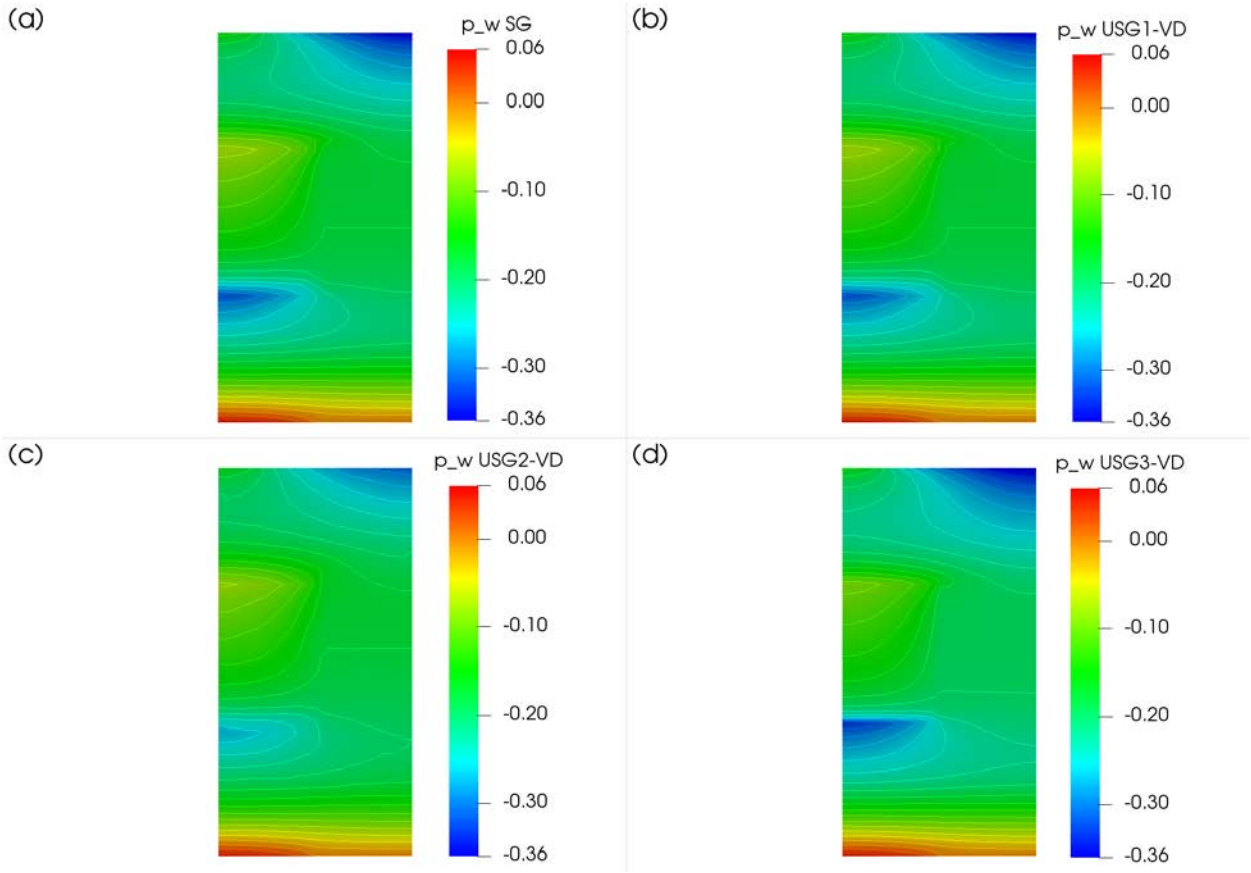

Figure 8-10: Distribution of Pressure Head [m] for Demonstration Example Stedvs Calculated by MIN3P-THCm V1.0 and MIN3P-THCm V2.0, (a) Mesh SG, (b) Mesh USG, (c) Mesh USG2 and (d) Mesh USG3

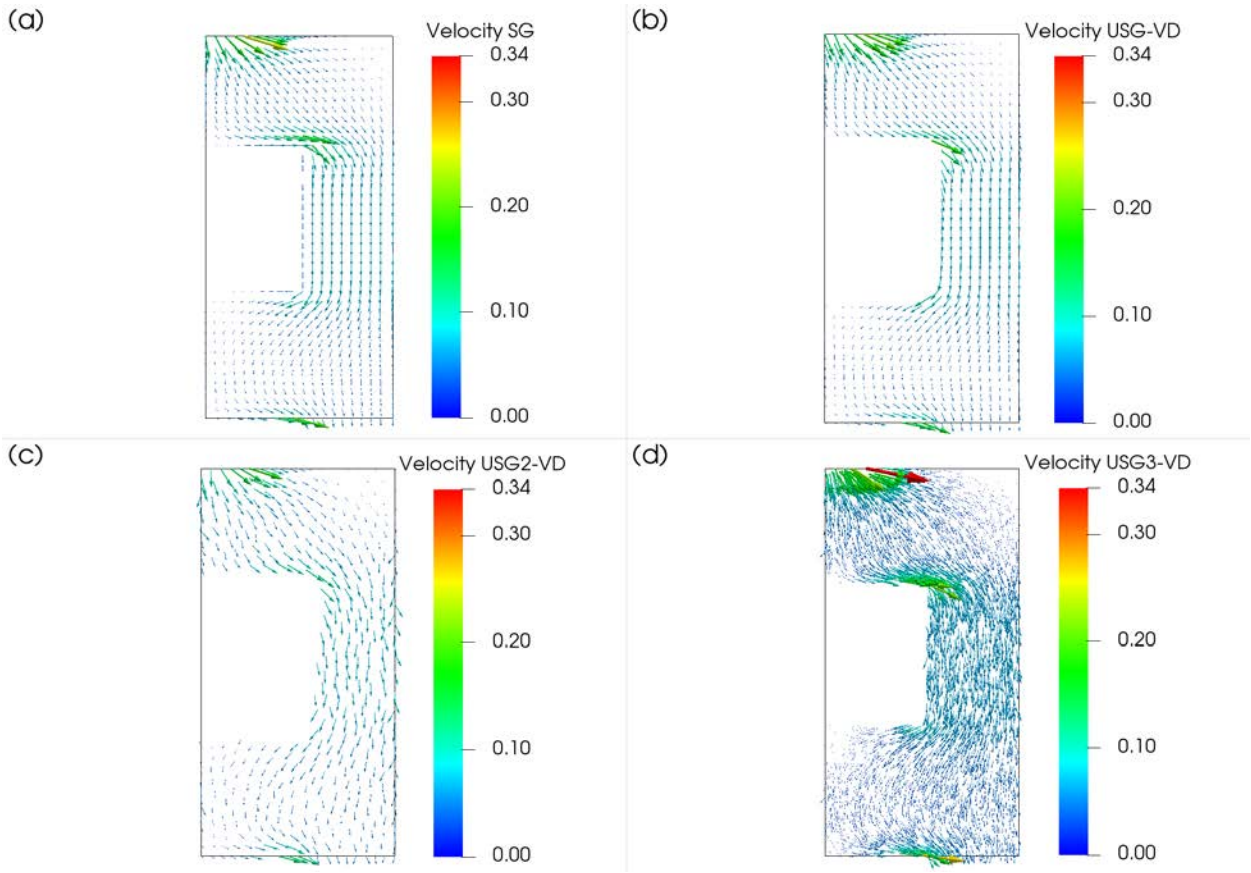

Figure 8-11: Distribution of Velocity Vectors [m day^{-1}] for Demonstration Example Stedvs Calculated by MIN3P-THCm V1.0 and MIN3P-THCm V2.0, (a) Mesh SG, (b) Mesh USG, (c) Mesh USG2 and (d) Mesh USG3

8.1.5 2D Transient Fully Saturated Flow

8.1.5.1 Problem Definition

This demonstration example is a two-dimensional transient fully-saturated flow problem (entitled 'tranfs').

8.1.5.2 Model Setup

The simulation domain and spatial discretization are the same as in the demonstration example stedfs, as shown in Figure 8-6. The initial condition for the flow problem consists of a hydraulic head of 2.0 m for the entire domain. Boundary conditions for the flow problem consist of a flux of 5.79×10^{-5} m/s at the center (0.02 m) of the top boundary, and an outflow boundary at the bottom left of the domain with a hydraulic head of 2.0 m.

8.1.5.3 Parameters

The physical parameters (material properties) used for the simulations are summarized in Table 8-4.

Table 8-4: Physical Parameters for Demonstration Example Tranfs

Parameter	Symbol	Value	Unit
Width of domain	L_x	1.00	m
Height of domain	L_z	1.00	m
Porosity	ϕ	1.00	-
Hydraulic conductivity zone 1	K_{xx}, K_{zz}	1.16×10^{-5}	m s^{-1}
Specific storage coefficient	S_s	1.00×10^{-3}	-

8.1.5.4 Results

Water flow was simulated for a period of 0.02 days. The simulated pressure heads and velocity vectors are depicted in Figure 8-12 and Figure 8-13. The results are again in good agreement for different meshes.

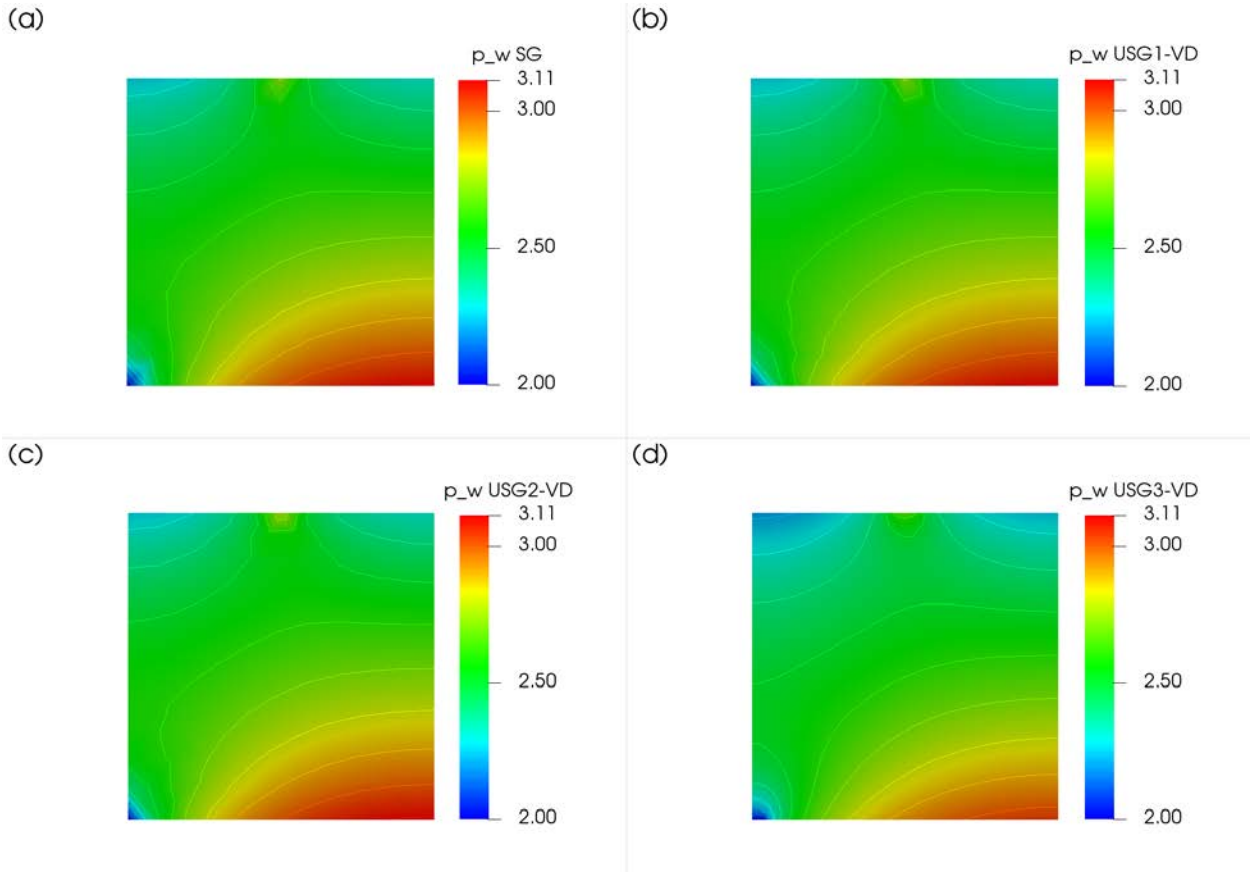

Figure 8-12: Distribution of Pressure Head [m] for Demonstration Example Tranfs Calculated by MIN3P-THCm V1.0 and MIN3P-THCm V2.0, (a) Mesh SG, (b) Mesh USG, (c) Mesh USG2 and (d) Mesh USG3

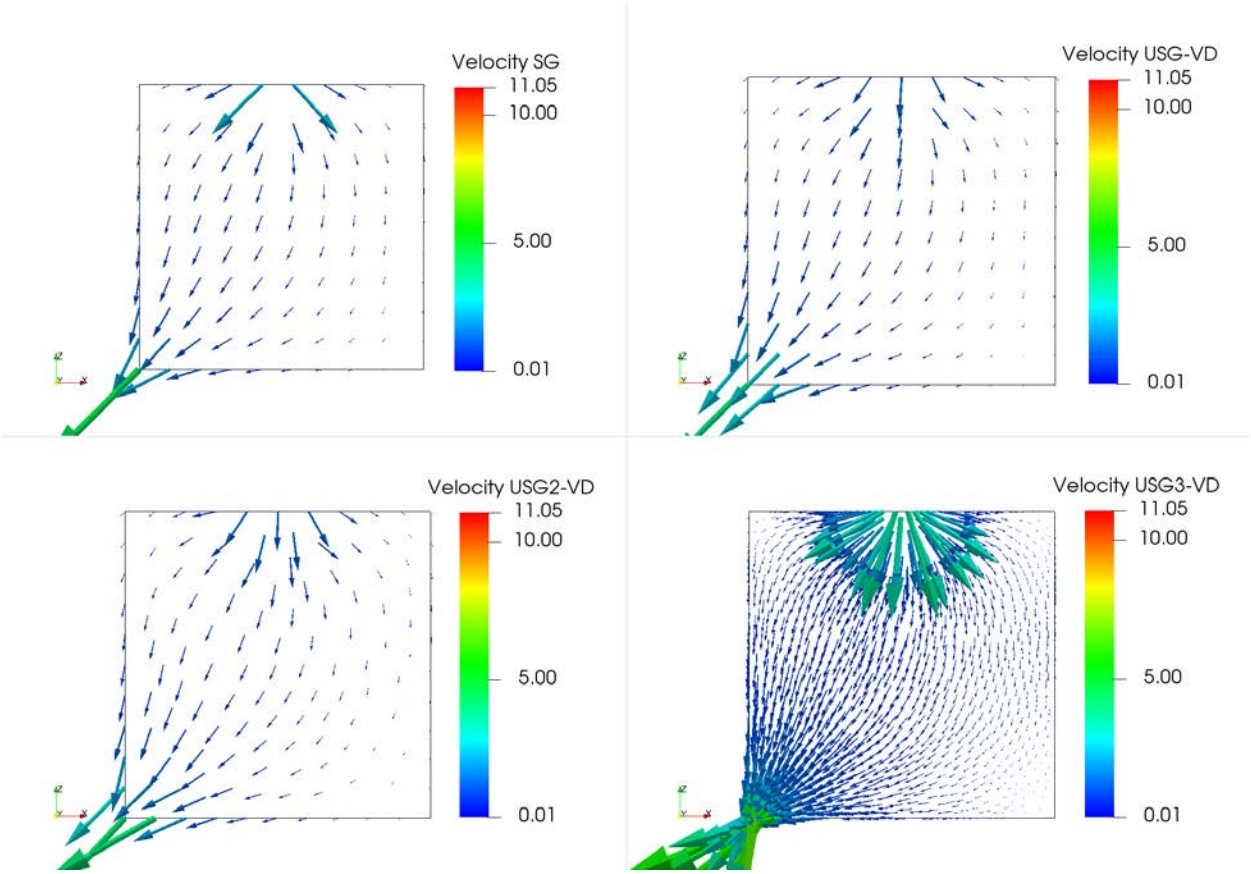

Figure 8-13: Distribution of Velocity Vectors [m day^{-1}] for Demonstration Example Tranfs Calculated by MIN3P-THCm V1.0 and MIN3P-THCm V2.0, (a) Mesh SG, (b) Mesh USG, (c) Mesh USG2 and (d) Mesh USG3

8.1.6 2D Transient Variably Saturated Flow

8.1.6.1 Problem Definition

This demonstration example is a two-dimensional transient variably-saturated flow problem (entitled 'tranvs'), identical to demonstration example stedvs, but for transient flow conditions.

8.1.6.2 Model Setup

The simulation domain and spatial discretization are the same as for the demonstration example stedvs, as shown in Figure 8-9. The initial condition for the flow problem is defined by a hydraulic head of 2.0 m for the entire domain. Boundary conditions for the flow problem consist of a flux of 5.79×10^{-5} m s^{-1} across a central region (0.1 m in length) at the top boundary, and an outflow boundary at the lower left corner of the domain with a hydraulic head 2.0 m.

8.1.6.3 Parameters

The physical parameters (material properties) used for the simulations are summarized in Table 8-5.

Table 8-5: Physical Parameters for Demonstration Example Tranvs

Parameter	Symbol	Value	Unit
Width of domain	L_x	1.00	m
Height of domain	L_z	2.00	m
Porosity	ϕ	3.00×10^{-1}	-
Hydraulic conductivity zone 1	K_{zz}	1.16×10^{-5}	m s^{-1}
Hydraulic conductivity zone 2	K_{zz}	1.16×10^{-13}	m s^{-1}

8.1.6.4 Results

Water flow was simulated for a period of 1 day. The simulated pressure head and velocity vectors are shown in Figure 8-14 and Figure 8-15. The results are in good agreement for the different meshes except for differences in velocity distribution near the interface of the regions with highly different hydraulic conductivities. These differences are caused by the velocity interpolation and a refined unstructured mesh is required to reduce the numerical error in velocity interpolation.

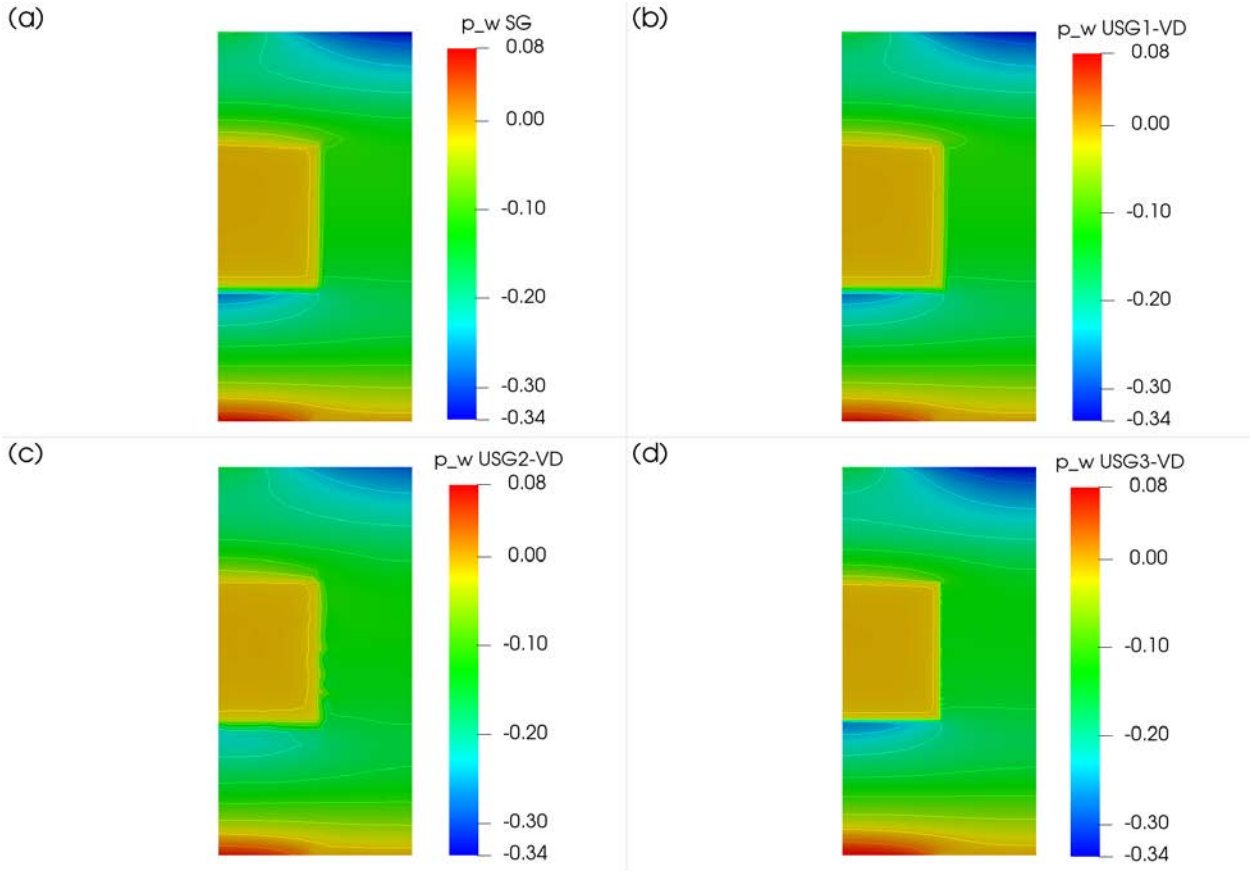

Figure 8-14: Distribution of Pressure Head [m] for Demonstration Example Tranvs Calculated by MIN3P-THCm V1.0 and MIN3P-THCm V2.0, (a) Mesh SG, (b) Mesh USG, (c) Mesh USG2 and (d) Mesh USG3

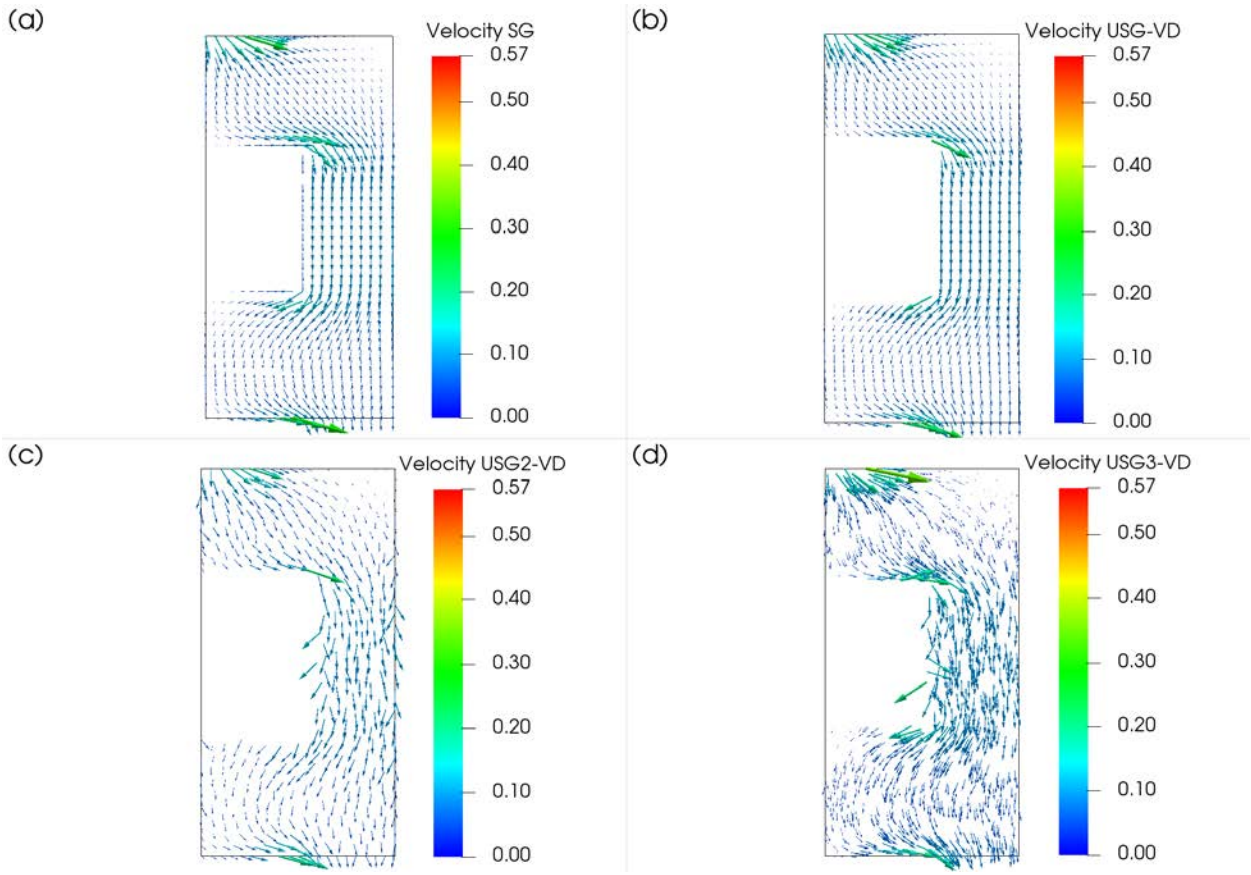

Figure 8-15: Distribution of Velocity Vectors [m day^{-1}] for Demonstration Example tranvs Calculated by MIN3P-THCm V1.0 and MIN3P-THCm V2.0, (a) Mesh SG, (b) Mesh USG, (c) Mesh USG2 and (d) Mesh USG3

8.2 2D Reactive Transport with Complex Geometry

8.2.1 Advective-Dispersive Transport

8.2.1.1 Problem Definition

This application example describes reactive transport including complexation and kinetically controlled dissolution-precipitation of calcite for a 2D-system with complex geometry.

8.2.1.2 Model Setup

This case includes aqueous complexation and kinetically controlled dissolution-precipitation of calcite. The 2D model is discretized into 6338 control volumes.

The hydraulic head for the top right boundary is constant at 0.0 m; for the bottom boundary, the hydraulic head is set at 0.0014 m. The remaining boundaries are no flow boundaries. The initial pore water concentrations and mineral contents (IC) are shown in Table 8-6. A low pH solution flows into the domain from the bottom left (between x=0.0 to 0.05 m, Z=0.0 m). The boundary condition for the remainder of the bottom is identical to the initial condition. The reactive transport boundary at the top is set as a free exit type boundary condition.

Table 8-6: Initial and Boundary Conditions for 2D Reactive Transport Problem with Complex Geometry

Parameter	Initial condition	Boundary conditions		Unit
Aqueous phase		Bottom left	Top	
H^+	2.00×10^{-7}	2.00×10^{-4}		mol l^{-1}
CO_3^{2-}	1.00×10^{-7}	1.00×10^{-4}	(free exit)	mol l^{-1}
Ca^{2+}	1.00×10^{-8}	1.00×10^{-8}		mol l^{-1}
Mineral				
Calcite	1.00×10^{-5}	-	-	m^3 m^{-3}
Hydraulic condition				
Hydraulic head	0.00	1.40×10^{-3} (first)	0.00 (first)	m

8.2.1.3 Parameters

The parameters of the porous medium are summarized in Table 8.7.

Table 8-7: Parameters for 2D Reactive Transport Problem with Complex Geometry

Parameter	Symbol	Value	Units
Hydraulic conductivity	K	1.16×10^{-5}	m s^{-1}
Porosity	ϕ	3.50×10^{-1}	-
Longitudinal dispersivity	α_l	5.00×10^{-3}	m
Transverse dispersivity	α_t	1.25×10^{-4}	m
Molecular diffusion coefficient	D_0	0.00	m^2 s^{-1}

8.2.1.4 Results

The domain mesh and simulated velocity distributions are depicted in Figure 8-16. The simulated concentrations of Ca^{2+} at 10, 20, 50 and 100 days are shown in Figure 8-17. The results demonstrate the ability of the code to simulate reactive transport in irregular domains.

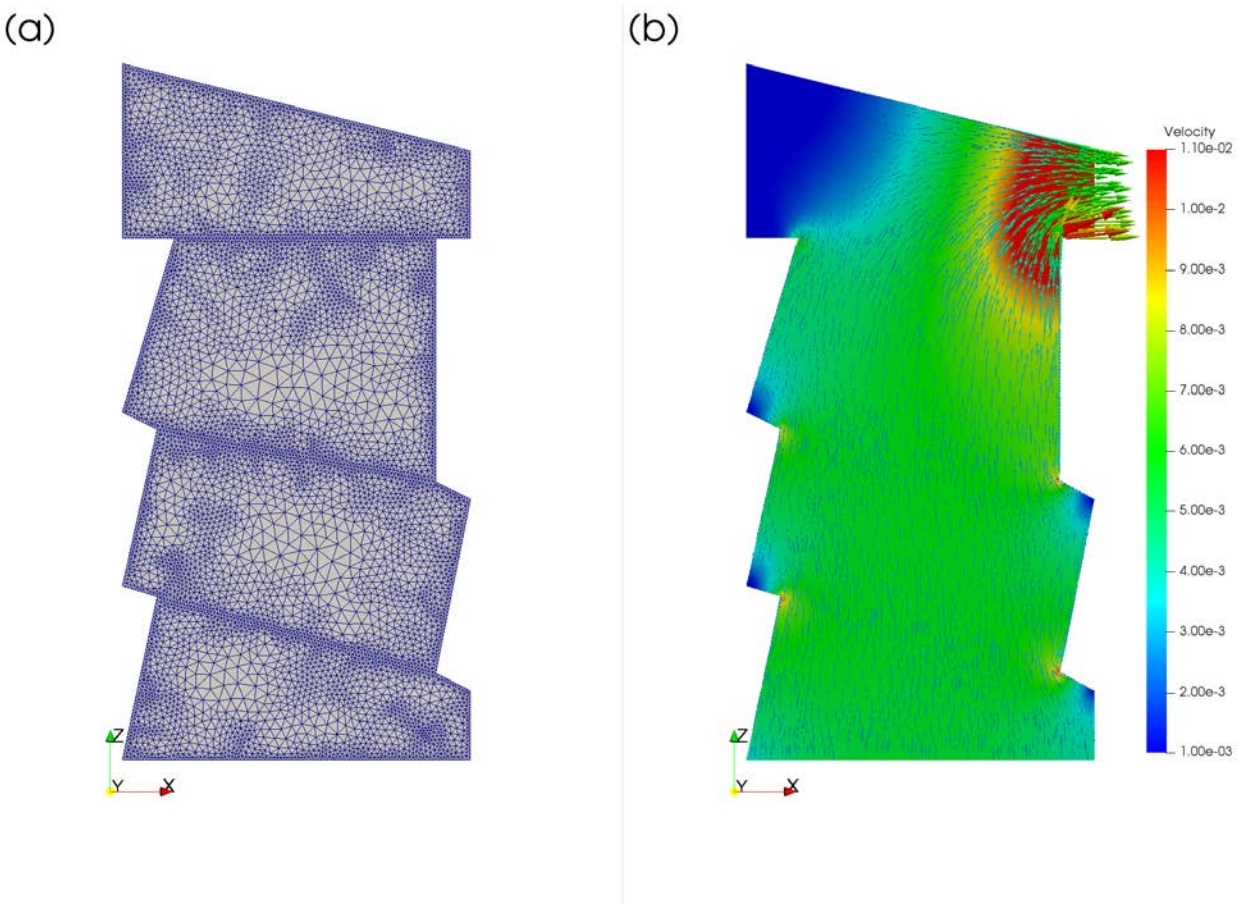

Figure 8-16: 2D Reactive Transport Problem with Complex Geometry - Simulation Domain and Velocity Vectors [m day^{-1}] Calculated by MIN3P-THCm V2.0

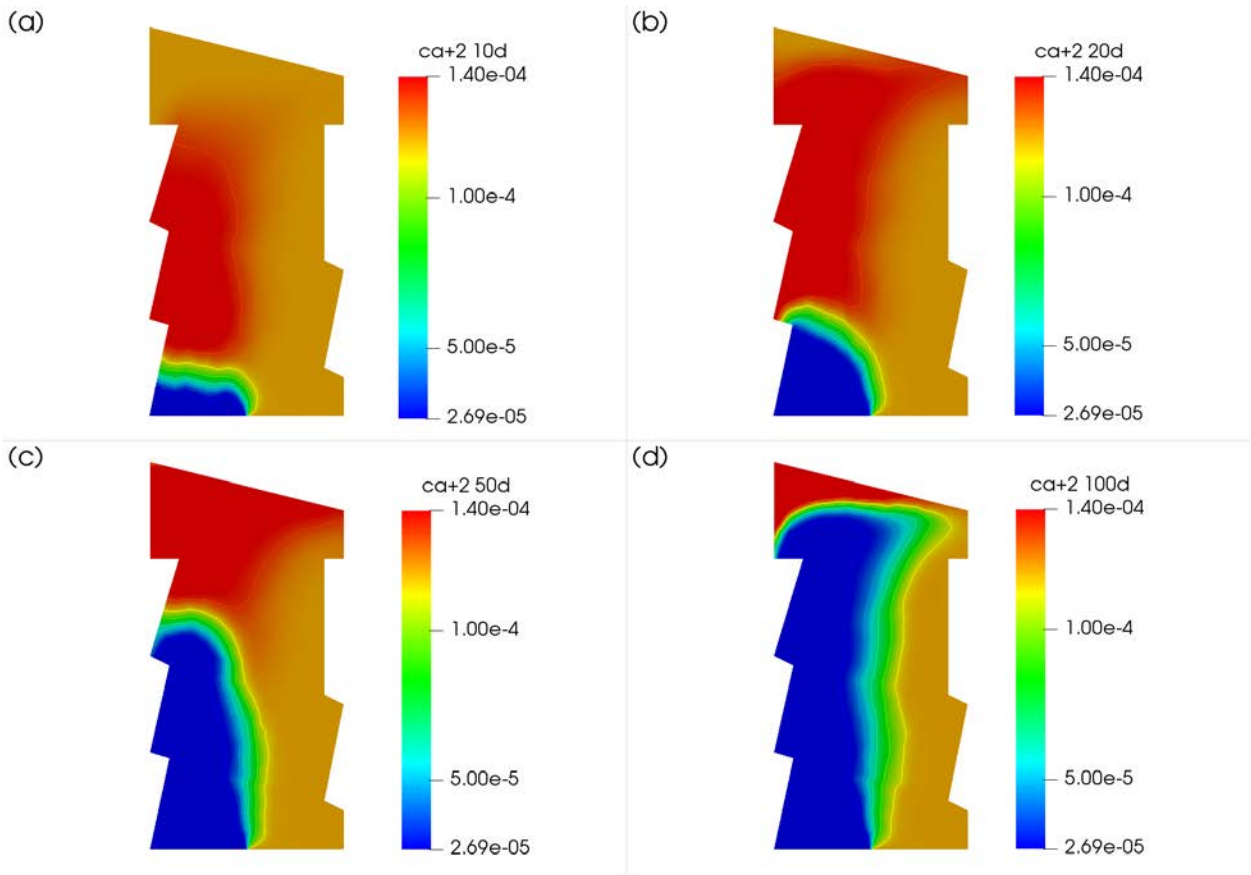

Figure 8-17: 2D Reactive Transport Problem with Complex Geometry - Concentration of Ca^{2+} [mol L^{-1}] Calculated by MIN3P-THCm V2.0, (a) 10 Days, (b) 20 Days, (c) 50 Days and (d) 100 Days

9. Conclusions

This report introduced the implementation of unstructured grid capabilities into the existing reactive transport code MIN3P-THCm V1.1, a generic process-based reactive transport code designed for the investigation of multicomponent reactive transport in variably saturated media under non-isothermal conditions. The new code, MIN3P-THCm V2.0, uses vertex-centered control volume methods. The accuracy, efficiency and convergence behaviors of the candidate set of methods are compared for variably saturated flow and reactive transport problems. The roles of different control volume types, gradient reconstruction methods, control volume interface center types, spatial weighting, and flux approximation methods, are further analyzed.

In the numerical experiments with isotropic conductivity tensors, the results are similar when different numerical methods are used. However, these different methods can play quite different roles in the accuracy and efficiency of results in the simulations with anisotropic conductivity tensors. The numerical experiments demonstrate that, for the isotropic material property, the VD control volume type has the best accuracy and can avoid non-physical oscillation for meshes with different resolutions. The CC and MD control volume types generally need high resolution meshes to avoid non-physical oscillations. The differences in gradient reconstruction methods, spatial weighting and flux approximation methods do not play an important role in the simulation cases with isotropic conductivity tensors and the difference in numerical results is not significant. In this case, the standard two-point flux approximation can still generate reasonable results. For the anisotropic material property, we find that the difference in control volume types have different effects on monotonicity, convergence behavior and mass balance error, and the VD control volume type proves to be the most robust and accurate method compared to CC and MD control volume types. The standard two-point flux approximation cannot generate accurate results for anisotropic conductivity tensors. The MPFA and MPUPS weighting schemes play a critical role in the accuracy and monotonicity that guarantees convergence compared to TPFA and standard two-point upstream weighting. Both centered weighting and MPUPS weighting work well for different control volume types and gradient reconstruction methods. Compared to the results using a structured mesh, results obtained using centered weighting are generally identical for different numerical schemes with either coarse mesh or fine mesh. However, non-physical oscillations are possible when using centered weighting for flow problems with sharp wetting fronts. In the case of centered weighting, unstructured meshes require fine resolution to ensure accuracy, while the MPUPS method also works well for a coarse mesh. The numerical experiments conducted also demonstrate that the high order Taylor expansion remainder can provide better mass balance, if used appropriately; however, this method may lead to poor convergence behavior. On one hand, the higher order scheme provides better resolution than the low-order scheme, on the other hand, the low order scheme prevents oscillations around the sharp wetting fronts.

The model verification demonstrates that the new code provides solutions of comparable accuracy relative to the results obtained with the structured grid version as well as PFLOTRAN. For the meshes that lack orthogonality, e.g., tetrahedral mesh, MIN3P-THCm V2.0 still generates reasonable results without losing quality. In addition, the new code provides a high degree of versatility and is suitable for reactive transport problems involving complex geometries and irregular internal and external boundaries by using the cell types that can adequately represent the simulation domain. These enhanced capabilities increase the solution accuracy without significantly increasing computational cost, especially for cases with a high degree of heterogeneity and anisotropy.

The performance of different parallelization schemes was analyzed based on a series of test cases. The implemented parallelization scheme provides flexibility to optimize performance by specifying the use of computational resources for different computer platforms, ranging from desktop PCs to distributed memory supercomputers. Both OpenMP parallelization and MPI parallelization provide near linear acceleration. The hybrid MPI-OpenMP version, if configured properly, can give additional speedup compared to conventional OpenMP and MPI parallelization. The parallel performance test indicates that for small problems, performance of the OpenMP parallelization performs generally better than the MPI parallelization, while for large problems that require more substantial computational resources, the MPI and hybrid MPI-OpenMP parallelizations are more preferable. By using the high performance parallelization scheme, the code can be substantially more efficient than the normal sequential version. As a result, the revised code shows a high level of versatility and is suitable for simulating large-scale long-term reactive transport problems with complex geometries, irregular boundaries and heterogeneous material distributions within practical computing times.

MIN3P-THCm V2.0 was designed for any simulation or irregular domains in 2D and 3D. The verification and demonstration of a variety of flow and reactive transport problems has shown that MIN3P-THCm V2.0 provides accurate results for both regular simulation domains and complex irregular simulation domains. In addition, the capabilities of mesh generation and mesh conversion from external software such as GMS are also possible.

ACKNOWLEDGEMENTS

This research is supported by NWMO under project GS431 and Mitacs Accelerate program (UBC ref: 22R20102). The authors would also like to acknowledge WestGrid and ComputeCanada for providing computing hardware, software and technical support.

REFERENCES

Aavatsmark, I., T. Barkve, O. Bøe and T. Mannseth. 1998a. Discretization on Unstructured Grids for Inhomogeneous, Anisotropic Media. Part I: Derivation of the Methods. SIAM J. Scientific Computing, 19(5), pp. 1717-1736.

Aavatsmark, I., T. Barkve , O. Bøe and T. Mannseth. 1998b. Discretization on Unstructured Grids For Inhomogeneous, Anisotropic Media. Part II: Discussion And Numerical Results. SIAM J. Scientific Computing, 19(5), pp. 1717-1736.

Aavatsmark, I., G. Eigestad, B. Mallison and J. Nordbotten. 2008. A compact multipoint flux approximation method with improved robustness. Numerical Methods for Partial Differential Equations.

Balay, S., P. Brune, K. Buschelman, W. Gropp, D. Karpeyev, D. Kaushik, M. Knepley, L. Curfman McInnes, K. Rupp, B. Smith, H. Zhang, S. Abhyankar, M. Adams, L. Dalcin, S. Zampini and H. Zhang. 2018. {PETS}c Users Manual.

Bea, S. A., K. U. Mayer and K. T.B. MacQuarrie. 2011. Modelling Reactive Transport in Sedimentary Rock Environments - Phase II MIN3P-THCm code enhancements and illustrative simulations for a glaciation scenario, Technical report: NWMO TR-2011-13.

Bea, S. A., K. U. Mayer and K. T.B. MacQuarrie. 2016. Reactive transport and thermo-hydro-mechanical coupling in deep sedimentary basins affected by glaciation cycles: model development, verification, and illustrative example. Geofluids, Volume 16, p. 279–300.

Bea, S. A., D. Su, K. U. Mayer and K. T.B. MacQuarrie. 2018. Evaluation of the Potential for Dissolved Oxygen Ingress into Deep Sedimentary Basins during a Glaciation Event. Geofluids, Volume 2018, pp. 1-20.

Bea, S., S.A. Wilson, K. U. Mayer, G. M. Dipple, I. M. Power and P. Gamazo. 2012. Reactive Transport Modeling of Natural Carbon Sequestration in Ultramafic Mine Tailings. Vadose Zone Journal, 11(2), pp. 1-17.

Carrayrou, J., J. Hoffmann, P. Knabner, S. Kräutle, C. Dieuleveult, J. Erhel, J. Lee, V. Lagneau, K. U. Mayer and K. T.B. MacQuarrie. 2010. Comparison of numerical methods for simulating strongly nonlinear and heterogeneous reactive transport problems—the MoMaS benchmark case. Computational Geosciences, 14(3), pp. 483-502.

Clement, T., W. R. Wise and F. J. Molz. 1994. A physically based, two-dimensional, finite-difference algorithm for modeling variably saturated flow. Journal of Hydrology , 161(1–4), pp. 71-90.

Croucher, A. E. and M. J. O'Sullivan. 1995. The Henry problem for saltwater intrusion. Water Resources Research, 31(7), pp. 1809-1814.

Davis, L. A. and S. P. Neuman. 1983. Documentation and user’s guide: UNSAT2—variable saturated flow model, Washington, D.C.

Edwards, M. G. and H. Zheng. 2010. Quasi-positive families of continuous Darcy-flux finite volume schemes on structured and unstructured grids. Journal of Computational and Applied Mathematics, Volume 234, p. 2152–2161.

Eigestad, G. T. and R. A. Klausen. 2005. On the convergence of the multi-point flux approximation O-method: Numerical experiments for discontinuous permeability. Numerical Methods for Partial Differential Equations, Volume 21, p. 1079 –1098.

Forsyth, P. A. and M. C. Kropinski. 1997. Monotonicity Considerations for Saturated--Unsaturated Subsurface Flow. SIAM J. Scientific Computing, 18(5), pp. 1328-1354.

Fujii, A., A. Nishida and Y. Oyanagi. 2005. Evaluation of Parallel Aggregate Creation Orders: Smoothed Aggregation Algebraic Multigrid Method. pp. 99-122.

Hammond, G., P. Lichtner, C. Lu, and R.T. Mills. 2012. Pflotran: Reactive flow and transport code for use on laptops to leadership-class supercomputers. In: Groundwater Reactive Transport Models.

Henderson, T. H., K. U. Mayer, B. L. Parker and T. A. Al. 2009. Three-dimensional density-dependent flow and multicomponent reactive transport modeling of chlorinated solvent oxidation by potassium permanganate. Journal of Contaminant Hydrology, 106(3–4), pp. 195-211.

Henry, H. and J. Hilleke. 1972. Exploration of multiphase fluid flow in a saline aquifer system affected by geothermal heating. Bureau of Engineering Research, Report No. 150-118.

Klausen, R. A., F. A. Radu and G. T. Eigestad. 2008. Convergence of MPFA on triangulations and for Richards' equation. international Journal for Numerical Methods in Fluids, Volume 58, pp. 1327-1351.

Klausen, R. A. and R. Winther. 2006. Convergence of multipoint flux approximations on quadrilateral grids. Numerical Methods for Partial Differential Equations, Volume 22, p. 1438–1454.

Kotakemori, H., H. Hasegawa and A. Nishida. 2005. Performance Evaluation of a Parallel Iterative Method Library using OpenMP, IEEE.

Lichtner, P. C., G. E. Hammond, C. Lu, S. Karra, G. Bisht, B. Andre, R. Mills and J. Kumar. 2018a. {PFLOTRAN} {W}eb page.

Lichtner, P. C., G. E. Hammond, C. Lu, S. Karra, G. Bisht, B. Andre, R. Mills and J. Kumar. 2018b. {PFLOTRAN} User Manual.

Marty N., O. Bildstein, P. Blanc, F. Claret, B. Cochepin, E. C. Gaucher, D. Jacques, J.E. Lartigue, S. Liu, K. U. Mayer, J. Meeussen, I. Munier, I. Pointeau, D. Su and C. Steefel. 2015. Benchmarks for multicomponent reactive transport across a cement/clay interface. Computational Geosciences, 19(3), pp. 635-653.

Mavriplis, D. J.. 2003. Revisiting the Least-squares Procedure for Gradient Reconstruction on Unstructured Meshes.

Mayer, K. U. and K. T.B. MacQuarrie, 2010. Solution of the MoMaS reactive transport benchmark with MIN3P- model formulation and simulation results. Computational Geosciences, 14(3), pp. 405-419.

Mayer, K. U., E. O. Frind and D. W. Blowes. 2002. Multicomponent reactive transport modeling in variably saturated porous media using a generalized formulation for kinetically controlled reactions. Water Resources Research, 38(9), p. 1174.

Nishida, A.. 2010. Experience in Developing an Open Source Scalable Software Infrastructure in Japan, Springer, Berlin, Heidelberg.

Nishikawa, H.. 2014. First, Second, and Third Order Finite-Volume Schemes for Advection-Diffusion. Journal of Computational Physics, 273(15), pp. 287-309.

Panday, S., C. Langevin, R. G. Niswonger, M. Ibaraki and J. D. Hughes. 2013. MODFLOW–USG Version 1: An Unstructured Grid Version of MODFLOW for Simulating Groundwater Flow and Tightly Coupled Processes Using a Control Volume Finite-Difference Formulation.

Pasdunkorale, J. and I. W. Turner. 2005. A second order control-volume finite-element least-squares strategy for simulating diffusion in strongly anisotropic media. Journal of Computational Mathematics, 23(1), pp. 1-16.

Perko, J., K. U. Mayer, G. Kosakowski, L. Windt, J. G., D. Jacques, D. Su and J. C. L. Meeussen. 2015. Decalcification of cracked cement structures. Computational Geosciences, 19(3), p. 673–693.

Sejekan, C. B.. 2016. Improving Finite-Volume Diffusive Fluxes Through Better Reconstruction.

Şengör, S. S., K. U. Mayer, J. Greskowiak, C. Wanner, D. Su and H. Prommer. 2015. A reactive transport benchmark on modeling biogenic uraninite re-oxidation by Fe(III)-(hydr)oxides. Computational Geosciences, 19(3), p. 569–583.

Simmons, C. T. and J. W. Elder. 2017. The Elder problem. Groundwater, 55(6), pp. 926-930.

Simpson, M. J. and T. P. Clement. 2004. Improving the worthiness of the Henry problem as a benchmark for density-dependent groundwater flow models. Water Resources Research, 40(1), p. W01504.

Su, D., K. U. Mayer and K. T.B. MacQuarrie. 2017. Parallelization of MIN3P-THCm: A high performance computational framework for subsurface flow and reactive transport simulation. Environmental Modelling & Software, September, Volume 95, pp. 271-289.

Therrien, R. and E. A. Sudicky. 1996. Three-dimensional analysis of variably-saturated flow and solute transport in discretely-fractured porous media. Journal of Contaminant Hydrology.

Trefry, M. G. and C. Muffels. 2007. FEFLOW: A Finite-Element Ground Water Flow and Transport Modeling Tool. groundwater, 45(5), pp. 525-528.

Vauclin, M., D. Khanji and G. Vachaud. 1979. Experimental and numerical study of a transient, two-dimensional unsaturated-saturated water table recharge problem. Water Resources Research, 15(5), pp. 1089-1101.

Voss, C. I., and W. R. Souza. 1987. Variable density flow and solute transport simulation of regional aquifers containing a narrow freshwater-saltwater transition zone. Water Resour. Res., 23(10), pp. 1851-1866.

Wexler, E. J.. 1992. Techniques of Water-Resources Investigations of the United States Geologic Survey: Chapter B7 - Analytical solutions for one-, two-, and three-dimensional solute transport in ground-water systems with uniform flow.

Wöste, J. H. M. and M. T. van Genuchten. 1988. Using Texture and Other Soil Properties to Predict the Unsaturated Soil Hydraulic Functions. Soil Sci. Soc. Am. J., Volume 52, pp. 1762-1770.

Xie, M., D. Su, K. U. Mayer and K. T.B. MacQuarrie. 2015. MIN3P-THCm: a three-dimensional numerical model for multicomponent reactive transport in variably saturated porous media.

Xu, T., N. Spycher, E. Sonnenthal, L. Zheng and K. Pruess. 2012. TOUGHREACT User's Guide: A Simulation Program for Non-isothermal Multiphase Reactive Transport in Variably Saturated Geologic Media,Version 2.0.

Younes, A., M. Fahs and B. Belfort. 2013. Monotonicity of the cell-centred triangular MPFA method for saturated and unsaturated flow in heterogeneous porous media. Journal of Hydrology, 504(11), pp. 132-141.